Università degli Studi di Udine
Dottorato di Ricerca in
Tecnologie Chimiche ed Energetiche

CHARACTERIZATION OF FIBER SUSPENSIONS IN ARCHETYPAL FLOWS BY MEANS OF STANDARD AND HIGH SPEED PARTICLE IMAGE VELOCIMETRY

Dott. Alessandro CAPONE

COMMISSIONE

Prof. Kenneth KIGER	Revisore
Prof. Tommaso ASTARITA	Revisore
Prof. Stefano DEL GIUDICE	Commissario
Prof. Giorgio PAVESI	Commissario
Prof. Fabrizio BEZZO	Commissario
Prof. Alfredo SOLDATI	Supervisore
Prof. Giovanni Paolo ROMANO	Co-Supervisore
Prof. Alfredo SOLDATI	Coordinatore del Dottorato

Author's Web Page: www.diegm.uniud.it

Author's e-mail: alessandro.capone@uniud.com

Author's address:

Dipartimento di Ingegneria Elettrica
Gestionale e Meccanica
Università degli Studi di Udine
Via delle Scienze, 106
33100 Udine – Italia
web: http://www.diegm.uniud.it

Abstract

Multiphase flows, i.e. flows in which one or more phases are dispersed within a carrier phase, are often encountered in environmental and engineering applications. The inherent difficulty in studying these flows, due to the phases interactions, is further complicated when the carrier flow is turbulent.
A specific category of two-phase flows relevant for industrial applications is represented by flows where the shape of the dispersed phase is best approximated by rods or fibers, rather than spheres. In this thesis dilute fiber suspensions in a turbulent pipe jet and in a channel with backward-facing step are characterized experimentally by means of standard and high-speed Particle Image Velocimetry. A full characterization of the near-field region of the single-phase, unladen jet is provided with a focus on entrainment rate. To this end, a simple model is presented to predict entrainment rate and tested against experimental data in the Reynolds number range [3200-28000]. The fiber-laden case is obtained by adding Nylon fibers featuring an aspect ratio of 13.3 to the pipe jet at two different concentrations at a Reynolds number equal to 10000. A phase discrimination technique is presented and validated to obtain simultaneous carrier flow and dispersed phase velocity data. Jet mean and RMS of velocity measurements, velocity correlations and spectral data are discussed with a focus on turbulence modulation induced by the dispersed fibers.
High spatial resolution measurements of fiber suspensions in a channel with a backward-facing step are presented and discussed. The high spatial resolution and the use of an object-fitting technique allow the identification and measurement of single fibers orientation within the flow. Fibers orientation and concentration data are compared to carrier flow velocity statistics. The results hint at an important role played by fibers orientation and orientation anisotropy in turbulent modulation on the carrier phase.

Contents

List of Figures

List of Tables

1 Introduction

1.1 Turbulent Multiphase Flows

Multiphase flows, namely flows in which a dispersed phase may be distinguished from a carrier phase, are ubiquitous in nature and in engineering and environmental applications. Examples of these flows are particles suspended in a liquid or gaseous flow, gas flows with droplets and liquid flows with bubbles. In general, these flows are thus characterized by a dispersed phase, in the form of particles, droplets, or bubbles, that is distributed within a carrier phase which is often turbulent.

The level and the nature of the interaction between the phases may differ remarkably in dependence of the volume fraction V_p/V_f of the dispersed phase with respect to the fluid phase. This parameter, hereafter C_v, is crucial to determine the degree of interaction occurring between the phases. When C_v is small ($C_v < 10^{-6}$) the turbulent dynamics of the carrier flow dominates on the dispersed phase dynamics and particle dispersion depends on the state of turbulence. In this case, the level of interaction is described as one-way coupling (Elgobashi [1994]), emphasizing that the effect of the carrier phase on the dispersed phase is mono-directional and negligible feedback effect is observable from the dispersed phase to the carrier flow. When C_v is closer to the order of magnitude of the carrier phase ($10^{-6} < C_v < 10^{-3}$), the regime of interaction is described as two-way coupling. The effect of the dispersed phase on the carrier flow in this case cannot be ignored and the momentum transfer from the particles is large enough to affect the carrier phase turbulence (Elgobashi [1994]). When C_v increases further the interactions occurring within the multiphase system become even more complex because particles representing the dispersed phase interact with themselves bringing about collision effects (for solid particles) or coalescence and break-up behaviours (for bubbles or droplets). This level of mutual interaction is named four-way coupling. In the limit of $C_v = 1$ the regime is defined as granular and the interactions between the dispersed phase become so dominant that the effect of interstitial flow is negligible.

As mentioned before, very often the multiphase flows encountered in engineering and environmental applications are turbulent. The simultaneous multiphase and turbulent nature of such flows makes them one of the most challenging subjects in fluid mechanics, even when the volume fraction under investigation is very low, i.e. in very dilute regimes. The stochastic nature of the carrier-phase turbulence is in fact coupled with the random

distribution of the dispersed phase and the latter poses non-trivial difficulties when experimental measurements are to be carried out or simulations to be set up.

The complex nature of the interactions occurring in turbulent multiphase flows brings about a variety of interesting phenomena. These phenomena may be organized in two main categories depending whether the phase mostly involved is the dispersed or carrier one. The majority of investigations on turbulent multiphase flows focused consequently on one of the following main aspects: the dispersed phase distribution and concentration induced by the flow and the modification of the fluid phase due to the presence of a dispersed phase.
Focusing on the dispersed phase, one of the key features of particle distribution in turbulent flows is the phenomenon of preferential accumulation (Eaton and Fessler [1994] and Squires and Eaton [1991]). Even in isotropic turbulence, particle distribution is in fact not homogeneous. Particles heavier than fluid accumulate preferentially in regions of high strain rate whereas avoid regions of intense vorticity (Wang and Maxey [1993]). On the other hand, particles lighter than fluid tend to concentrate in vortical regions (Balachandar and Eaton [2010]). A particular phenomenon strictly linked to preferential concentration is called inertial clustering (Eaton and Fessler [1994]). Inertial clustering takes its name by the fact that it is caused by the difference in inertia between a particle and the fluid and it consists in particles being drawn into clusters by turbulence.
The features of the particle distribution in a turbulent flow are conveniently interpreted in the light of the Stokes number, defined as follows

$$St = \frac{\tau_p}{\tau_f} \tag{1.1.1}$$

where the response time of a spherical particle of diameter d_p and density ρ_p takes, for a Stokes flow, the following form valid for $\rho_p \gg \rho_f$

$$\tau_p = \frac{\rho_p d_p^2}{18 \rho_f \nu} \tag{1.1.2}$$

with ρ_f and ν respectively the density and kinematic viscosity of the fluid. The particle response time τ_p represents the time needed by the particle to respond to the changes in the fluid. $\tau_f = L/U$ represents the characteristic time of the flow obtained by the characteristic velocity U and length L. The Stokes number, which may be interpreted as the ratio of the particle inertia to fluid inertia, plays a key role in the discrete phase dispersion by turbulence. When $St << 1$, the response time of the particle is much lower than that of the fluid, that is the particle is faster to respond to the fluid changes than the fluid characteristic time. This implies that the particles follow all the motions of the fluid, thus behaving as fluid elements. This is the reason why this condition is a prerequisite for particles to be employed as seeding material in optical measurement techniques such as Particle Image Velocimetry (PIV). For $St >> 1$ the particles are not responsive enough to follow the fluid dynamics and their motion is dominated by inertia. This results typically in a lag between the particle velocity and fluid velocity. The most relevant regime and the one more often occurring in applications is that characterized by

$St \approx 1$. In this case, although particles are not responsive enough to follow faithfully the fluid, turbulent eddy motion induces a relevant coherent motion in the particles. For this reason, at this regime preferential concentration effects are non-trivial and consequently most important.

The investigation on dispersed phase distribution in a turbulent flow is also of particular interest for many industrial and environmental applications: combustion devices, pneumatic transport of solid particles, spray cooling, fuel injection devices, pollution abatement systems, food processing, paper production are some of them. Consequently, a large range of experimental and numerical works have been developed over the years. Diez et al. [2011] and Campolo et al. [2005] investigated respectively experimentally and numerically the dispersion of particles in a jet crossflow. Multiphase flows in confined configuration, such as pipe or channels, were tackled by several authors (Rouson and Eaton [2001] among others). Yang and Shy [2005] and Poelma et al. [2007] focused on particle distribution in homogeneous turbulence. Also sprays were the subject of a variety of studies (Kosiwczuk et al. [2005]) together with bubbly flows (Delnoij et al. [1999] and Molin et al. [2008] among others).
As introduced earlier, another important aspect of the manifold interaction between phases in turbulent flows is represented by turbulence modulation induced by the dispersed phase in the carrier flow. In multiphase flows characterized by $C_v << 1$ and particles with lengthscale d smaller than the Kolmogorov scale η, flow turbulence is practically unaffected by particle presence (Parthasarathy and Faeth [1990]). At higher C_v the presence of a dispersed phase brings about extra mechanisms of turbulence production and dissipation. As a consequence, turbulence can be either attenuated or enhanced. The level of turbulence modulation can reach levels that qualitatevely change the features of the processes under investigation. In spite of this, the mechanisms behind it are still not fully understood and a relevant degree of uncertainty and mismatch between published results is noticeable. The difficulties lie in the broad range of scales involved, from particle to large eddies, and in the different, and simultaneously-acting, mechanisms that can cause turbulence modulation.

The mechanism contributing to turbulence modulation can be identified according to the final effect on the flow, i.e. attenuation or enhancement. Turbulence may be reduced by (Balachandar and Eaton [2010]): (I) the enhanced inertia of the particle-laden flow, (II) increased dissipation arising from particle drag, and (III) the enhanced effective viscosity of the particle-laden fluid. Turbulence increase can stem from (IV) enhanced velocity fluctuation due to wake dynamics and self-induced vortex shedding and (V) buoyancy-induced instabilities due to density variation arising from preferential particle concentration (Balachandar and Eaton [2010]). These effects may take place at the same time and most remarkably they occur at different scales. This implies that particles can have simultaneosly a suppressing and enhancing effect acting each at a different scale of the flow. Many efforts have been made attempting to predict the effect on flow turbulence by the dispersed phase. Gore and Crowe [1989] proposed a single parameter, Reynolds number independent, to characterize the dispersed phase effect on the turbulence intensity of the fluid phase. This parameter is the ratio d_p/L of the solid-phase

diameter assumed to be spherical, d_p, to the characteristic eddy length scale L of the fluid phase. For $d_p/L > 0.1$ the turbulence intensity is supposed to be enhanced by solid phase addition, whereas for $d_p/L < 0.1$ a decrease is expected (Gore and Crowe [1989]). The hypothesis is that the drag force on particles whose diameter is smaller than the most energetic eddies dampens the turbulence intensity whereas bigger particles produce wakes which eventually increase turbulence.
Due to the importance of the subject, many studies have been undertaken which focused on turbulence modulation in fluid and gaseous flow by solid particles and a comprehensive review of the results may be found in Crowe [2006] and Eaton [2006]. Turbulence modulation in homogeneous flows has been studied experimentally by Yang and Shy [2005] (air turbulence with solid particles) and Parthasarathy and Faeth [1990] (water with glass particles); in Molin et al. [2008] the turbulence induced by micro-bubbles in a vertical channel is studied numerically.

Historically important classes of turbulent shear flows are jet flows and channel flows, in which the effect of velocity gradients on the carrier phase are larger and interesting to investigate. Jets, whether confined or free, are commonly encountered in several areas of engineering involving mixing, combustion and exhaust devices. Many works have been developed which focus on turbulence modification induced by solid particles in various jet configurations. Fleckhaus et al. [1987] and Prevost et al. [1996] investigated experimentally the effect of particles dispersed in a gaseous jet finding that turbulence attenuation increases with particles size, in particular in the far-field. The works by Mergheni et al. [2009] and Sadr and Klewicki [2005] focused on coaxial jets comparing the results to those predicted by the d_p/L criteria and finding that the addition of particles featuring a d_p/L ratio of 0.2 resulted in an increase of dissipation and a slight enhancement of turbulence intensity, in agreement with Gore and Crowe [1989] criterion. Particle-laden water jets were investigated by Parthasarathy and Chan [2001] highlighting the different effects of the dispersed phase on transversal and vertical velocity fluctuations.

Channel flows also represent an important class of confined flows and are often found in applications. The scientific production on this flow laden with a dispersed phase is vast. Turbulence modulation by particles in channel flow has been investigated experimentally by Paris [2002], Rouson and Eaton [2001] and Kussin and Sommerfeld [2002] among others. This type of flow is made even more complicated when a sudden expansion is added, i.e. in the configuration called backward-facing step (hereafter BFS). This geometry is common in diffusers and conduits and adds to the complex interaction between phases due to the shear region originating from the step. The BFS multiphase flow has been the subject of many works: Yu and Lee [2009] simulated by means of Large Eddy Simulation the gas flow over a BFS performing Lagrangian tracking of the dispersed phase whereas Benavides and van Wachem [2009] performed Eulerian-Eulerian simulation in a similar configuration. Fessler and Eaton [1999] and more recently Li et al. [2010] investigated a gas flow laden with solid particles in a sharp expansion with Phase Doppler Anemometry.

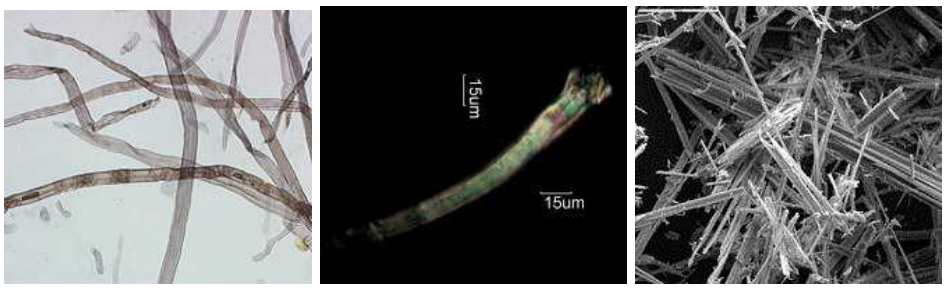

Figure 1.1: Microscopic images of wood fibers (left), nylon fibers (center) and asbesto particles (right). Pictures taken from microlabgallery.com and mcclatchydc.com.

1.2 Turbulent Fiber Suspensions

As shown in the brief review of the previous section, the majority of the studies developed in the field of turbulent multiphase flows is based on the assumption that the dispersed phase shape is spherical. This is the underlying assumption for several studies about gas or liquid flows laden with solid particles and, to a certain extent, also for gas flows with droplets and bubbly liquid flows. For the latter, the modelling and simulation of dispersed phase particle deformation poses several difficulties and represents the specific focus of various works (Molin et al. [2008] among others).

In addition to this direction of investigation, there exists a broad range of environmental processes and engineering applications where the carrier fluid is laden with particles whose shape cannot be effectively approximated by a sphere. Pollution control applications and health-related issues where the deposition and concentration of microscopic pollutants particles in the respiratory tracts is relevant; clouds formation, in which ice crystals represents the dispersed phase; paper making processes characterized by wood fibers are just a few of the most relevant fields of application. In all these processes and phenomena, the dispersed phase particles are conveniently and suitably assumed as elongated, rod-like bodies as shown in Figure 3.1, which depicts the microscopic images of respectively wood fibers, asbesto particles and nylon fibers. As it may be noticed, the features of the particles may vary remarkably in length and diameter. For this reason, a convenient parameter to categorize this kind of particles is the aspect ratio $r_p = l/d$ that is the ratio of the particle length l to its diameter d. Together with this definition and characterization of the dispersed phase it is also usually assumed that r_p is invariant with respect of time, i.e. the elongated particles may be assumed as rigid. Although this could result in an over-simplification of the problem when dealing with specific applications (drag reduction in pipe flows is one of them) this assumption is widely acceptable for many of the conditions listed before.
The use of different geometries to approximate the actual shape of the dispersed phase is also another degree of variability and includes ellipsoids, cylinders or segments. Marchioli et al. [2010], Dearing et al. [2012] and Carlsson et al. [2011] provide examples of these approaches in simulation and experimental works, with the choice of the fitting shape

having effects that will be addressed later in the next sections.

Fluid mechanics of multiphase flows in which the dispersed phase may be confidently approximated by fiber-like particles, also called fiber suspensions, is complex in particular when the flow under investigation is turbulent. The most relevant difference with respect to the spherical approximation is that unlike spheres fibers undergo rotation and their motion within the flow is dependent on this rotation. The orientation state of turbulent fiber suspensions is of fundamental importance in many applications. The mutual interactions which take place in such flows due to the orientation of fibers have an impact on the rehology of the suspension and hence is crucial for the processes where controlling this factor is a key issue. The most economically relevant example of it is paper manufacturing but also the manufacturing of fiber-reinforced materials is worth mentioning. During these processes, the fiber suspensions flow through complex geometries such as tapered channels and sudden expansions (see Lundell et al. [2011] for a thorough description of paper-making process) and the understanding of the evolution of fiber orientation (preferential orientation and coupling with the flow dynamics) is pivotal in order to improve process efficiency and product quality.
Understanding the way the phases dynamics interact with each other (two-way coupling) not only may help improve the design of the apparati through which the suspension flows, but may be usefully exploited to implement fibers orientation control methodologies.
Turbulence modulation by fibers is particularly important in drag reduction application (Parsheh et al. [2005a] and Gillissen et al. [2008] among others) where a small amount of fibers in the flow (resulting in a very dilute suspension regime) has been reported to reduce the pressure drop in piping applications. This technique represents a valid alternative to polymers drag reduction and the mechanism behind its effect are still not completely understood. It is worth mentioning that results in this field report that in order to obtain drag reduction effects, fiber aspect ratio r_p should be quite high ($r_p > 50$). In these cases the assumption of rigid fibers does not hold making the problem difficult to tackle, in particular as regards simulations studies.

The dynamics of a single rod-like particle moving in a simple, laminar shear flow was first addressed by Jeffery [1922]. Jeffery's theory predicts that in such condition, a single ellipsoid will move according to a so-called "kayaking" motion, in other words tumbling its way through the carrier fluid. This tumbling motion occurs following determined paths, named Jeffery's orbits and it is dependent on the initial orientation state of the ellipsoid, though independent of time. Jeffery's equation (Jeffery [1922]) for the angular velocity of a single ellipsoid in a laminar shear flow are

$$\dot{\phi} = -\frac{\dot{\gamma}}{{r_p}^2 + 1}({r_p}^2 \sin^2(\phi) + \cos^2(\phi)) \tag{1.2.1}$$

$$\dot{\theta} = (\frac{{r_p}^2 - 1}{{r_p}^2 + 1})\frac{\dot{\gamma}}{4} sin(2\phi) sin(2\theta) \tag{1.2.2}$$

where ϕ is the angle of the projected ellipsoid in the x-y plane with respect to the streamwise direction (Figure 1.2) while the angle of the ellipsoid with respect to the

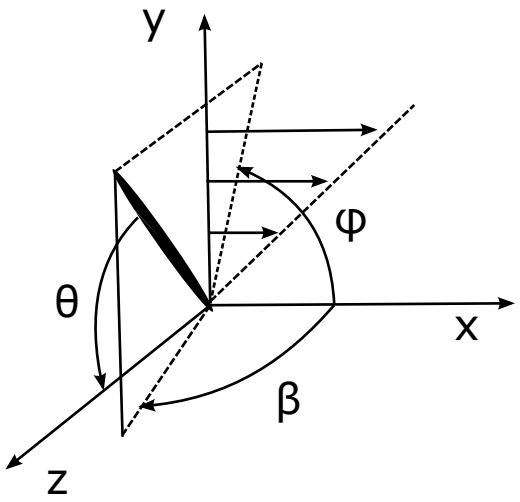

Figure 1.2: Coordinate reference for a single ellipsoid in a shear flow (Jeffery [1922]).

vorticity axis is defined as θ. As set out before, $r_p = l/d$ denotes the particle aspect ratio whereas $\dot{\gamma} = u/y$ represents the shear rate and u is the velocity component along axis x. The dots over the variables represent differentiation with respect to time. It is easy to obtain that when the ellipsoid is perpendicular to flow direction ($\theta = \pi/2$) the angular velocity $\dot{\phi}$ reaches its maximum wheras the minimum is attained in correspondance with the ellipsoid being parallel to the flow ($\theta = 0$).

Integrating equations 1.2 and 1.3 over time we obtain the following expressions

$$\tan(\phi) = \frac{1}{r_p}[-\dot{\gamma}t\frac{r_p}{{r_p}^2 + 1} + \arctan(r_p \tan(\phi_0))] \tag{1.2.3}$$

$$\tan(\theta) = \frac{Cr_p}{({r_p}^2 \sin^2(\phi) + \cos^2(\phi))^{\frac{1}{2}}} \tag{1.2.4}$$

where ϕ_0 is the initial orientation of the ellipsoid and C is an integration constant called orbit constant.

The orbit constant C describes the shape of the orbit followed by the ellipsoid in its motion (Figure 1.3). When $C = 0$ the ellipsoid is aligned with the z-axis, i.e. the vorticity axis. For values of C that tend to infinity $C \to +\infty$ the ellipsoid tend to align to x-y plane, namely the shear plane. Intermediate values of C may be matched to intermediate orbits as shown in Figure 1.3. The period of rotation of the particle takes the following form

$$T = \frac{2\pi}{\dot{\gamma}}(\frac{{r_p}^2 + 1}{r_p}) \tag{1.2.5}$$

it descends that the time the ellipsoid spends in its path along the orbit depends on the shear rate and the aspect ratio. In other words, very long, slender fibres (i.e. featur-

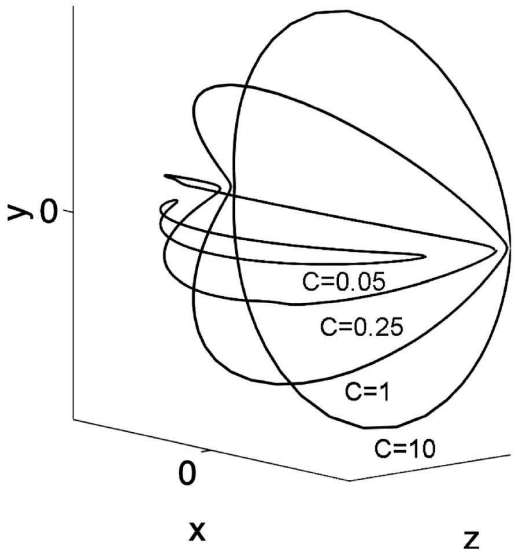

Figure 1.3: Jeffery's orbits, Jeffery [1922]. Picture from Carlsson et al. [2011].

ing high r_p values) spend most of their time aligned with the flow undergoing every half a period a revolving motion which abruptly changes their orientation.
Several experiments have been carried out to confirm the prediction of Jeffery's theory: Goldsmith and Mason [1974] verified it for different particle shapes in low Reynolds number flow and Trevelyan and Mason [1951] investigated the motion of a long cylinder in an uniform shear flow. Returning to the subject of different particle shapes, Jeffery's results have been extended to any body with fore-aft simmetry (Bretherton [1962]) provided that an equivalent aspect ratio is employed in the calculations of Jeffery's equations.

The non-trivial dynamics of a single particle in a laminar shear flow becomes even more complicated when the flow under investigation is turbulent and further difficulties are brought about when large quantities of fibers are suspended. In such conditions, fibers are in fact free to interact with the turbulent motion, other fibers and possibly walls, when dealing with confined flows. Although presently a strong demand of simulations of such systems is needed, the inherent complexity of the problem has led to many studies where the coupling between the two phases is one-directional, i.e. one-way coupling (see Sbrizzai et al. [2004] and Sbrizzai et al. [2009] among others). Just a few numerical studies in particular configurations explicitly took into account two-way coupling (Moin and Apte [2006]) and more experimental data are needed to tune effectively the existing models.
For these reasons, several experimental works have been developed to investigate fiber suspensions in a range of configurations, testing flows in different geometries, varying particles aspect ratio and materials and at different initial conditions. A comprehensive

review of these works is given in Chapter 3.

Turbulent fiber suspensions are difficult to investigate experimentally in particular due to the opacity that characterizes these flows even at dilute concentrations. A variety of experimental techniques have been employed in the attempt to analyse these flows. Laser Doppler Velocimetry has been chosen by Steen [1989] and Andersson and Rasmuson [2000] to investigate turbulence in a vertical pipe flow and in a rotary tester respectively. They both took advantage of index of refraction methodology to overcome the light scattering induced by dispersed fibers and the mentioned transparency issues.
For the above reasons, many effort have been done at developing non-invasive, non-optical techniques such as Nuclear Magnetic Resonance (NMR) and Ultrasonic Doppler Velocimetry (UVP). NMR is based on selective absorption of very high-frequency radio waves by certain atomic nuclei when the suspension is immersed in a strong stationary magnetic field. Results from Li et al. [1994] obtained in a turbulent pipe flow of a wood pulp suspension featuring nearly 1% mass concentration and Arola and Powell [1998] (water suspension with 0.5 % mass concentration in a sudden expansion) show that this technique suffer from poor signal to noise ratio and requires long measuring time. In addition to this, turbulent flows are apparently unsuitable for this technique due to difficulty in obtaining quantitative results from acquired images.
UVP is a noninvasive measurement technique that uses ultrasonic pulses to measure fluid velocity analyzing the Doppler-shift of reflected pulses. The inherent capability of this approach to allow measurements in opaque flows makes it particularly suitable for wood-pulp applications. As a downside, the commercial UVP-systems available today require dozens of ultrasonic pulses for each measurement point. This affects negatively the temporal resolution making the method most suitable for time averaged measurements. For recent works and developments using UVP refer to Sato et al. [2002] and Wiklund et al. [2006] among others.
Although with the limitations discussed earlier, the idea that is conveyed by this short overview of the state of the art in experimental works on fiber suspensions, is that whenever it is of interest to obtain quantitative measurements of turbulence quantities and a deeper insight into the flow is needed, optical methods are the most viable path to follow. The limitations posed by the maximum feasible concentrations which can be effectively observed (usually $C_v \approx 10^{-4}$) although ruling out real-time in-line applications in industrial field such as paper manufacturing or pulp processing, do not hinder the achievement of valuable results in understanding the principles behind the interactions occurring in these peculiar flows. Measurements carried out by optical techniques such as Particle Image Velocimetry (PIV) are the best choice in these cases, because they can provide non intrusively quantitative measurements of flow velocity field and simultaneously collect data on fiber concentration and, most remarkably orientation. This allows the experimentalist to shed light on the interactions between phases at an instantaneous level, and not only based on time-averaged quantities. Various experimental works have been developed addressing fiber suspension flows which reported results of orientation of fibers (a comprehensive review is given in Chapter 3) and we build on them comparing orientation and concentration results to flow data.
To this end, the purpose of this work, which is outlined in the next section, is to in-

vestigate by means of PIV technique fiber suspensions in free shear and confined flow configurations. The results will help shed light on the complex interactions taking place between dispersed and carrier phases in turbulent fiber suspensions.

1.3 Outline of the work

As described in the previous sections, an important class of multiphase flows is represented by so-called fiber suspensions. These flows are multiphase flows in which the dispersed phase is attained by elongated, rod-like particles with an aspect ratio $r_p > 1$. For this reason, in many applications, adopting the rod approximation is a more fitting choice than the spherical assumption, for which a vast literature has been produced. Fiber suspensions are difficult to handle, both in simulations and experimentally and nonetheless a demand for quantitative results is undergoing recently a rapid growth.
In this thesis, we present the results of an experimental campaign based mostly on fiber suspension flows by means of planar High-Speed and Standard Particle Image Velocimetry techniques. Despite the constraints represented by the maximum fiber concentrations which can be succesfully tested, the results will help understand better the mechanisms underlying phases interactions in turbulent flows (two-way coupling).
The fiber suspensions have been investigated in two experimental configurations, namely a turbulent pipe jet and channel flow with a backward-facing step. As detailed in the previous sections, these flows are very interesting from the applications point of view and at the same time allow the study of fiber suspensions in qualitatevely different flow conditions; a free shear unbounded flow and a confined shear flow with separation induced by the step.
Being the jet flow a historically important class of flow, in Chapter 2 we choose to characterize it thoroghly in the unladen case. In this Chapter we focus in particular on the mixing and entrainment phenomena taking place in the near-field of the jet ($x/D < 7$, where D is the pipe diameter). These phenomena are of great interest for many applications (combustion, cooling among others), in particular when a dispersed phase is present and we believe that a thorough investigation in the unladen case represents the first step along the path which leads us to a better understanding of phase interactions in fiber suspensions. To this end, in Chapter 2 we present a model to predict the entrainment rate and compare it to the experimental results for a Reynolds number range $3000 - 30000$ based on jet axial velocity U.
In Chapter 3 we build on these results investigating the same jet flow laden with fiber particles in a very dilute regime. A phase discrimination algorithm is presented to obtain simultaneous PIV velocity fields of carrier flow and dispersed phase and particle concentration data. Results are discussed and compared to the single phase case. The results obtained in Chapter 3, where the orientation state appears to play a key role in turbulence modulation in the carrier flow paves the way for the experimental campaign reported in Chapter 4.
In Chapter 4, acquisitions have been carried out in a channel flow with BFS and have been designed specifically to obtain orientation information of suspended fibers. High spatial resolution is thus achieved (0.01 mm per pixel) and data collected up to $x/H = 8$

where H represents the step height at a Reynolds number nearly 15000.
Simultaneous carrier flow velocity data and fiber orientation and velocity data are compared to results from the jet case and discussed in order to help reach a deeper insight on fiber-flow interactions in this important category of flows.

2

Turbulent pipe jet: mixing and entrainment

2.1 Introduction

As anticipated in the previous Chapter, due to the complex phenomena occurring in turbulent multiphase flows, we believe that a thorough investigation on the baseline case, i.e. the unladen, single-phase jet is useful to interpret the results of the rest of the experimental campaign.
The results presented in this Chapter will help draw a picture of the mixing and entrainment phenomena noticeable in turbulent jets, highlighting their dependence on Boundary Conditions (BC), Inlet Conditions (IC) and Reynolds number (Re, based on pipe diameter D and exit velocity U_0).
It is particularly meaningful to devise models which can isolate the effects of these parameters from each other and which are, to a broader extent, independent of the experiment details. In fact, one of the main directions of investigation on jets has been represented by the search for asymptotic behaviours which could enable a description of the flow field as much as possible independent of the details of each experiment (Xu and Antonia [2002], Hussein et al. [1994]).
In such a description, several geometrical, kinematic and dynamical parameters are involved. Restricting the analysis to low-Mach number, isothermal steady jets, it is possible to limit the number of parameters to a reduced set which, as mentioned earlier, includes IC, BC and Reynolds number, Re. Early work from Wygnanski and Fiedler [1969] conducted with Hot Wire Anemometry (HWA) showed that at $40 < x/D < 100$ (where x is the streamwixe coordinate as shown in Figure 2.1) the jet proves to be self-preserving. Wygnanski and Fiedler [1969] drew these conclusions based on several measured quantities including mean velocity, turbulence stresses, intermittency, skewness and flatness factors. Considering more recent works, Malmstrom et al. [1997] report the results obtained from a nozzle jet with different diameters at low Reynolds number and up to $x/D = 120$ focusing on the axial behaviour of the jet whereas Hussein et al. [1994] show how in the moderate-far jet field ($x/D > 15$) and for rather high Reynolds numbers ($Re > 50000$) the hypothesis of self-similarity holds.

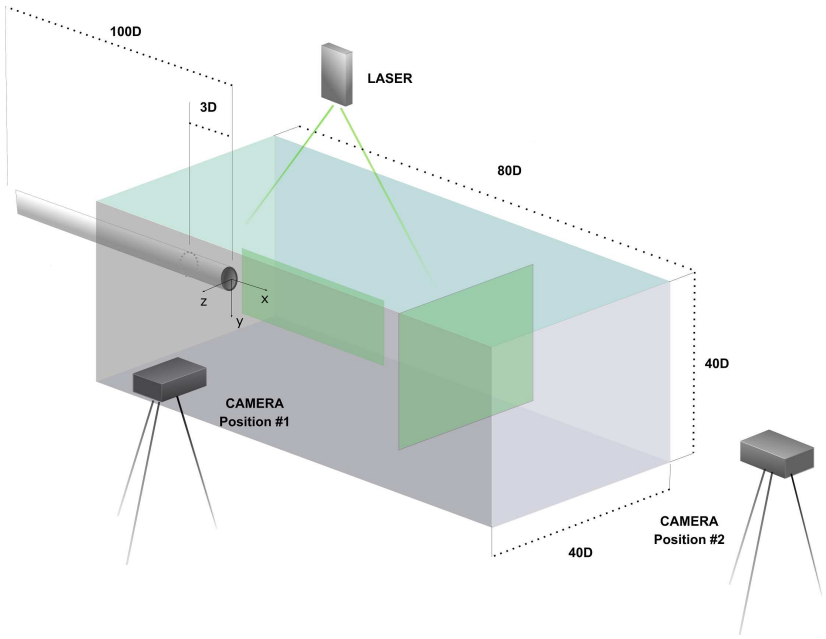

Figure 2.1: Experimental set-up for the turbulent pipe jet.

Prediction of the jet centreline velocity self-similar streamwise decay is given by (Pope [2000])

$$\frac{U_0}{U_x(x)} = \frac{1}{K_u}\left[\frac{(x-x_p)}{D}\right] \tag{2.1.1}$$

where U_0 is the jet exit velocity, $U_x(x)$ is the local centreline axial velocity and x_p is the so-called virtual origin of the jet. Similarly, the streamwise behaviour of the jet half-width $R_{\frac{1}{2}}$ (where the axial velocity is one half that at the centreline) is

$$\frac{R_{\frac{1}{2}}(x)}{D} = K_d\left[\frac{(x-x_p)}{D}\right] \tag{2.1.2}$$

The values of the constants K_u and K_d in 2.1.1 and 2.1.2 have been examined by several authors. In particular, Malmstrom et al. [1997] investigated the variation of these parameters in the case of an axisymmetric jet with different nozzle diameters comparing the results to literature data. They report that typical values lie within the interval [3.98-6.22] and [−0.3-4] for K_u and K_d respectively.
Consequently, a similar streamwise linear increase was exhibited by the shear layer momentum thickness and jet aperture calculations, according to the works by Cohen and Wygnansky [1987] and Romano [2002].
Along the radial direction, r, the axial velocity exhibits a Gaussian behaviour (Malm-

strom et al. [1997])

$$U_x(x,r) = U_x(x)e^{-\eta^2} \tag{2.1.3}$$

where $\eta = K_u r/(x - x_p)$ is the radial rescaled coordinate. The self-similar analysis can be further extended to turbulent Reynolds stresses along axial and radial directions (Kuang et al. [2001]).

It is rather established that 2.1.1, 2.1.2, 2.1.3 are almost independent on IC, BC and Reynolds number, provided that the conditions of far field ($x/D > 15$) and $Re > 50000$ hold. It is worth pointing out that these conditions correspond to those required for establishing local isotropy of the turbulent flow field. However, in many engineering applications, the interest is focused onto the jet near field and to regimes with $Re < 50000$, so that previous issues regarding asymptotic behaviour rise up again. An example of this is provided by the work by Malmstrom et al. [1997], where robust indications on a linear dependence of K_u on Reynolds number, for low Reynolds numbers ($Re < 50000$) are shown.
This conclusions could reflect the simultaneous reduced jet spread as a function of Reynolds number shown by Hussein et al. [1994] for high Reynolds number jets ($Re = 100000$). The Large Eddy Simulation (LES) investigations on the circular pipe jet made by Kim and Choi [2009] pointed out that the behaviour of mean and rms axial velocity along the streamwise direction is strongly dependent on the combined effects of Reynolds number and IC (namely the momentum thickness at the jet outlet). This has been derived also by Bogey and Bailly [2009], with a jet LES at $Re = 11000$ and is in agreement with early observations by Zaman and Hussain [1981] and Crow and Champagne [1971]. Not all reports confirm this behaviour and such a dependence was not observed by Fellouah and Pollard [2009] on a contraction jet at Reynolds numbers between 6000 and 100000.
There exists also a certain degree of variation due to the BC and many works have been developed on the subject. Xu and Antonia [2002] show what the impact of the jet stemming from a long pipe or a smooth contraction nozzle is on turbulent structures and consequently on jet self similarity. In Quinn [2006], Quinn [2007] and Mi et al. [2007] the focus is set on the effect of a sharp or smooth edge of the nozzle on the jet structure employing different measuring techniques.
The subject of the nozzle geometry was furtherly investigated by Deo et al. [2007a] in the case of a plane jet issuing from a nozzle with different geometries. The impact of BC on the jet turbulent structures has been tackled by Romano [2002] for a jet originating from a contraction focusing in particular on the effects of a free-slip or no-slip boundary condition at the contraction outlet. In Deo et al. [2007b], building on the results from Deo et al. [2007a] and on the same apparatus, the effect of rigid walls at the sides of a plane jet was investigated.

The broad range of parameters involved suggests that it is desirable to separate the contribution of each of the previous effects to establish specifically if there is a Reynolds number dependence. In particular, the dependence on Reynolds number should be con-

sidered within the entire picture of jet flow behaviour along the streamwise and orthogonal directions, being the phenomena under observation fully three-dimensional. Indeed, this point is connected to the subtle argument underlying the self-similarity hypothesis, i.e. that the flow was described by a single length (and velocity) scale (Burattini et al. [2005]). However, if IC, BC and Reynolds number influenced self-similarity, it should be expected that this will not be the case and the number of relevant scales would increase. Thus, it is rather important to establish the effect of IC, BC and Re on the relation among longitudinal (axial) and transverse (radial) phenomena.

2.2 Relations among axial and radial flows

In the case of constant density jets, it is useful to start from the definitions of axial and radial volumetric flow rate, respectively Q_a and Q_r, and relating them to the entrainment rate as in Wygnanski and Fiedler [1969], Crow and Champagne [1971] and Liepmann and Gharib [1992]. The mass balance on the differential control volume shown in Figure 2.2 can be written as:

$$\frac{\partial Q_a}{\partial x}\mathrm{d}x = -\mathrm{d}Q_r(x,R), \tag{2.2.1}$$

thus it is possible to write

$$Q_a(x+\mathrm{d}x,R) - Q_a(x,R) = -\mathrm{d}Q_r(x,R) \tag{2.2.2}$$

Therefore, using the axial and radial volumetric flow rates expressions

$$Q_a(x,R) = \int_0^{2\pi}\int_0^{R} U_x(x,r,\theta) r \mathrm{d}r\mathrm{d}\theta \tag{2.2.3}$$

$$dQ_r(x,R) = \left(\int_0^{2\pi} U_r(x,R,\theta) R \mathrm{d}\theta\right) dx \tag{2.2.4}$$

the following descends from relation 2.2.2.

$$\frac{d}{dx}\int_0^{2\pi}\int_0^{R} U_x(x,r,\theta) r \mathrm{d}r\mathrm{d}\theta = -R\int_0^{2\pi} U_r(x,R,\theta)\mathrm{d}\theta \tag{2.2.5}$$

where R is a generic radius over which integration is performed which could be also a function of the axial distance x, U_r is the radial velocity component and θ is the azimuthal angle. This equation establishes a relationship among axial and radial velocities, at each downstream distance, as also a means to derive the entrainment rate (which is just the left hand side of the equation) from radial velocity distribution along a circle centered on the jet axis. For large R (in comparison to local jet radius defined in 2.1.2) the integral will reach an asymptotic value (Liepmann and Gharib [1992]), whereas for small R the

dependence on the radial coordinate will be outlined. In the following, the dependence on the azimuthal angle θ will be relaxed on the basis of the results presented in this thesis, to focus the attention on axial and radial behaviours. Thus, we can insert in 2.2.5 the expression for the axial velocity component derived from combining 2.1.1 and 2.1.3, i.e. we are considering the self-similar region, to obtain

$$\frac{U_0 D}{2K_u}\frac{d}{dx}[(x-x_p)(1-e^{-H^2})] = -RU_r(x,R) \tag{2.2.6}$$

where $H = K_u R/(x-x_p)$. Therefore

$$\frac{U_r(x,R)}{U_0} = -\frac{1}{2H(x-x_p)/D}\frac{d}{dx}[(x-x_p)(1-e^{-H^2})] \tag{2.2.7}$$

where the dependence of $H(x)$ should be specified (through $R(x)$). If we assume that along the axial distance, the generic radius R scales as in 2.1.2, the quantity H is a constant along x and it is derived from 2.2.7 that

$$\frac{U_r(x,R)}{U_0} = -\frac{1}{2(x-x_p)/D}\frac{(1-e^{-H^2})}{H} \tag{2.2.8}$$

whereas without such an assumption the outcome is the following

$$\frac{U_r(x,R)}{U_0} = -\frac{1}{2(x-x_p)/D}\frac{(1-e^{-H^2}(1+2H^2))}{H} \tag{2.2.9}$$

This is a well defined behaviour with negative values, i.e. positive entrainment, along the axial distance (decreasing as $1/x$) in both model equations. Considering relation 2.2.5, in the potential core, i.e. with $U_x \approx U_0$ and $R(x)$ equal to a constant $(D/2)$, it descends that $U_r(x,R) \approx 0$ (no entrainment). Along the radial direction the hypothesis on H to be independent of x or its relaxation leads to different behaviours up to $H \approx 2.5$. In particular, for $H < 1.2$ a positive radial velocity is predicted by equation 2.2.9 as opposed to 2.2.8 as shown in Figure 2.3 which displays 2.2.8 and 2.2.9 versus H. Similarly, the behaviour of axial and radial flow rates in the self-similar region can be derived from 2.2.3 and 2.2.4

$$\frac{Q_a(x,R)}{Q_0} = \frac{4}{K_u}\frac{(x-x_p)}{D}(1-e^{-H^2}) \tag{2.2.10}$$

$$\frac{dQ_r(x,R)}{Q_0} = -\frac{4}{K_u}(1-e^{-H^2})\frac{dx}{D} \tag{2.2.11}$$

the latter taking the following form in case no assumption is made about R scaling

$$\frac{dQ_r(x,R)}{Q_0} = -\frac{4}{K_u}(1-e^{-H^2}(1+2H^2))\frac{dx}{D} \tag{2.2.12}$$

where $Q_0 = \pi D^2 U_0/4$ is the flow rate at the jet nozzle. Along the streamwise direction x, from 2.2.10, the well known linear increase of the axial flow rate can be derived.

On the other hand, the radial flow rate from being zero at the nozzle, attains a negative constant value for increasing axial distance. In the potential core, from 2.2.3, 2.2.4 and 2.2.5, the initial values of the flow rates are $Q_a = Q_0$ and $Q_r = 0$. The behaviour along the radial direction is much more interesting and it is shown in arbitrary units in Figure 2.3 as a function of H (which depends on both the radial and axial coordinates) for model equations 2.2.8-2.2.11 (hereafter equations A) and 2.2.9-2.2.12 (hereafter equations B). In Figure 2.3, the parameters K_u and x_p are taken respectively equal to 6 and 0 as in Malmstrom et al. [1997] for similar IC and a Reynolds number equal to 42000. The entrainment rate ($dQ_r(x,R)/dx$) starts from zero for $H = 0$ and attains an asymptotic negative value for both models A and B (in arbitrary units equal to -1). For intermediate values of H, a region of negative entrainment is present in model B, as for the radial velocity, ending at nearly $H = 1.2$. This behaviour is the same for the axial flow rate with opposite sign.
Starting from the models presented, the aim of this Chapter is to highlight the connections between phenomena on longitudinal and transverse planes and their effects on mixing in the near field of a circular turbulent jet by focusing the attention on their dependence on Reynolds number. To this end, high-speed PIV measurements on longitudinal and transverse planes are performed. The relevant quantities for this analysis are axial, radial and azimuthal velocities and their spatial behaviours, the axial and radial flow rates, entrainment rate calculations and velocity fluctuations. Later in this Chapter the results obtained in longitudinal planes are carefully verified and compared to existing results to investigate if the Reynolds number dependence could be connected to the mixing transition in jet flows, reported by Dimotakis [2000], Hill [1972] and Liepmann and Gharib [1992]. For Reynolds numbers below 10000, the cited authors report a rather strong dependence on Reynolds number which almost disappears for $Re > 10000$. In Section 2.5 the results on cross-planes are examined to establish if the simplified models descending from far field behaviour here presented are able to capture the essentials of the highly three-dimensional phenomena involved in the near field of turbulent jets. The possibility of acquiring data on both longitudinal and transverse planes, is used at the end of this Chapter to verify the correctness of the hypothesis of perfect balance among axial and radial flow rates which is the basis for the derived simplified models.

2.3 Experimental set-up

The water jet apparatus is detailed in Figure 2.1; the facility consists of a long pipe with a round section of diameter $D = 2.2$ cm ending nearly 7 cm inside the observation tank. Being the pipe nozzle not flush with the tank's wall the jet flow features a reentrant behaviour (Romano [2002]). The pipe is about $100D$ long, which is enough to observe fully developed turbulent flow conditions. The observation tank is approximately $40D$ high and wide, approximately $60D$ long and is made of glass for full optical access. Due to the limited size of the tank, the jet is considered as confined rather than free. It should be pointed out that this work focuses on the near field region of the jet where the cross-sectional area of the jet flow, estimated as three times the jet half width $R_{\frac{1}{2}}$ is below $2D$ and then small compared to the observation tank width whose effect on the

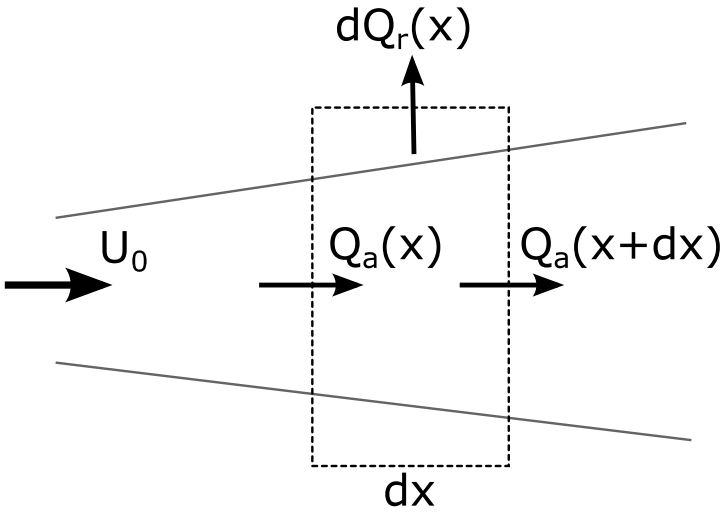

Figure 2.2: Schematic of volumetric flow rate balance.

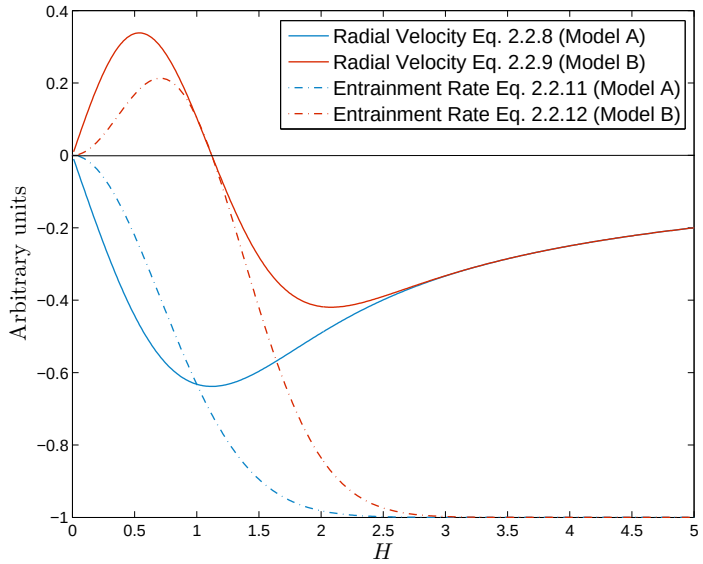

Figure 2.3: Radial velocity and entrainment rate model equations versus $H = K_u R/(x - x_p)$ given in arbitrary units

Figure 2.4: Sample streamwise PIV image at $Re = 10000$. Pipe outlet is visible at the far left of the picture.

flow is thus negligible (Cater and Soria [2002]).
The flow is driven by constant head provided by an elevated tank which is constantly supplied by a pump. At the bottom of the observation tank, opposite to the pipe outlet, a discharge hole is located which was kept closed during measurements in order not to introduce disturbances in the flow. It follows that the fluid level at the top of the tank is allowed to increase slightly (less then 1 mm) during measurements.
A high-speed PIV system is set up by means of a high-speed 8-bit BW, Photron APX CMOS camera with 1024×1024 pixels resolution at 1 KHz frame rate. The camera objective used for all the acquisitions was a Nikon F 50 mm focal length with maximum aperture of 1.2. Lighting is provided by a continuous Spectra Physics Ar-ion laser, $488-514$ nm in wavelength, with a maximum power equal to 7W, and flow seeding was attained with almost neutrally buoyant 10μm diameter hollow glass spheres (Dantec HGS-10).

Two types of image acquisition were carried out, based on the position of the camera. The first set of acquisitions, hereafter called streamwise acquisitions, was performed by placing the camera laterally with respect to the main flow (denoted as Position 1 in Figure 2.1) whereas the second image set, hereafter called crosswise acquisitions, was obtained by setting the camera facing on transversal planes (labelled as Position 2 in Figure 2.1).
Streamwise measurements covered an area of approximately $6D$ from the nozzle exit, resulting in a pixel resolution of 0.12 mm corresponding to $0.006D$. In order to collect

Re	F_a (Khz)	F_s (Khz)	T_{win} (s)	D_{max} (pixels)
3200	0.5	1	20	4
6000	0.5	1	20	7
10000	1	2	10	6
14500	1	2	10	8
22000	1	3	10	12
28000	1	4	10	15

Table 2.1: Streamwise measurements acquisition parameters. F_a and F_s represent the acquisition and shutter rate, T_{win} is the measurement time and D_{max} the average maximum displacement.

data from the jet's far field, complementary streamwise acquisitions were performed by composing a series of close-up measurements covering each approximately $3D$ and reaching $18D$ in the far field.
Transverse, crosswise acquisitions covered a squared area with side of approximately 3D with a pixel spatial resolution of 0.12 mm. Measurements were carried out on planes lying within a range from 0.75 to $4.5D$ from the nozzle exit.
In the experimental campaign, the jet Reynolds number based on the jet bulk velocity U_0 ranged from 3200 to 32000 for both acquisition types. For each Reynolds number, typically 5000 image pairs were collected. Streamwise measurements acquisition rate was 0.5 or 1 KHz corresponding to a δ_t between image pairs of respectively 0.002 and 0.001 seconds. Shutter time was set according to the flow speed in order to keep the maximum distance traveled by the seeding particles in a time frame well below 0.5 mm, corresponding to 4 pixels. In Table 2.1 acquisition parameters for streamwise measurements are reported. Crosswise measurements were carried out with an acquisition rate of 1 KHz. Laser sheet thickness was approximately 1 mm. A sample image for the streamwise acquisitions, obtained at $Re = 10000$, is given in Figure 2.4.

A commercial PIV software, that is DaVis by LaVision Gmbh, has been employed for instantaneous vector field computation. The advanced image deformation multi-pass PIV cross-correlation algorithm with window offset, adaptive window deformation and Gaussian sub-pixel approximation algorithm and the hybrid PIV/PTV algorithm employed for PTV tracking, are described in Stanislas et al. [2008], together with features and overall performances. Minimum window size adopted was 32×32 and 16×16 pixels for streamwise and crosswise measurements respectively. In both cases overlap was set to 75 percent, thus the spacing between velocity vectors was 8 and 4 pixel corresponding to a spatial velocity resolution of approximately $0.045D$ for all acquired data.

As described in detail in Falchi and Romano [2009], data collected via high-speed PIV systems have a high degree of correlation in time. Thus, the high temporal resolution of the present measurements (0.001 and 0.002 seconds, respectively 0.04 and 0.08 integral time scales) allows to derive correlation functions. Integral time scale was derived by the integral length scales measured from correlation functions in the far field, i.e. L=10 mm, divided by the local mean velocity, about 0.4 m/s. At the same time, the typical

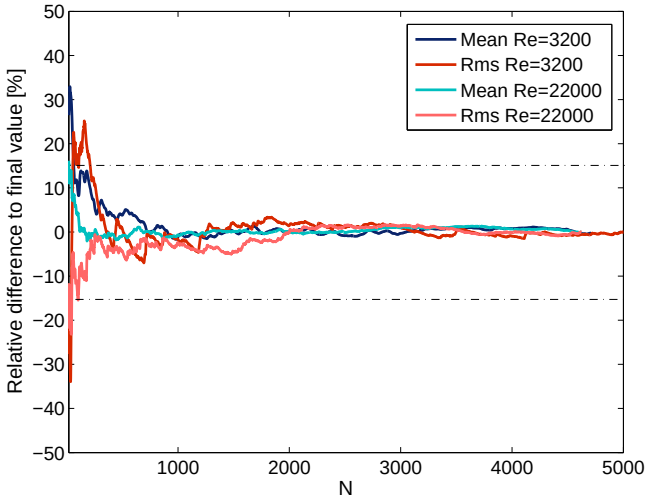

Figure 2.5: Relative differences to final values for the first two statistical moments of the streamwise velocity components.. Data from upper shear layer ($y/D = 0.5$) in jet's far field ($x/D \approx 5$).

acquisition time window for the streamwise case was 10 or 20 seconds, depending on the Reynolds number, and covered as much as 400 integral time scales so that reported data are also almost statistically independent to attain statistical convergence (Falchi and Romano [2009]). An example of that is given in Figure 2.5 where the relative difference to the final value for the mean and rms of streamwise velocity is given versus number of samples N. Data are taken at a point within the shear layer in the jet far field ($x/D = 5$) at a Reynolds number of 3200 and 22000 and show a good overall behaviour in both cases, with both mean and rms within 15% relative difference already for $N > 1000$ and within 2% for $N = 4000$.

2.4 Results on streamwise decay and validation

In Figure 2.6, the horizontal decay of average axial velocity is reported and compared to that provided by Amielh et al. [1996] obtained by means of Laser Doppler Anenometry at a Reynolds number of 21000 and to low Reynolds number data from O'Neill et al. [2004]. The present data covered a range of Reynolds number from 3200 to 28000 reaching up to $x/D = 9$. For the largest Reynolds number, data were collected by composing three slightly overlapping close-up runs, each of nearly $3D$ length, thus reaching as far as $9D$ and adding a further series in the jet's far field up to approximately $18D$. Data have been trimmed at the border of each imaged region to account for the intrinsic loss of accuracy of PIV algorithm at the boundaries. Capital and lowercase letters are used respectively

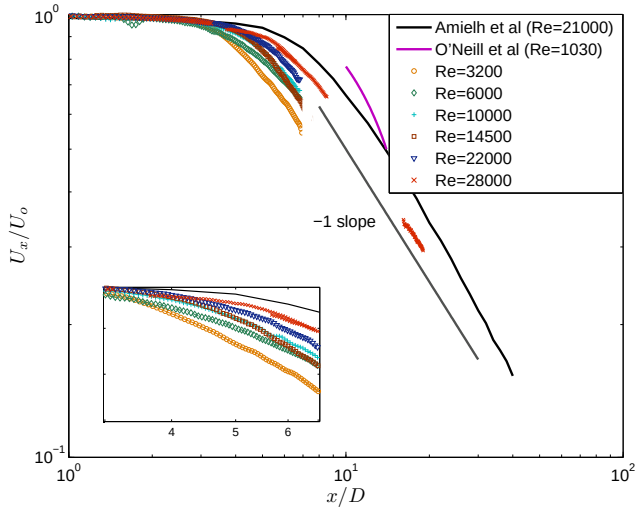

Figure 2.6: Average normalized axial velocity versus downstream distance compared to $(x/D)^{-1}$ profile, LDA data from Amielh et al. [1996] and low Reynolds number data from O'Neill et al. [2004].

for mean and fluctuating quantities and a ' represents rms values.
For increasing Reynolds numbers, the decay of normalized streamwise velocity along the jet's axis given in Figure 2.6 approaches the one of LDA data and shows a satisfactory continuity between near and far field measurements. Such decay exhibits also the expected $(x/D)^{-1}$ behaviour described in Liepmann and Gharib [1992]. Measurements up to $6D$ for different Reynolds numbers show a similar decay profile which moves downstream as the Reynolds number increases, as displayed in figure inset. Comparison to the results reported in O'Neill et al. [2004],obtained at a Reynolds number of 1030 with a conical nozzle, confirms the reported trend of axial velocity decay even at low Reynolds numbers.

Normalized profiles of axial and vertical velocity rms versus downstream position are depicted respectively in Figure 2.7 and 2.8, where a quite good agreement with LDA data is noticeable at high Reynolds numbers for the axial velocity. The decay of the profile is slightly above LDA data at 5-6D, where the shear layers begin to merge. At lower Reynolds numbers this merging is attained farther from the nozzle, and an increase in rms is observed. In Figure 2.9, normalized axial and vertical velocity rms values taken at $x/D = 5$ are shown as a function of Reynolds number. This position is approximately that of maximum rms as shown in Figures 2.7 and 2.8. The observed decrease is in agreement with a $-1/4$th power of the Reynolds number, thus suggesting that the rms fluctuations scale as $Re^{3/4}$.

Present data are also validated with respect to radial velocity profile very close to the nozzle ($x/D = 0.2$). Comparison to LDA data and to empirical fully developed pipe flow

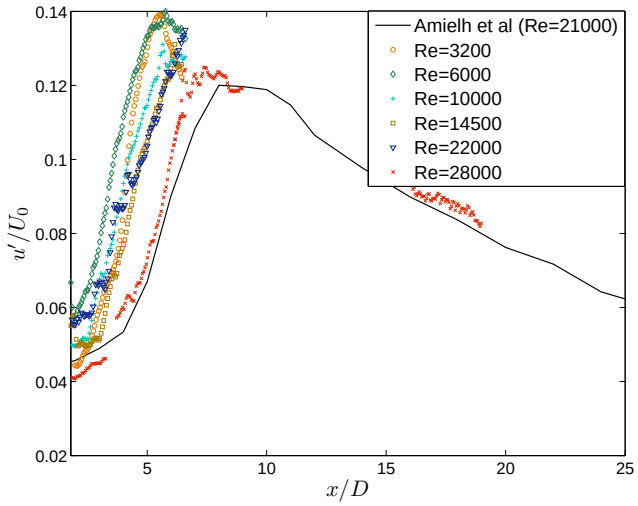

Figure 2.7: Rms of axial velocity, i.e. at y/D=0, vs downstream distance compared to LDA from Amielh et al. [1996].

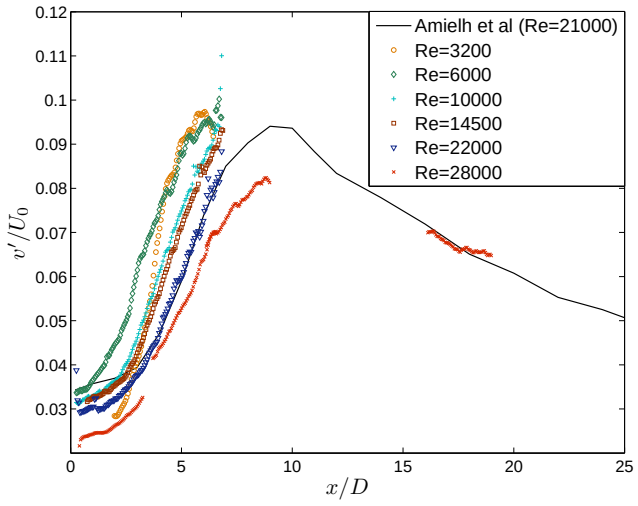

Figure 2.8: Rms of vertical velocity vs downstream distance at y/D=0 compared to LDA from Amielh et al. [1996].

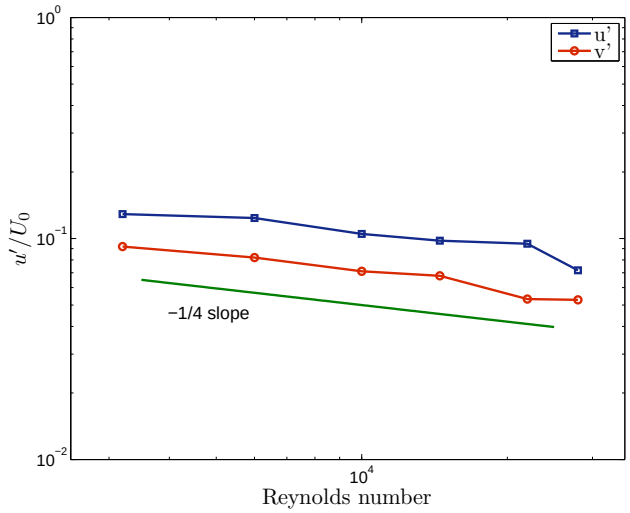

Figure 2.9: Normalized rms of axial and vertical velocity versus Reynolds number at $x/D = 5$ compared to $Re^{-1/4}$ slope.

power law $(1 - 2r/D)^{1/n}$ with $n = 6.5$ described in Mi et al. [2001] are shown in Figure 2.10 with collected data matching fairly well the reference profiles. The smooth ends at the jet's boundaries (r/D=0.5) are also a consequence of the free-slip condition due to the nozzle not flushing with the tank wall, as described in Romano [2002]. These findings confirm the hypothesis of completely developed turbulent pipe flow at the nozzle exit.

An evaluation of the way the jet spreads in the ambient fluid is given by Figure 2.11, where momentum thickness versus downstream location x/D is provided versus Reynolds number and compared to results in Cohen and Wygnansky [1987]. The momentum thickness increases along the downstream coordinate, as found by Cohen and Wygnansky [1987], whereas it decreases as Reynolds number grows reaching an almost asymptotic state for $Re > 15000$. The systematic difference between Cohen and Wygnansky [1987] data (obtained at $Re \approx 27000$) and present data may be explained by the different boundary conditions at the nozzle exit, i.e. momentum thickness, and free-slip condition which, as described in Romano [2002], leads to higher values of momentum thickness.

2.5 Crosswise instantaneous and mean velocity fields

The fluid mechanics phenomena taking place on longitudinal planes considered in previous sections are closely related to those on crosswise planes leading to fully three-dimensional vortical structures (Klaasen and Peltier [1988], Liepmann and Gharib [1992] and Sbrizzai et al. [2004]). In axisymmetric jets, the ejection of secondary transverse fluid related to Kelvin-Helmholtz shear layer primary instabilities allows the formation

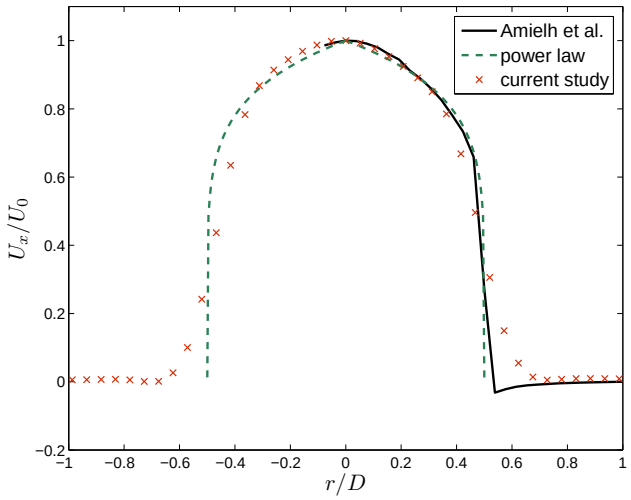

Figure 2.10: Mean velocity profile at $x/D = 0.2$ and $Re = 22000$ compared to experimental data from other authors and empirical power law for turbulent pipe flows.

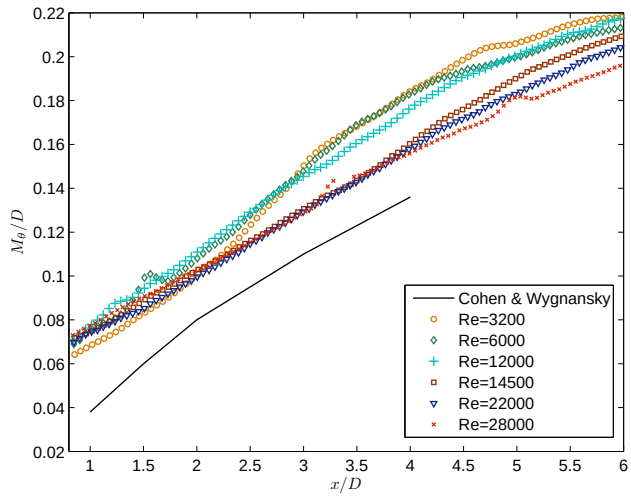

Figure 2.11: Momentum thickness M_θ variation along x/D coordinate for different Reynolds numbers compared to Cohen and Wygnansky [1987] data.

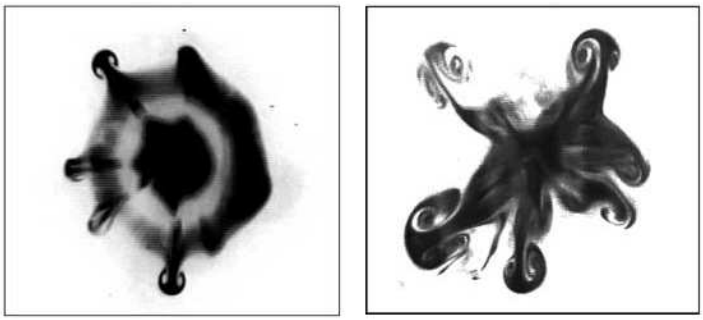

Figure 2.12: Frontal view of a nozzle jet at two downstream positions $x/D = 3$ and $x/D = 4$, $Re = 6600$. Courtesy from Romano [2002].

of secondary double counter-rotating structures, resembling a "mushroom" shape in the plane perpendicular to the main flow (Liepmann and Gharib [1992], Romano [2002] and Sbrizzai et al. [2004]). In Figure 2.12 from Romano [2002], obtained from a nozzle jet with free-slip BC by means of Laser Induced Fluorescence (LIF), these "mushroom" structures are clearly visible at two downstream positions, respectively $x/D = 2$ and $x/D = 3$.

In this work, velocity measurements on cross-planes make it possible to investigate secondary instabilities from $x/D = 0.75$ up to $x/D = 4.5$, approximately where the potential core vanishes.

The high-speed acquisition method allowed the visualization of the transient secondary structures evolution, as shown in the series of pictures given in Figure 2.13. The snapshots represent a close up on the upper-left area of the cross plane where the formation of a mushroom-like structure takes place, i.e. at $x/D = 2.5$, for two different Reynolds numbers, namely 3200 and 14500. For the sake of clarity only one image every 0.008 seconds, nearly 0.3 integral time scales, was displayed in the picture for $Re = 3200$, whereas one image each 0.15 integral scales was used for $Re = 14500$ data. The formation and evolution of the two counter-rotating vortices can be appreciated; in particular the life time of such structures is approximately equal to 1 integral time scale. The picture is similar for the data at $Re = 14500$. The vector field averaged over 5000 images (about 10 s, i.e. more than 100 integral time scales) at $x/D = 1.5$ and $Re = 4800$ is presented at the top of Figure 2.14. The empty central area is the effect of a computation mask which was set prior to PIV processing to avoid the large velocities at the jet centerline which give almost uncorrelated image pairs. The actual pipe outlet shape is depicted as the gray circle. The circular area close to the pipe outlet characterized by low velocities values is due to the travelling vortex rings. As the vortex passes by in fact, fluid is ejected; this process is compensated by the subsequent ring's roll-up during which a strong fluid entrainment takes place thus leading to the observed average velocity field. For large radial distances (around 1D) on the other hand, there is a negative radial velocity, i.e. a positive entrainment stemming from secondary instabilities, as shown in instantaneous plots and predicted by the model presented in Section 2.2 (Figure 2.3). It

is also interesting to note that the velocity field under investigation is not affected by major swirling.
For increasing Reynolds numbers, a similar field is noticeable as shown at the bottom of Figure 2.14, for $Re = 19300$, where fluid entrainment is again visible up to the border of the imaged area. As expected, the average velocity field magnitude is considerably larger than the $Re = 4800$ case and the region around the pipe outlet where the velocity field is attenuated is less evident. It may be noticed that the velocity field in the $Re = 19300$ case features a higher degree of symmetry with respect to the center of the pipe than the $Re = 4800$ case. As the acquisition time increases, in terms of flow integral scales, such velocity fields are expected to exhibit an ever growing symmetry and this is confirmed by the findings in Figure 2.14. Keeping the same acquisition time, as the Reynolds number increases, the acquisition window covers more integral scales for the highest Reynolds number case.
The resulting radial and azimuthal mean velocities are presented in Figure 2.15 for $Re = 14500$ with positive U_r pointing outwards. The mean U_r field, displayed on the left side of Figure 2.15, normalized by the flow velocity U_0, reveals a strong dependence on the downstream distance: up to $x/D = 1$ the field shape is still unaffected by secondary structures, and vortex rings action is predominant. From $x/D = 1.5$ up to 2.5, instabilities of the potential core begins to be visible and consequently the velocity field shows an increasing dependence of the radial velocity on the azimuthal angle. In the last downstream position, $x/D = 4.5$, the presence of secondary vortex structures is substantial and modifies the velocity field's shape up to $r/D = 2$. The absolute value of the radial component U_r increases considerably with x/D, both outwards up to -0.25U_0, and inwards up to 0.25U_0. On the other hand, the mean U_θ (azimuthal velocity) distribution is quite independent from x/D as may be seen in the right side of Figure 2.15. In particular, for high x/D, the field retains its shape and no far-field modification is evident. This behaviour may be related to the counter-rotating features of vortical structures that cancels out the U_θ component on average. It is important to point out that the azimuthal velocity attains average values which are as small as $\pm 0.001 U_0$ at all downstream distances. The behaviour of average velocity components as a function of Reynolds number is summarized in Figure 2.16 at four downstream positions. Those values have been obtained by sorting positive (fluid ejection) and negative (fluid entrainment) motions and by averaging the data over the entire region under investigation. All velocity components at the different distances decrease with respect to Reynolds number not far from the -1/4 slope (depicted as reference in Figure 2.16). This is the same behaviour derived for the rms velocities on a longitudinal plane (Figure 2.9), thus indicating that on the average the secondary instabilities on cross-planes are driven by the same mechanism (at least with respect to Reynolds number effects) which gives rise to primary instabilities on longitudinal planes. On a statistical basis, this mechanism can predict the ones from the others and viceversa.
The behaviour of velocity fluctuations provides further insight on the phenomenon. In Figure 2.17, radial profiles of rms values for radial and azimuthal velocities are presented for $Re = 14500$. Radial rms were obtained by averaging four data sets lying on two mutually perpendicular axes passing by the pipe outlet's geometric center. The values of turbulent fluctuations, while decreasing with the radial distance, are almost constant

with x/D up to $x/D = 3.5$, where an increase is observed, matching the onset of fully three-dimensional instability as reported by Liepmann and Gharib [1992]. In comparison to u_r fluctuations, those in u_θ appear to attain lower values (less than 1/20) and consequently seem to be weakly related to jet's mixing. The u'_r and u'_θ rms curves at fixed x/D for different Reynolds numbers are depicted in Figure 2.18. Radial velocity data are characterized by the following pattern: the rms level decreases up to $Re = 9600$ and then increases for higher Reynolds numbers, in particular for $r/D < 0.5$, that is close to the pipe outlet's rim. A similar behaviour was pointed out in Liepmann and Gharib [1992], for a Reynolds number of approximately 10000; it was related to jet's initial boundary layer transition to turbulence. Azimuthal velocity rms profile shows a similar behaviour, although with much smaller values.

2.5.1 Mean entrainment rates

The observations made in the previous sections confirm the average relationships among longitudinal and transverse vortical structures. Thus, the entrainment rate introduced in Section 2.2 can be evaluated by combining equations 2.2.2, 2.2.3 and 2.2.4

$$\frac{d(Q_r(x,R)/Q_0)}{d(x/D)} = \frac{D}{Q_0}\int_0^{2\pi} RU_r(x,R)\mathrm{d}\theta \tag{2.5.1}$$

with the already mentioned normalization. The above formulation states that the mean entrainment rate at a specific downstream distance x/D will be derived by integrating the radial velocity U_r along a circular path centered on the pipe's outlet. It is of interest to assess how for $R < 2D$, the entrainment rate is affected by the radial coordinate as it can provide a good insight on the role of different vortical structures in such process.

The entrainment rate derived by the average radial velocity field U_r is displayed in Figure 2.19 at downstream position $x/D = 0.75$ for different Reynolds numbers. For $r/D < 0.5$ the curves feature a slightly negative rate, whereas for larger radial distances, the entrainment rate level becomes positive and increases up to an almost asymptotic value. The features of the reported profiles can be explained considering that the effect of primary instability structures is predominant at this downstream position and vortex rings affect noticeably the entrainment. As shown in Figure 2.14, for radial distances shorter than $0.5D$, there is still an ejection of flow which is responsible for the negative peak. On the other hand, the increase achieved for r/D in the range 0.6-0.8 stems from the primary vortex rings roll-up, whose effect is most relevant in a limited flow region and vanishes in the cross-plane far field ($r/D > 1$). For large r/D, the entrainment rate is expected to be a constant independent from radial distance and this is confirmed by the results shown in Figure 2.19.

Figure 2.19 provides also information on Reynolds number effect on entrainment, in particular on the negative entrainment $r/D < 0.5$ region and the asymtpotic behaviour of normalized entrainment rate. About the latter effect, it is worth pointing out that the effect of secondary instabilities is less evident at higher Reynolds number regimes, as

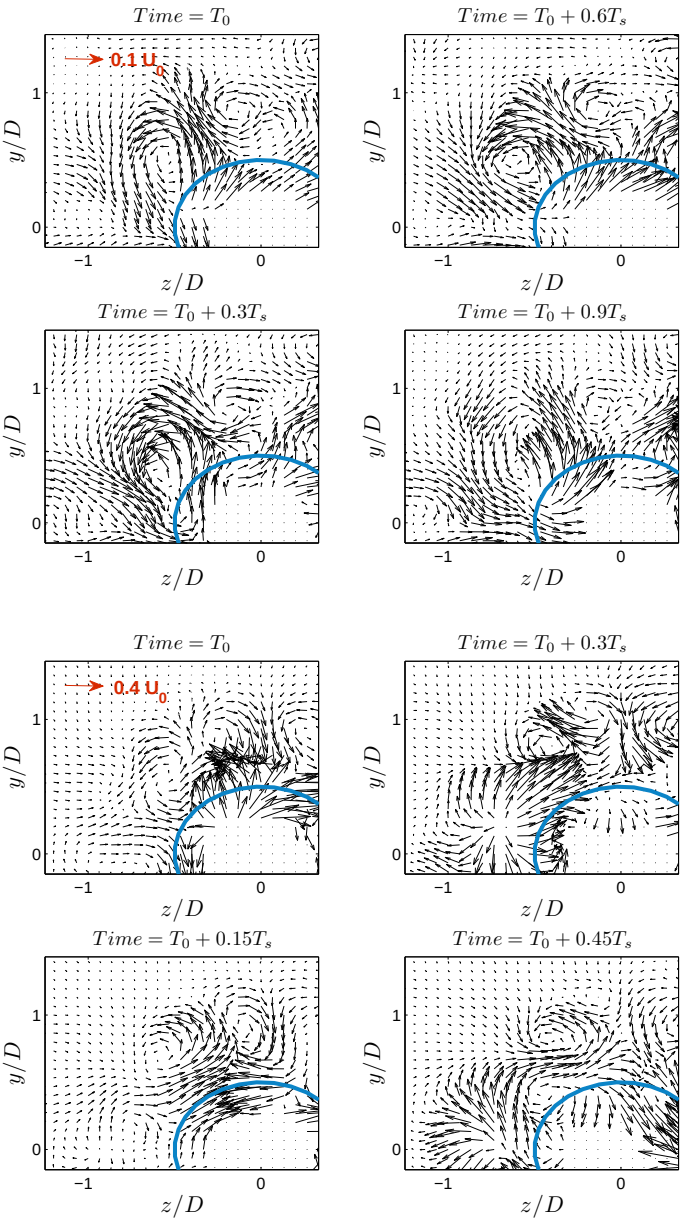

Figure 2.13: Snapshots of cross-plane transient structures for $x/D = 2.5$, $Re = 3200$ (first four pictures at the top) and $Re = 14500$ (four pictures at the bottom). U_0 for $Re = 3200$ case has been used as a reference for both figures.

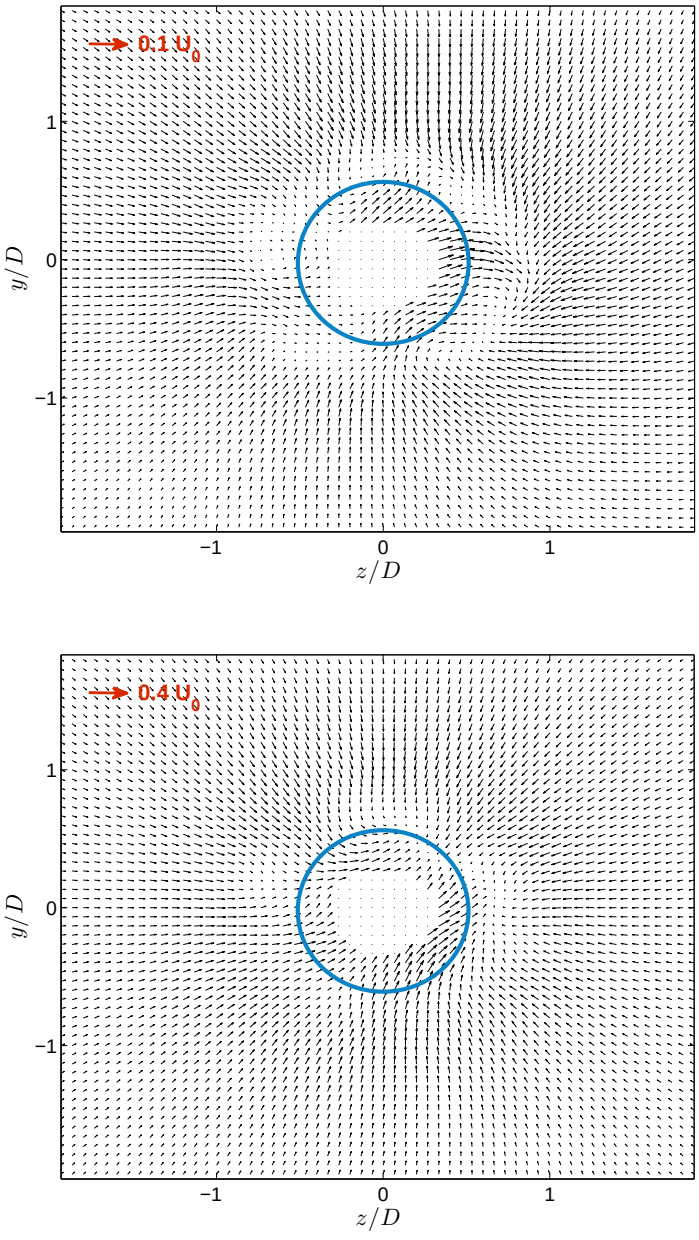

Figure 2.14: Mean velocity field for $x/D = 1.5$ at $Re = 4800$ (top) and $Re = 19300$ (bottom). U_0 for $Re = 4800$ case has been used as a reference for both figures. Grey circle represents pipe outlet's rim.

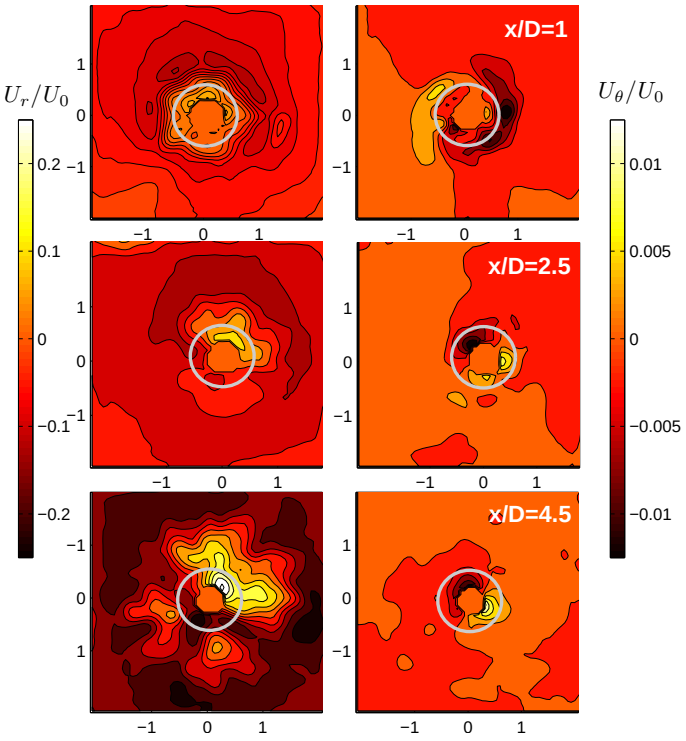

Figure 2.15: Normalized U_r and U_θ mean field for $Re = 14500$ at various x/D. The grey circle represents the pipe outlet's rim.

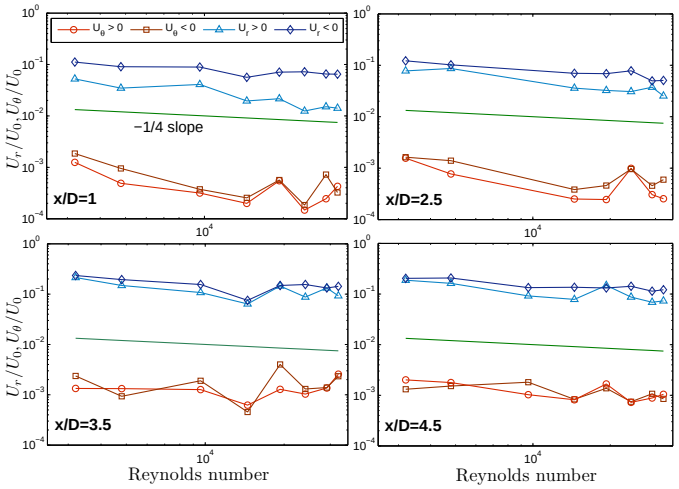

Figure 2.16: Radial (U_r) and azimuthal (U_θ) average velocity versus Reynolds number at different downstream positions.

suggested also by Figure 2.15.
These observations, combined with the results from Figure 2.15, confirm that for cross-planes farther away from the nozzle, secondary vortical structures become more efficient at entraining fluid and, when the potential core ends, they take full control of the entraining process.
The initial negative entrainment region visible in Figure 2.19, which was also reported by Hassan and Meslem [2010] at $r/D = 0.8$ for $x/D = 4$, shows a strong dependence on Reynolds number almost vanishing for $Re > 14500$.
In section 2, the balance between axial and radial volumetric flow allowed to derive model equations for the average radial velocity as well as for the entrainment rate in the form of model equations A and B depicted in Figure 2.3. Comparison of the proposed models against experimental data is shown in Figure 2.20 where average radial data and entrainment rate at $x/D = 4.5$ and at different Reynolds numbers were plotted against $H = K_u R/(x - x_p)$. Such a downstream position was chosen to verify as much as possible the assumption of self-similarity even in such a region close to the jet outlet. The parameters K_u and x_p are taken respectively equal to 6 and 0 as in Malmstrom et al. [1997].

Experimental data show that for the radial velocity, the agreement is rather poor especially for $Re \leq 14500$ and $H > 1$. However the simple models seem to account for the main features of measured data and relative error bars for $Re > 14500$ and $H < 1$. Specifically, model A seems to be more suited for data around $Re \approx 20000$, while model B is better describing the other data. Results for the entrainment rate show that model B prediction of an initial negative entrainment region followed by a positive negative entrainment region is confirmed by experimental data for $Re < 10000$. For $Re > 10000$

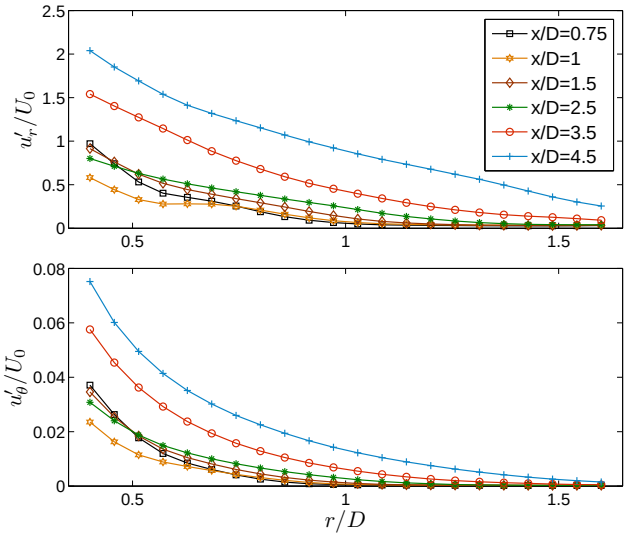

Figure 2.17: Rms of radial velocity u_r (top) and azimuthal velocity u_θ (bottom) versus radial distance in cross-planes at $Re = 14500$ for various downstream distances x/D.

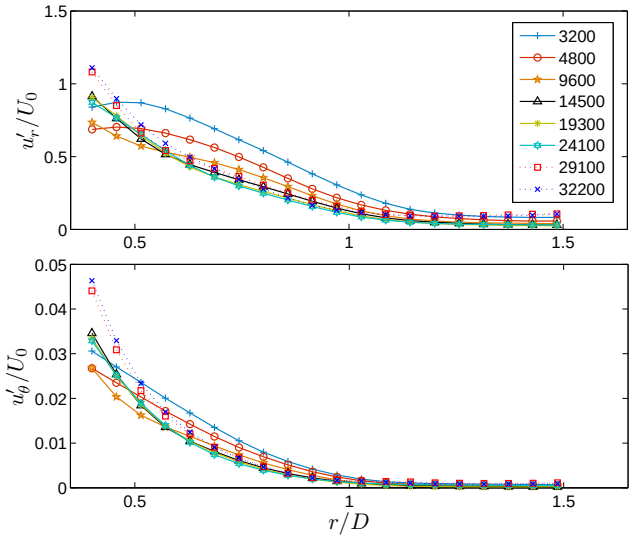

Figure 2.18: Rms of radial velocity u_r (top) and azimuthal velocity u_θ (bottom) versus Reynolds number at $x/D = 1.5$.

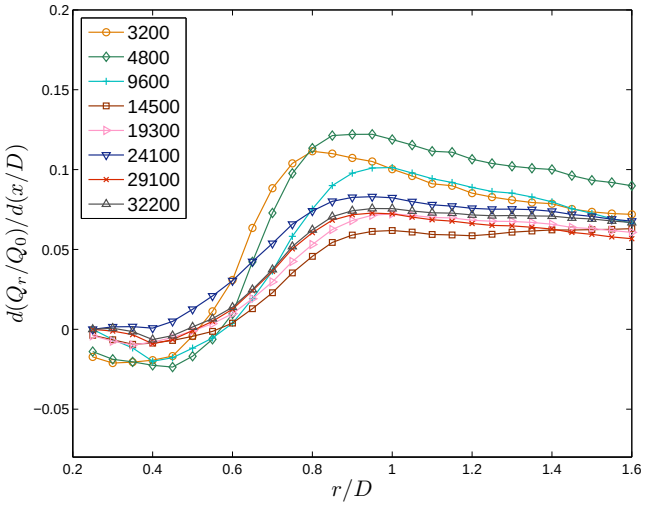

Figure 2.19: Normalized entrainment rate at downstream position $x/D = 0.75$ for different Reynolds numbers.

model B does not recover the sign of entrainment rate for $H < 1.3$, predicted by model A, while following satisfactorily the experimental data for $H > 1.3$.
Clearly, the choice of the parameters in the model (K_u and x_p) could be one of the reasons for the observed differences in comparison to data.

2.5.2 Velocity correlation, Reynolds Stresses and Turbulent Kinetic Energy

The analysis of transverse structures can explain some of the features observed in previous sections in relation to the effect of Reynolds number as also investigated by Liepmann and Gharib [1992]. These authors found that the number of secondary structures grows up to $Re = 10000$ (while dropping for larger values), whereas their size appears to be inversely proportional to Reynolds number up to $Re = 10000$ (and nearly constant for larger values). This behaviour was associated to the transition to turbulence of the boundary layer at the nozzle exit which in turn affects the shear layer thickness.
In the present work, a preliminary visual investigation of the flow features did not show an evident increase in the number of counter-rotating vortical structures in cross-planes with Reynolds number. The reason lies in the different inlet conditions of the present work, i.e. a long pipe as opposed to a smooth contraction in Liepmann and Gharib [1992].

Further insight was provided by the Reynolds stress distributions, based on radial and azimuthal velocity components turbulent fluctuations, namely $< u_\theta u_r >$.
Figure 2.21 depicts Reynolds stress distributions in cross-planes at $x/D = 2.5$ and $x/D =$

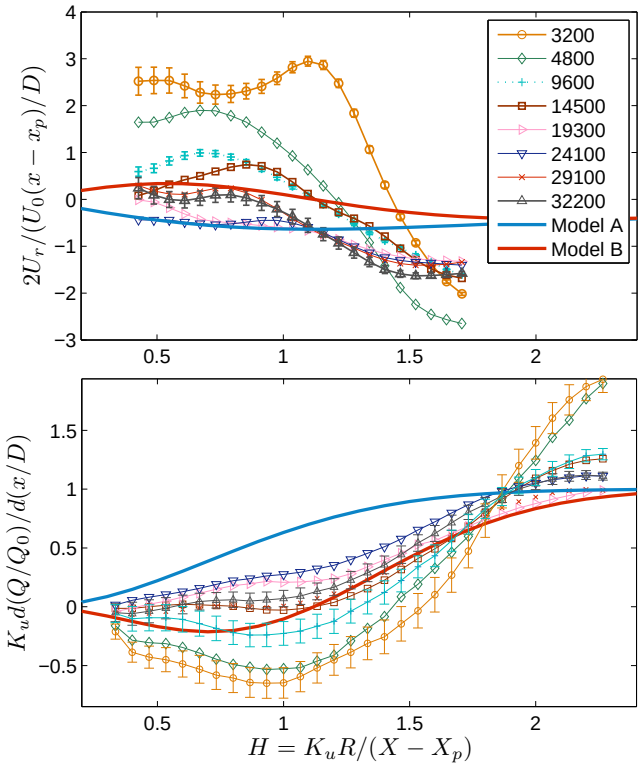

Figure 2.20: Average radial velocity (top) and entrainment rate (bottom) versus $H = K_u R/(x - x_p)$ at $x/D = 4.5$.

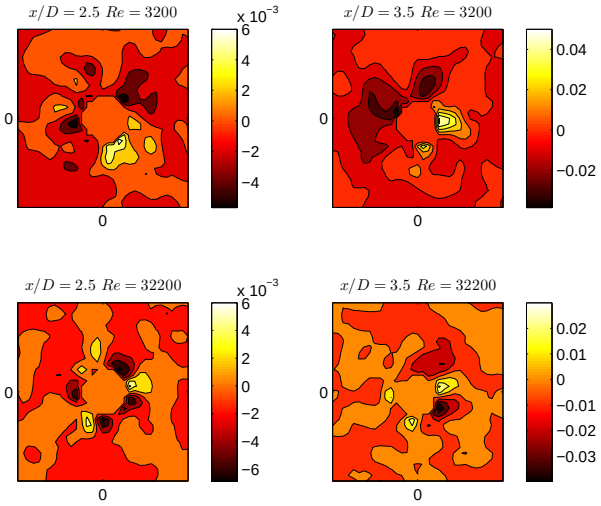

Figure 2.21: Reynolds stress distribution based on u_θ,u_r components normalized by U_0^2 at two different x/D positions and Reynolds numbers.

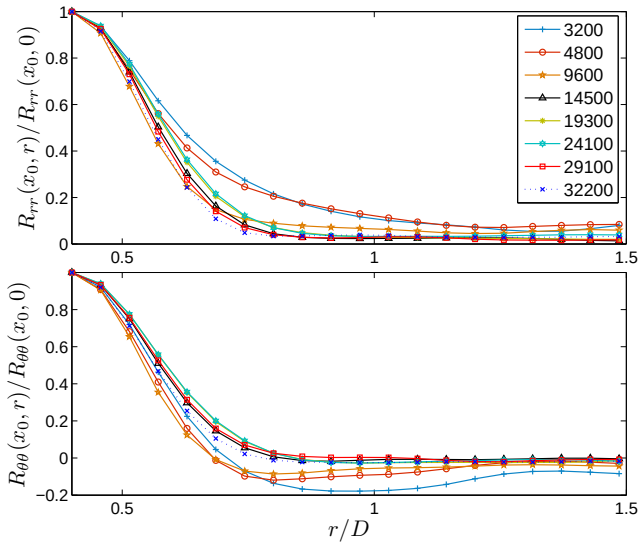

Figure 2.22: Normalized radial (top) and azimuthal (bottom) velocity correlation functions at $x/D = 3.5$ for different Reynolds numbers.

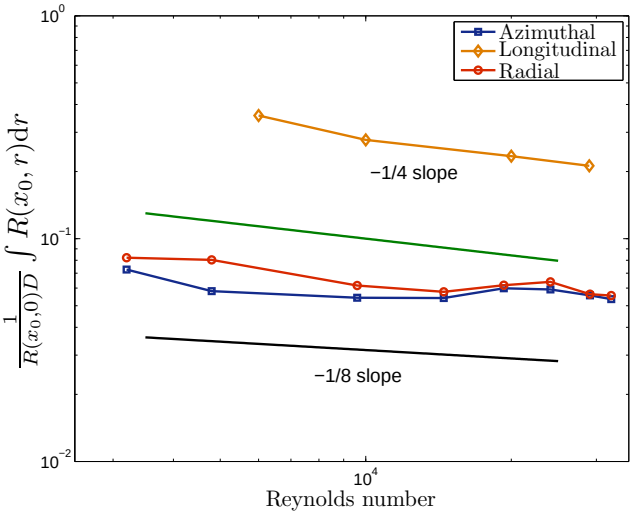

Figure 2.23: Integral scales derived by azimuthal and radial velocity correlation functions versus Reynolds number.

3.5 for different Reynolds numbers. The velocity fluctuations related to the counter-rotating, mushroom-shaped, structures are visible as regions of high, reverse sign, stress. The number of these regions is nonetheless unaffected by a Reynolds number variation of nearly a decade. This is in agreement with the work of Liepmann and Gharib [1992], where the number of modes increased slowly with Reynolds number after pipe's nozzle boundary layer transition. In the current work, the experimental set-up in fact leads to a fully developed turbulent flow and consequently a change in the number of modes should not be expected as reported by Liepmann and Gharib [1992].
Regarding the average size of cross-planes vortical structures, it was assessed by means of radial and azimuthal velocity correlation functions defined respectively as

$$R_{rr}(x_0,r) =< u_r(x_0)u_r(x_0+r) >, R_{\theta\theta}(x_0,r) =< u_\theta(x_0)u_\theta(x_0+r) > \qquad (2.5.2)$$

Where the reference position x_0 was set right inside the pipe's outlet rim (at $r/D \approx 0.45$) and r direction represents the radial position with respect to pipe's center. Correlation functions were then normalized to their initial value, $R_{rr}(x_0,0)$ and $R_{\theta\theta}(x_0,0)$, and were subsequently spatially averaged from four data sets lying on two mutually perpendicular axis passing by the pipe's center, as for rms calculations presented in Figures 2.17 and 2.18. Figure 2.22 shows such correlation functions calculated at $x/D = 3.5$ for different Reynolds numbers. The radial correlation profiles show a dependance on Reynolds number with decreasing levels of correlation as Reynolds number increases. For $Re \leq 4800$, R_{rr} retains 50% of its starting value up to $r/D \approx 0.65$ whereas at the same radial distance for the $Re = 32200$ case it is as low as 25%. Furthermore, R_{rr} is above 10% of its initial value up to $r/D \approx 1$ for lower Reynolds numbers, whereas such relative

value is reached already at $r/D \approx 0.7$ at $Re = 32200$. These findings confirm that the average spatial extension in the radial direction of counter-rotating, streamwise vortical structures decreases with growing Reynolds for $Re < 10000$ followed by an asymptotic behaviour.
Similarly, at the bottom of Figure 2.22 the profile of $R_{\theta\theta}$ for different Reynolds numbers is provided. Differently from the radial correlation, the azimuthal correlation shows negative values due to the vortical structures which roll up inwards and is related to the spatial extension of such structures in the azimuthal direction. For increasing Reynolds number the radial position at which the anti-correlation peak is attained decreases confirming again the shrinking of vortices. $R_{\theta\theta}$ is less subject to this effect than R_{rr}, arguably because of the double counter-rotating nature of the structures under investigation, which dampens the azimuthal component of velocity in the spatial-averaging process.
A further insight on the dependance of velocity correlation functions on Reynolds number is given by Figure 2.23, where normalized integral scales obtained by previous functions have been plotted as a function of the Reynolds number. Radial and azimuthal integral scales show both the same profile, confirming the decrease of the average spatial extension of secondary vortical structures for increasing Reynolds numbers with similar results found at other downstream positions. The given results bear an important resemblance to entrainment rate findings presented in the previous paragraph as to the Reynolds number dependency. The entrainment rate appears in fact to be affected by the velocity spatial correlation induced in cross-planes by the secondary structures. The efficiency at entraining fluid relatively to a reference velocity decreases with Reynolds number and attains an asymptotic state for $Re > 10000$ as reported in Figures 2.19 and 2.20.

Turbulent kinetic energy (TKE), defined as $u_r'^2 + u_\theta'^2$, was calculated in planes perpendicular to jet's main velocity in order to give a better insight on how the onset of fully three-dimensional turbulence influences the energy distribution. In Figure 2.24, the distribution of TKE for $Re = 3200$ at different downstream position is shown. TKE values, normalized to the square of the flow speed U_0, show two well distinct regimes. TKE grows steadily inside the $r/D = 1$ region up to $x/D = 2.5$. This effect, described by Hassan and Meslem [2010] in their work, is confined to an area close to the pipe's outlet and stems from the primary instability structures which evolve spatially. As the downstream position increases to $x/D \approx 2$, these structures strengthen and undergo a pairing process which increases the TKE value locally.
On the other hand, TKE distributions for positions $x/D > 2.5$ are characterized by high levels all over the investigated area. In particular the shape of the TKE distribution for such cross-planes shows an increase of TKE levels in the outer area where $r/D > 1$, whereas the region close to the pipe's outlet, where the effect of vortex rings is most relevant, does not undergo noticeable changes.

This phenomenon is related to the effect of the vortical crosswise structures, which have shown to develop fully in the area far from the pipe's nozzle as the downstream position increases, boosting the kinetic energy. This findings match those from Figure 2.8 where rms of vertical velocity features a similar increase versus x/D.
TKE distributions at cross-plane $x/D = 4.5$ for different Reynolds numbers are shown in Figure 2.25. For low Reynolds numbers, namely $Re \leq 4800$, relevant TKE values

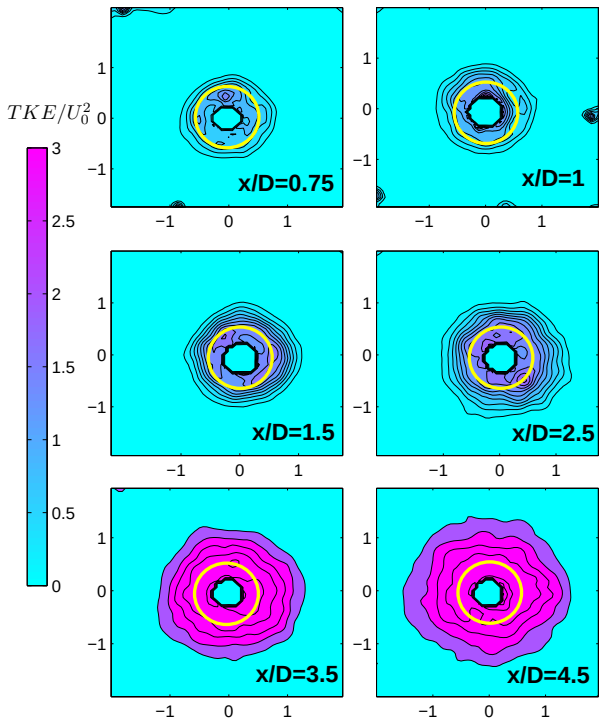

Figure 2.24: Normalized TKE distributions for different x/D positions at $Re = 3200$. The yellow circle represents the rim of the pipe's outlet.

are observed up to $r/D \approx 1.5$ having streamwise structures an important impact on the flow field. The normalized TKE distribution for higher Reynolds numbers shows that the region affected by high TKE levels shrinks progressively as the Reynolds number raises, remaining nearly constant from $Re \geq 29100$. These findings, together with the results from velocity correlations, suggest the existence of an initial regime, for $Re < 10000$, where the size of the cross-planes vortical structures decreases having an effect on turbulent energy distribution which do not scale with Reynolds number. For Reynolds numbers > 10000, the size of these structures reaches an asymptotic value and the level of TKE stays nearly constant as shown in Figure 2.25.

2.5.3 Spectral analysis

The high temporal resolution achieved in the present work by means of a high-speed camera made it possible to derive also spectral functions from cross-planes acquisitions. The intrinsic axisymmetric features of the flow visible in these planes suggested the use of spectral functions that could highlight the spatial coherency of the velocity field.
To this end, a valuable tool is represented by the coherency spectrum, as reported in

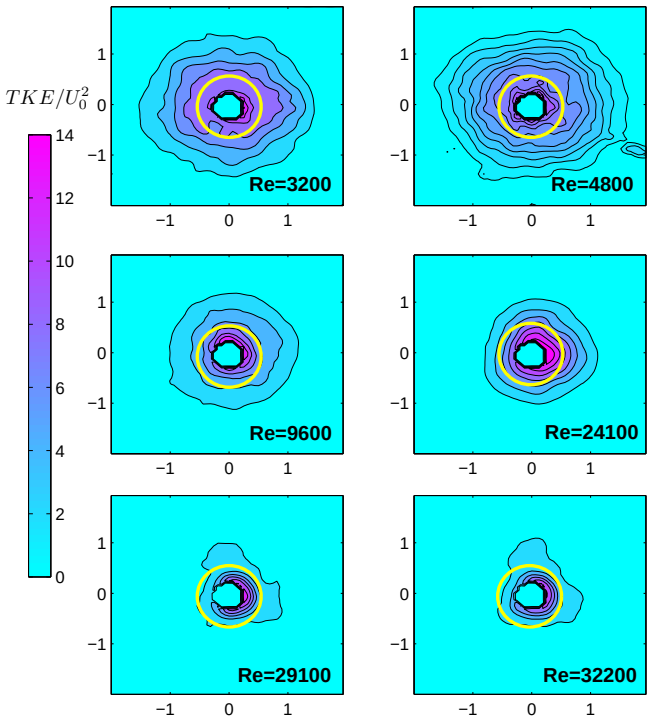

Figure 2.25: Normalized TKE distributions at $x/D = 4.5$ versus Reynolds number. The yellow circle represents the nozzle's rim.

Sato et al. [2002] and Sbrizzai et al. [2004]. In particular in Sato et al. [2002], coherency spectra were employed to identify frequency modes in a planar turbulent jet direct numerical simulation. The work by Sbrizzai et al. [2004] built on this perspective by taking advantage of coherency spectra to identify jet preferred-mode frequency in a Large Eddy Simulation of a multi-phase confined turbulent round jet. As described by Sato et al. [2002] and Sbrizzai et al. [2004] the use of the coherency spectrum reduces the influence of the broad-band background energy, a feature which is particularly relevant for experimental data. This in particular makes it an effective tool in this study in order to highlight the spatial coherency stemming from large vortical structures such as vortex rings.

Following the definition given in Sato et al. [2002], the coherency spectrum is defined as

$$Coh_{u_r u_r}(f) = |\int_{-\infty}^{+\infty} C_{u_r u_r}(\tau) exp(-2\pi j f \tau)\,\mathrm{d}\tau.| \tag{2.5.3}$$

where $C_{u_r u_r}$ is the time-space correlation of the radial velocity component at two opposing points, A_i and B_i, with respect to pipe nozzle's center $C_{u_r u_r}(\tau) = \overline{u_{A_i}(t+\tau) u_{B_i}(t)}$ as shown in Figure 2.26.

In order to further reduce the high-frequency noise and enhance the spatial coherency features within the entire cross-plane, the coherency spectrum was calculated for 32 couples of points from (A_1, B_1) to (A_{32}, B_{32}) positioned on a circle centered on the nozzle's outlet and their spectra were finally averaged. The right hand side of Figure 2.26 gives a graphical representation of the described calculations pointing out how points couples are chosen and comparing it to the correlation functions given in equations 4.2. The analysis was carried out in two cross-planes locations, on a circle of radius respectively $r = 0.5D$ and $r = 1.17D$. This choice allowed to separate the effect of primary instability, close to the pipe's nozzle, and secondary streamwise vortical structures, which have shown to develop far from pipe's nozzle, where vortex rings impact on flow is reduced. The radial component u_r was employed in such computations because of its strong correlation to both vortex rings and crosswise vortical structures as shown in the previous paragraph.

In Figure 2.27 a comparison between spectra calculated from points close the pipe's outlet is given for four different Reynolds numbers at $x/D = 1$. Coherency spectra were normalized to flow velocity U_0 and characteristic length D and plotted versus Strouhal number $St = fD/U_0$. At $Re = 3200$ a strong peak is noticeable which corresponds to a high degree of spatial correlation at $St \approx 0.54$ and this behaviour is due to the vortex rings shedding at the given downstream distance. The reported value of the Strouhal number falls within the range [0.24-0.64] given by Gutmark and Ho [1983] for the preferred mode of various jet configurations, with Reynolds number within the range 4.5 10^3-8 10^5.

As the Reynolds number increases, a damping effect on the spectrum's peak is visible, although the frequency of the peak is not changing, being correlated to the jet's vortex rings shedding frequency. This implies that the latter is linearly dependent on velocity and thus on Reynolds number. Nonetheless, as the peak's magnitude decreases, the energy correlated to the spectrum's high-frequency components grows accordingly. This

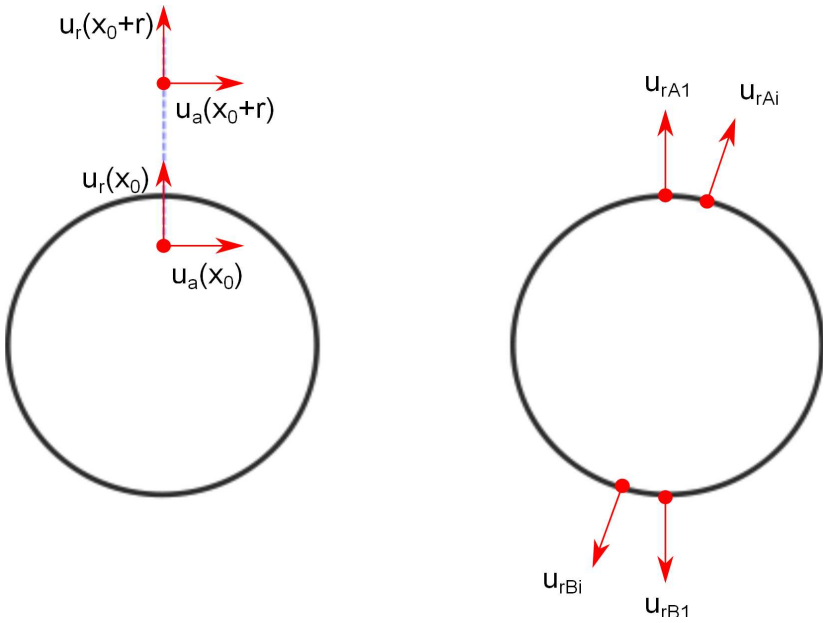

Figure 2.26: Graphical representation of radial (u_r) and azimuthal (u_a) velocity correlation functions (left hand) and two times correlation function $\overline{u_{A_i}(t+\tau)u_{B_i}(t)}$ (right hand). Circles represent pipe's nozzle.

effect may be explained by the turbulent energy transfer which takes places between primary and secondary vortical structures as the flow develops fully three-dimensional turbulence.

These findings match those reported for rms in Figure 2.18. As x/D increases, the potential core approaches its end and the spatial coherency induced by the primary vortical structures is progressively lost.
At a location near to $x/D = 2.5$ the development of crosswise structures, as a consequence of the fully three-dimensional turbulent flow, modifies the shape of the spectra making the preferred frequency much less visible. This is more evident when looking at spectra derived by points lying on a circle with radius $r \approx 1.2D$ as shown in Figure 2.28, where averaged coherency spectrum is here shown for $x/D = 3.5$ and $Re = 4800$. No preferential frequency is visible in this case, since streamwise structures do not evolve coherently within cross-planes having no axisymmetric properties and the primary instability effect is reduced.

2.6 Conclusions

In this Chapter, a thorough study of the effect of Reynolds number on the relation among primary and secondary structures developing in a fully-developed turbulent pipe jet and

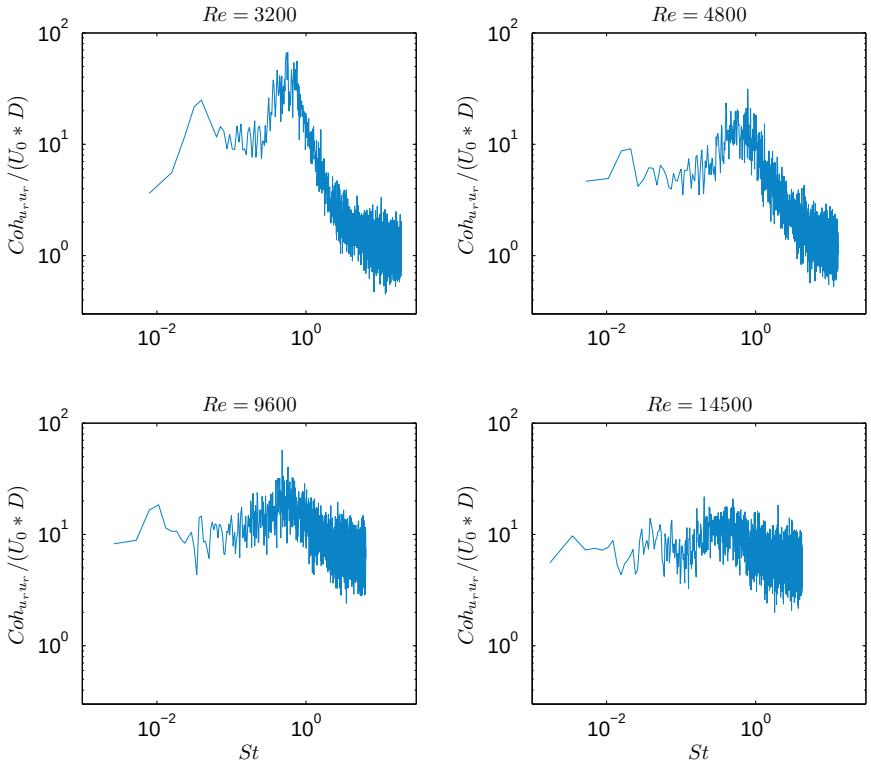

Figure 2.27: Normalized average coherency spectra for u_r derived by points lying in the shear layer ($r/D = 0.5$) at downstream position $x/D = 1$ for different Reynolds numbers.

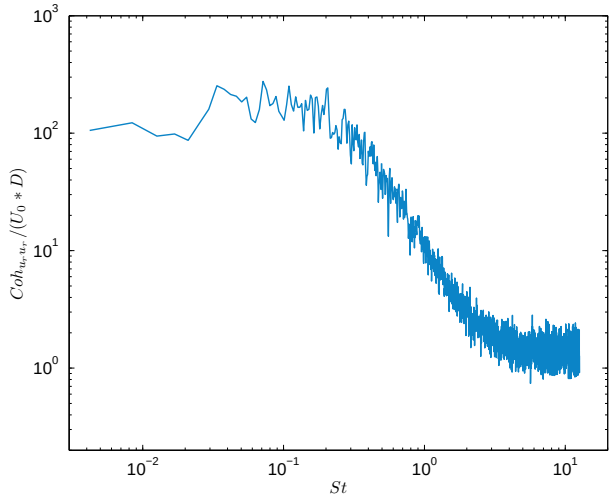

Figure 2.28: Normalized averaged coherency spectum derived by points lying on a circle far from nozzle's outlet ($r/D \approx 1.2$) for $Re = 4800$ and $x/D = 4.5$.

in particular on the effects on entrainment rate is presented. As explained before, this is a preliminary analysis before the investigation of more complex flows, in which a rod-like dispersed phase is added.
The results on the axial plane confirm those obtained by other authors, while highlighting the effect of Reynolds number on statistical moments. The potential core extension increases with Reynolds number, whereas the rms values of the two velocity components on the plane decrease with Reynolds number with a power law with exponent equal to -0.25, as reported in Figure 2.9. Simultaneously, the momentum thickness of the jet shear layer increases linearly with x/D with a similar behaviour with respect to Reynolds number if larger than 10000.
Regarding cross-planes, a relation based on the average balance among axial and radial flow rates is considered to derive analytical models for the radial velocity on cross-planes and for radial and axial flow rates as functions of axial and radial distances. One of the models is in good agreement with experimental data expecially for Reynolds numbers larger than 10000, as indicated in Figure 2.20. Therefore, close to the jet outlet there is a positive radial flow rate (towards the external part of the jet) balanced by a slight reduction in the axial flow rate. On the other hand, far from the jet, there is a negative radial flow (towards the internal) balanced by an increase of the axial flow. While the second of these results is well known, the first clearly improves the simple result for the potential core in which the radial flow rate is simply zero with a constant axial rate.
The radial and azimuthal velocity components on those cross-planes increases with the axial distance, while decreasing with Reynolds number for a given axial distance. The power law for this decrease is again close to -0.25. Thus, on the average it seems that

the variation of the axial flow, which are driven by the velocity rms fluctuations, are satisfactory balanced by the values of the radial and azimuthal velocities on cross-planes. Therefore, on a statistical basis, this mechanism can predict the ones from the others and viceversa. This is particularly useful when due to set-up constraints, measurements on cross-planes are difficult to carry out. This principle will be recalled in the discussion of the fiber-laden jet in the next Chapter allowing the extension of the results on entrainment rate to the fiber-laden case.
Results show that the length scales on cross-planes are reduced when the Reynolds number increases. Therefore, a turbulent Reynolds number, in which those scales and rms fluctuating velocities are considered, is derived to be a function close to the Reynolds number based on the jet diameter and jet outlet velocity at the power 1/2.
The previous indications, together with measurement of turbulent kinetic energy and spectral behaviours, confirm that the dependence on Reynolds number of the single-phase axisymmetric jet statistics is high for values lower than 10000, whereas a sort of asymptotic behaviour is attained for larger Reynolds numbers.

The results presented in this Chapter are summarized in Capone et al. [2012].

3

Turbulent pipe jet laden with fibers

3.1 Introduction

As explained in Chapter 1, multiphase turbulent jets are very often encountered in several engineering applications and consequently a variety of studies have been developed to investigate their features. In addition to this, in many applications and phenomena, the dispersed phase is best approximated by ellipsoids or rod-like particles rather than spherical ones. In spite of this notion, there is a lack of studies on turbulent jet flows laden with such particles, with the exception of few numerical works (Lin et al. [2012]). In this Chapter we show the results of an experimental campaign on a turbulent pipe jet laden with fiber-like particles.

Optical experimental observation of turbulent two-phase flows requires a non-trivial image processing phase in order to discriminate the dispersed phase from the carrier flow seeded with particle tracers. Section 3.3 contains an overview of the approaches to this issue pointing out the advantages and drawbacks of the most common methodologies and presents a simple extension of the algorithm by Kiger and Pan [2000] which has been employed in this work. In Section 3.4 a validation of the proposed algorithm is given.
In the next Sections, results of simultaneous flow and particle velocity data are presented and discussed in detail and compared to single-phase results from the previous Chapter.

3.2 Experimental set-up

The experimental apparatus used for the measurement campaign is the same as the one employed for the single-phase case, depicted in Figure 2.1. The High-Speed PIV system is also the same as the one described in Section 2.3.
The dispersed phase is attained with nylon fibers (Polyamide 6.6, density 1.13-1.15g/cm^3, produced by Swissflock AG) with a mean length of approximately l=320μm and mean diameter 24μm, resulting in an aspect ratio $r_p = 13.3$. A sample microscopic image of fibers is shown in Figure 3.1 where measured diameter and length are highlighted. Fibers

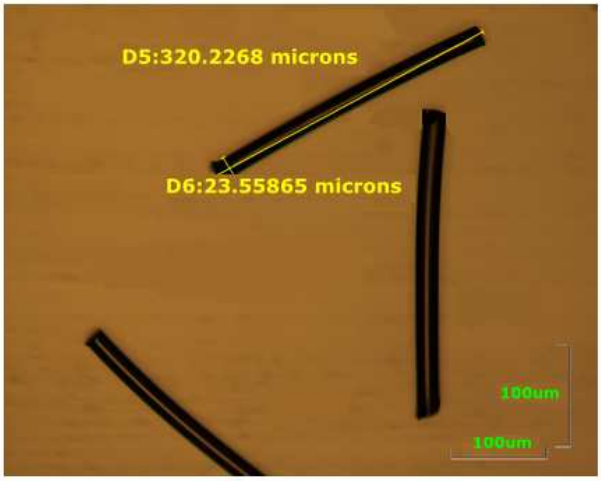

Figure 3.1: Fibers microscopic image. Diameter and length of a sample fiber is given (labelled in Figure as D6 and D5 respectively).

are introduced upstream in the system in the elevated tank where homogeneous mixing is achieved by stirring prior to injection in the pipe.
Acquisitions were carried out as shown in Section 2.3 for the single-phase case, with the limitation to the streamwise acquisitions. The jet Reynolds number based on the jet bulk velocity U_0 was 10000. In the previous Chapter this value was found to exhibit the features of an asymptotic behaviour in the measured quantities.

The importance of the concentration parameter in multiphase flows has been outlined in Section 1.1, where such flows have been categorized depending on flow-dispersed phase coupling which in turn is strictly linked to dispersed phase volume fraction, C_v.
Fibers suspensions feature peculiar characteristics which add complexity to this picture: at high concentration and in specific conditions they interact mechanically, entangling with each other and flocculating, i.e. creating fiber flocs which are detrimental for most engineering processes. Because of their peculiar behaviour, fiber suspensions are thus characterized via specific concentration paramaters. Since concentration has not proved to be a reliable measure of the tendency of a suspension to flocculate, Kerekes and Schell [1992] proposed a non-dimensional number indicating how relevant inter-fiber interactions are. The crowding number N, is a measure of the average number of fibers present in a reference volume represented by the sphere generated by a freely rotating fiber:

$$N = \frac{2}{3} C_v (r_p)^2 \tag{3.2.1}$$

Depending on the value of N, fiber suspensions may be classified into three regimes: dilute, semi-concentrated and concentrated.
An alternative way to characterize fiber suspensions, which will be used in this work, is

the nl^3 value, where n is the fiber number density which is equal to the number of fibers per unit volume. N and nl^3 are related by the following equation:

$$N = \frac{\pi}{6} nl^3 \tag{3.2.2}$$

and combining 3.2.1 and 3.2.2 we may obtain nl^3 from C_v:

$$nl^3 = C_v \frac{4}{\pi} r_p^2 \tag{3.2.3}$$

When $nl^3 \ll 1$, fiber-fiber interactions may be neglected and the suspension is called dilute. As the concentration increases the fiber distribution is controlled by hydrodynamic interactions between fibers ($nl^3 \gg 1$ and $nl^2 d \ll 1$) up to the regime where mechanical contacts between fibers are dominant ($nl^2 d \approx 1$).
The experimental campaign included two concentrations, namely $C_{v1} = 0.0018\%$ and $C_{v2} = 0.0054\%$. Suspension concentration was controlled measuring the amount of fibers to obtain a certain mass fraction in the flow and then converting it to volume fraction considering the water density at 25 degrees Celsius, i.e. $997.05 Kg/m^3$. It is straightforward to obtain that for both tested concentrations $nl^3 \ll 1$ holds, confirming that the fiber-suspension under investigation are very dilute. Two sample images of the single-phase and fiber-laden case are shown in Figure 3.2 for comparison.

3.3 Phase discrimination

Simultaneous velocity calculation of dispersed and carrier phase in turbulent flows requires a phase discrimination step to enable the application of PIV and Particle Tracking Velocimetry (PTV) respectively on the resulting seeding and dispersed phase images. Recent developments and the state of the art in the field of phase discrimination may be found in Cheng et al. [2010] and Khalitov and Longmire [2002] among others.
In general, phase discrimination methods may be divided in two broad categories depending on the stage when the actual discrimination is carried out: during image acquisition, i.e. optically, or after image acquisition, i.e. via post-processing.
In the first category fall the methodologies that typically make use of tracers containing a fluorescent dye (i.e., Rhodamine). The fluorescent dye absorbs the original laser light and emits light at a wavelength different from that of the laser, usually at longer ones. By using two cameras equipped with band filters, it is thus possible to separate the light scattered by the fluorescent tracers from that of the dispersed phase obtaining two distinct acquisitions for each phase.
This approach has been implemented in several works (Poelma et al. [2006], Towers et al. [1999] and Boedec and Simoens [2001] among others) with variations due to the use of two fluorescent dies for the flow tracers and the dispersed phase (Kosiwczuk et al. [2005] and Toth et al. [2009]) or two lasers with different wavelengths as in Driscoll et al. [2003]. Generally, the advantage of implementing methods based on optical separation lies in the reduced cross contamination occurring between carrier phase and dispersed phase data, also known as "cross-talk" (Poelma et al. [2006]). Nonetheless, a significant drawback is

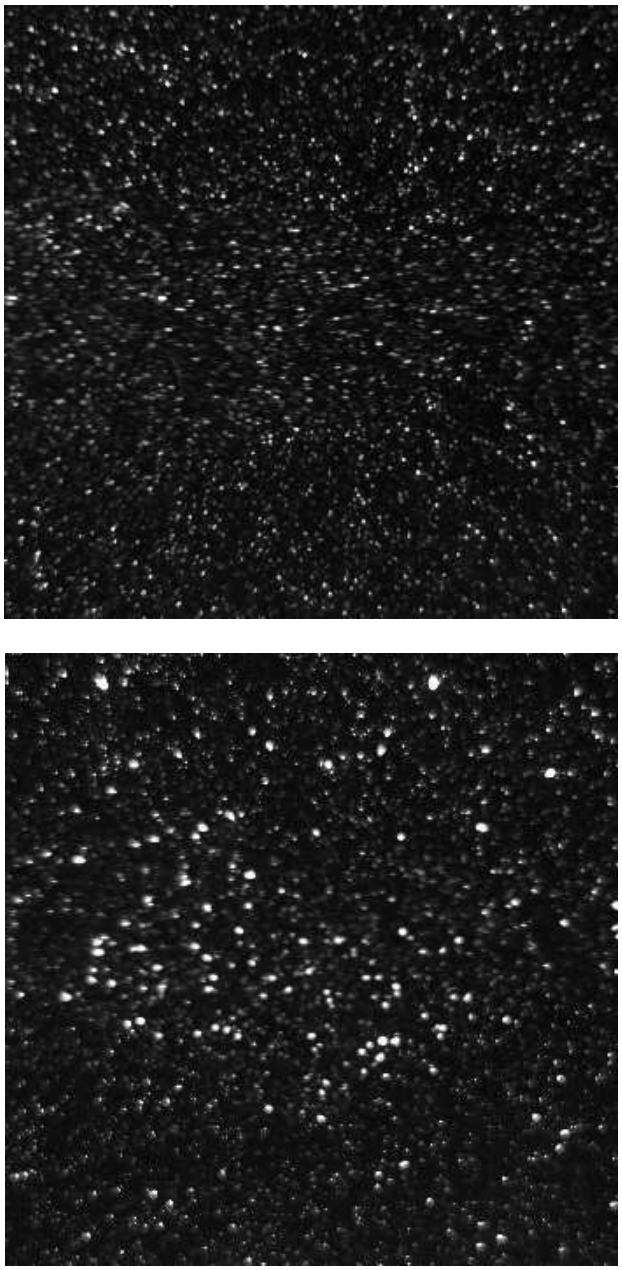

Figure 3.2: Fully single phase (top) and fiber-laden (bottom) sample image, $C = C_{v2}$.

the complicated and thus expensive set-up needed. This aspect is particularly relevant when more advanced acquisition schemes such as stereo-PIV are to be implemented.
On the other hand, post-processing methodologies are by definition simple and cheap to set-up as they rely on single camera acquisition schemes. When these acquisition schemes are adopted, a single camera collects images featuring both dispersed and carrier phases. A post-processing stage has then to be implemented to discriminate the phases images to be treated with PIV and PTV algorithms respectively for the continuous and discrete phase. The major drawback lies in the inherent errors introduced in this discrimination phase which should be assessed and quantified properly, usually through a validation step.
Several phase discrimination techniques have been proposed confirming the extreme difficulty at finding a general method independent of the experimental conditions.
In this work, a simple methodology for phase discrimination is proposed which builds on the work by Kiger and Pan [2000] and a validation by means of artificial images is provided in order to assess the error introduced in the calculated velocity fields. In the work by Kiger and Pan [2000], a two dimensional median filter is used to cancel out small tracer particles images present in two-phase raw pictures. Seeding-only images are then obtained subtracting from the original two-phase images the median-filtered images.
The filter is implemented by convolving a square two-dimensional filter stencil A, of width $N_f \times N_f$ pixels, over all the pixels within the image. The filter width, f, is taken to be the width of the window, N_f . For each position (i_o, j_o) of the window A, the filter sorts the gray level values of region A into ascending order and then selects the median value to replace pixel (i_o, j_o) (Kiger and Pan [2000]).
In Kiger and Pan [2000] a thorough discussion of the optimal size f of the square median filter is provided in terms of tracer and dispersed particles image size, respectively d_t and d_p, resulting in an optimal value of $f/d_t \geq 2$ for tracer particle evaluation and $f/d_t = 1.3$ (for $d_p/d_t \geq 3$) for dispersed phase evaluation.

In the current work, as a direct consequence of the choice to acquire images from a relatively large area of the jet, the spatial resolution is not sufficient to distinguish confidently the orientation state of fibers which consequently appear like near-circular areas as it is noticeable in Figure 3.2.

Fibers image size and shape is nonetheless dependent on their orientation state thus making discrimination from seeding tracers more difficult in particular when applying methods relying upon fixed criteria. In Figure 3.3 a median filter $f = 5$, so that $f/d_t \gg 2$ holds, is applied on a sample area of a two-phase case image at the highest fiber concentration. Although the filter application effect is to attenuate the tracers images they are not completely removed from the picture and are still visible as background disturbance. Due to the narrow gap between fibers and tracers size, a broader filter although eliminating more effectively the tracers would affect negatively the fiber images. To address this issue, in this work we add a further step after median filtering in which a threshold on pixel intensity is applied so as to identify whether a pixel belongs to a fiber-particle or not (that is tracers or background pixels).

The small difference between dispersed phase and tracer particles image size makes the application of discrimination methods based on fixed parameters difficult, causing

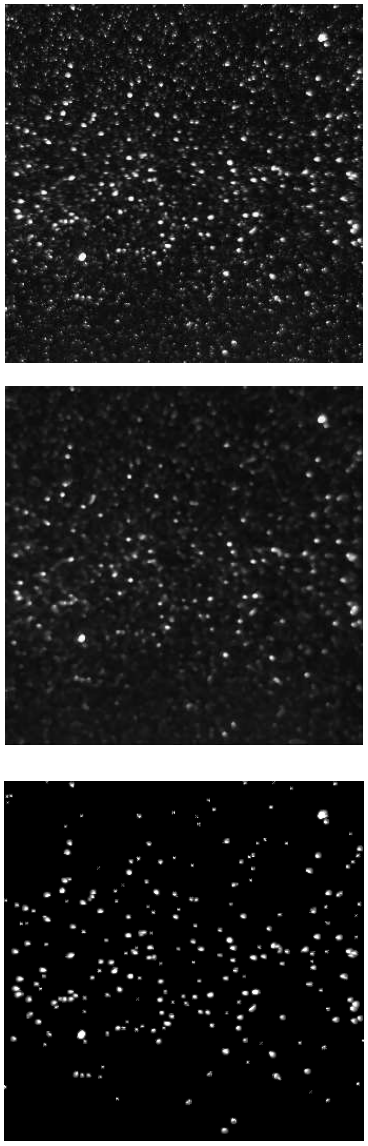

Figure 3.3: Sample area from a fiber-laden image, $C = C_{v2}$ case. Original image (top), image filtered with median filter $f = 5$ (center) and fiber-only image after threshold application (bottom).

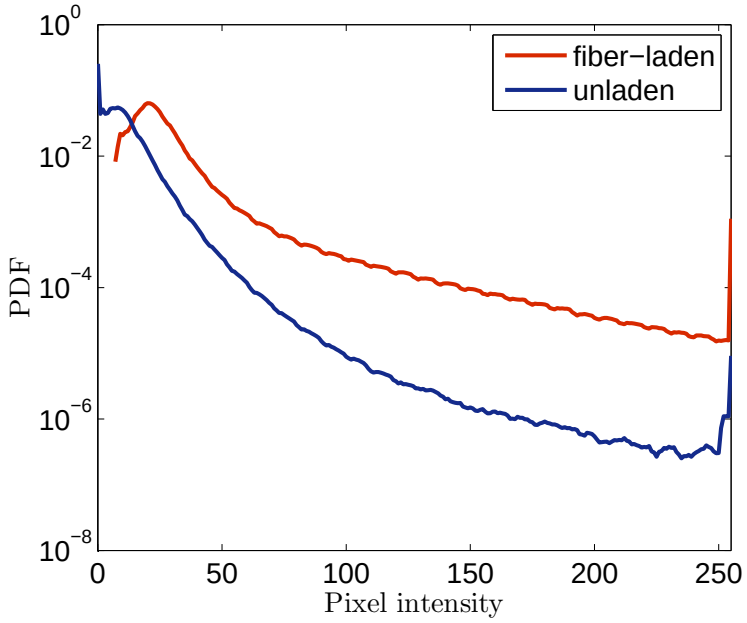

Figure 3.4: Pixel intensity PDF stemming from a median-filtered single-phase set of 200 images compared to median-filtered tracers and fiber-laden case.

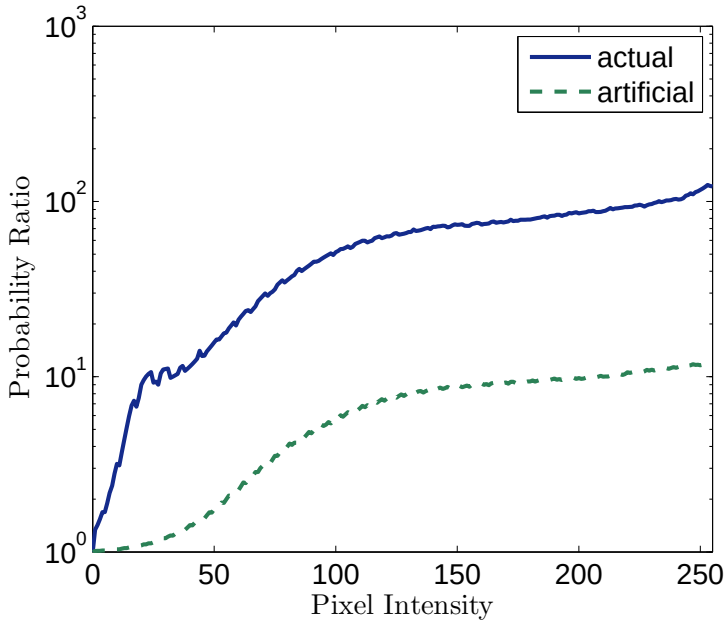

Figure 3.5: Probability ratio of a pixel featuring an intensity level higher than a certain value. Blue solid line obtained from Figure 3.4, green dashed line obtained from validation data.

uncertainty in image object evaluation. For these reasons the choice of the intensity threshold is based on the analysis of the statistical distribution of pixel intensity within images.
Probability density functions (PDF) of pixel intensity were calculated from a set of 200 uncorrelated images. PDF values proved to be fairly independent of time, as the PDF data converged on average for all pixel intensities within 10% of the final value yet after 100 samples. Figure 3.4 shows the PDF obtained for single phase and fiber laden case at the highest concentration C_{v2} after median filter application. The probability $P(i)$ that a given pixel features an intensity value higher than a given value i is thus given by integral of PDF curve from i until the upper range, i.e. 255.

Results show that when fibers are present in the flow, the resulting PDF is considerably affected, since larger particles feature higher intensity levels and, due to their size, are less affected by the median filter. To characterize the mutual relation of the PDF curves, for each intensity value i the probability $P_f(i)$ of a pixel having a higher intensity value than i has been calculated first in the fiber-laden case. The same has been carried out for the single-phase case $P_s(i)$ and the resulting probability ratio $P_f(i)/P_s(i)$ is given in Figure 3.5 where the blue solid line represents data obtained from the PDF shown in Figure 3.4 and the green dashed line is calculated from artificial data as explained in subsequent Section 3.4.

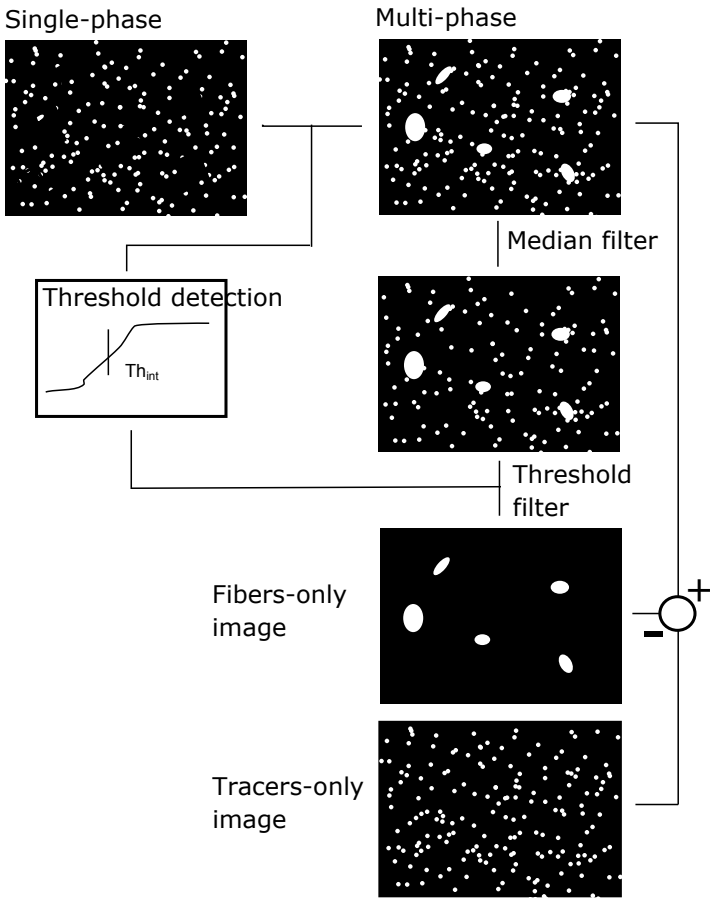

Figure 3.6: Schematic of the phase discrimination algorithm.

It may be noticed that as the intensity increases the ratio of the probabilities levels within the values 70 and 105. Information gathered from this profile may be used to set the threshold T_{int}, and this process is described in the next Section.
Once the value T_{int} is set, image pixels whose intensity exceeds the threshold T_{int} are labelled as pixels belonging to a fiber image. This criterion is applied on the whole initial image, obtaining finally a fiber-only image as shown at the bottom of Figure 3.3. This in turn can be subtracted from the original one to retrieve seeding-only pictures. The entire process is depicted schematically in Figure 3.6.

Clearly, the choice of a statistical threshold implies a certain degree of uncertainty and a trade-off in the results. High values of T_{int} would lead to fewer false positives, namely tracers pixels mistaken for fiber ones, whereas lower levels would lead to a higher rate of success at identifying fibers though at the same time taking in too many tracers.

In general, T_{int} should be chosen in order to minimize the error induced by the phase discrimination on both particle detection and PIV fields.
The analysis of the variation of the PIV/PTV results versus the choice of threshold T_{int} is the object of the next Section. The results obtained will provide a rationale for the threshold set-up in a general case.
As a final consideration, since the proposed method is based on a statistically evaluated threshold, the threshold calculation process needs to be repeated whenever the images features of the experiments undergo some changes, such as different boundary or inlet conditions or dispersed phase concentration.

3.4 Validation and Threshold setting

As explained in the previous Section, the proposed methodology requires the tuning of the value of T_{int} in order to minimize error in PIV and dispersed phase identification. Also, post-processing discrimination methods in PIV/PTV systems introduce a source of error in PIV calculations of carrier phase due to the empty areas left in the seeding image by fiber images removal (Khalitov and Longmire [2002] and Kiger and Pan [2000]) and in PTV results for erroneous identification of the dispersed particles (particles missed or false positives). To this end, in this Section we set out a validation procedure carried out on a set of a priori known data to assess the magnitude of these uncertainties and their sensitivity towards T_{int} variations. In order to perform the validation step, a further acquisition where the jet was laden with fibers at highest concentration C_{v2} and no tracers was carried out with the same experimental set-up.
Validation results will be compared to PDF findings in the previous Section in order to devise a general strategy for optimal T_{int} determination in similar experimental conditions.
The procedure follows the one detailed in Khalitov and Longmire [2002] and Kiger and Pan [2000] and consists of the following stages:
1) 160 experimental uncorrelated seeding-only image pairs are processed via the commercial PIV software described in Section 2.3. The mentioned fiber-only images are processed to derive the locations of fiber particles by means of a simple object detection strategy.
2) Artificial multiphase (tracers plus fibers) images are generated by combining the fiber-only pictures with the seeding-only images in step 1.
3) The phase discrimination algorithm detailed in the previous Section is applied to the resulting artificial images.
4) The tracer images obtained after phase discrimination are processed via PIV software. Simultaneously, the fiber-only images are processed to derive the locations of fiber particles.
5) The PIV velocity fields obtained in step 4 are compared to those calculated in step 1 in order to assess the error induced by the phase discrimination stage. Similarly, the locations of the identified fibers in step 4 were compared to the known ones in the original pictures in step 1. This procedure is repeated for several values of T_{int} and results

compared. Errors in PIV calculation (Kiger and Pan [2000]) take the following form

$$u_{err} = \frac{1}{NM} \sum_{i=1}^{N} \sum_{j=1}^{M} |u_{com(i,j)} - u_{ori(i,j)}| \tag{3.4.1}$$

$$v_{err} = \frac{1}{NM} \sum_{i=1}^{N} \sum_{j=1}^{M} |v_{com(i,j)} - v_{ori(i,j)}| \tag{3.4.2}$$

Where NM is equal to the number of velocity vectors of the carrier flow for each image, u_{ori}, v_{ori}, u_{com}, v_{com} are respectively the components of velocity along the x and y coordinate obtained from the original single phase acquisitions and the same components computed after the discrimination step. In order not to bias the results including velocity vectors lying in the fluid region outside the jet, we exclude in our analysis the vectors lying in positions where the mean velocity is lower than $0.005U_0$. According to this policy, roughly 2200 vectors were used for each of the 160 images leading to an overall vector number of 352000 for the carrier phase.
In Figure 3.7 u_{err} and v_{err} are plotted versus T_{int}. The results show that as T_{int} increases the displacement errors decrease reaching an optimal value in the range [60-90] whereas they steadily grow as T_{int} is incremented. This behaviour is simply explained considering that when T_{int} is low too many particles are removed from images resulting in several empty areas which decay the PIV effectiveness. The other way round, too high threshold values leave many fibers in the images. Figure 3.7 shows that with an optimal choice of T_{int} the displacement error can be reduced to nearly 0.02 pixels (compared to 0.015 pixels in Kiger and Pan [2000]) which corresponds to nearly 3% error with respect to mean displacement. This uncertainty is addressed specifically when PIV results are explained in the next Section. Similar results with respect to optimal T_{int} are obtained for dispersed phase identification as shown in Figure 3.8 where the rate of detection and of false detection are reported. Data show that with T_{int} lying within the range [60-90] the rate of detection of fibers is on average approximately 90% whereas the rate of false detection is nearly 0.05%.

We calculate now the probability ratio $P_f(i)/P_s(i)$ as described in the previous Section. Results are presented in Figure 3.5 in comparison with data obtained from actual multi-phase images and as such are labelled as "artificial". The qualitative trend of the ratio of the artificial images resembles the one recovered experimentally, in that after a climbing phase, the ratio reaches an asymptotic value. Most remarkably, the range of optimal T_{int} according to Figure 3.7 corresponds to the profile area just before the ratio stops to increase.
The results shown in this Section constitute a framework to lay out a threshold calibration procedure to be applied in a general case. According to this, the threshold calibration procedure will be based upon the following steps:
I) Probability ratio P_f/P_s is calculated from an independent set of experimental single and multi-phase data.
II) Threshold T_{int} is set in the interval [60%-75%] of P_f/P_s plateau level.
In order to translate this simple extension of the work by Kiger and Pan [2000] into a well-defined set of constraints a thourough validation scheme with different particle/tracers

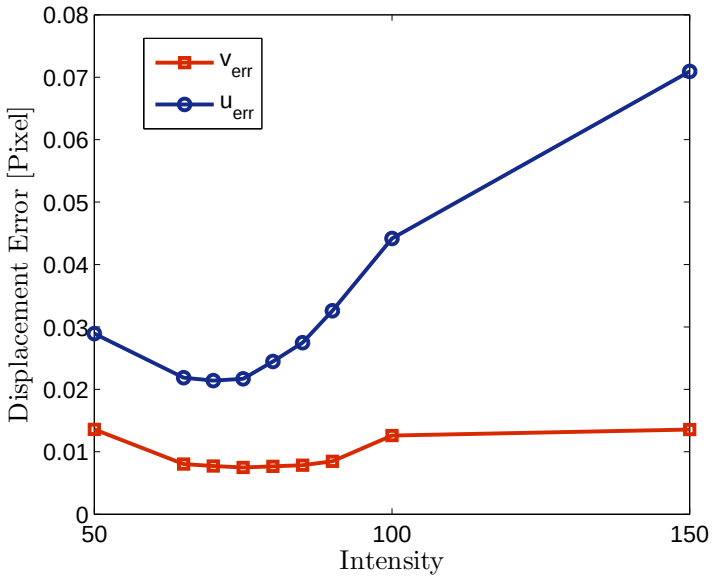

Figure 3.7: Longitudinal and vertical velocity displacement error induced by phase discrimination on PIV calculations versus intensity value of T_{int}. Data from artificial multiphase images.

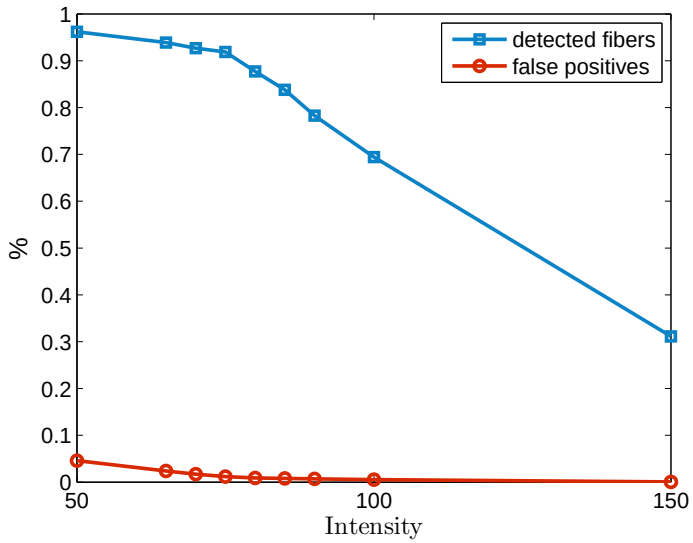

Figure 3.8: Percentage of detected fibers (blue squares) and uncorrectly detected fibers (red circles) versus intensity value of T_{int}. Data from artificial multiphase images.

image diameters is necessary. A broad criteria should rely upon the shape and the plateau level of the P_f/P_s curve, thus on the probability distribution of intensity in multi-phase images. Based on our tests in the presented experimental conditions, at least a value of $P_f/P_s = 60$ is necessary in the plateau region to obtain a satisfactory confidence in PIV/PTV results. It should be pointed out that a limitation of the presented algorithm resides in the necessity of acquiring single phase data for threshold calibration.

3.5 Results

In this Section, results of PIV/PTV calculations of, respectively, fluid and dispersed phase are presented. The commercial PIV package used for velocity vector calculations has been introduced in Section 2.3.
Minimum window size and overlap were respectively 32×32 and 75%, leading to a spacing between velocity vectors of 8 pixels corresponding to approximately $0.045D$.

3.5.1 Fluid phase in presence of fibers

As introduced in Chapter 1, Gore and Crowe [1989] proposed the ratio d/L to predict turbulence modulation in particle-laden flows. In the current study, the dispersed phase is represented by large aspect ratio rod-like particles and d was therefore set as the largest dimension, namely fiber length l.

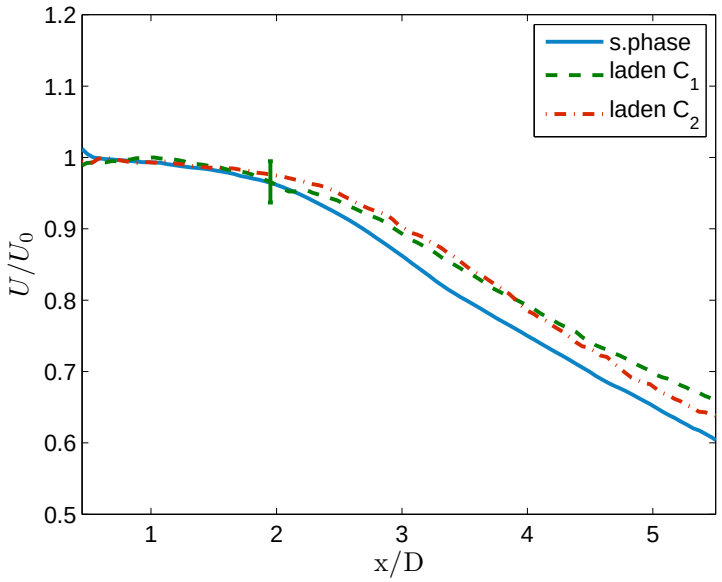

Figure 3.9: Streamwise profile of the centerline mean axial velocity for single-phase and fiber-laden case.

The flow integral scale L was calculated as the value at which the spatial correlation coefficient attains the value $1/e$, obtaining $L = 6mm$. It descends that, in the current work, $d/L < 0.1$. This value should, according to Gore and Crowe [1989] criterion, lead to turbulence attenuation. Mean axial velocity decay profiles are shown in Figure 3.9 for the single phase jet and fiber laden cases. The given profiles show that fibre injection in the flow, taking into account the discrimination estimate error, indicated by the vertical error bar, does not seem to influence noticeably the mean value. This is partially in agreement with results from Sadr and Klewicki [2005], obtained with a similar d/L ratio though with a quite different experimental set-up. Radial profiles of mean streamwise velocity shown in Figure 3.10 confirm this behaviour in the radial direction. In particular, for $x/D = 5$ and $y/D > 0.4$ the curves collapse.

The effect of the dispersed phase on turbulence intensity is summarised in Figure 3.11 where the RMS of streamwise velocity along the jet axis and at selected radial location is provided. A sample error bar in Figure 3.11 accounts for the measurement uncertainty added by the phase discrimination step. As set out in Section 3.4 this error has been quantified in a 3% additional uncertainty. Axial profiles show that the RMS levels are enhanced already at low fibers concentration with nearly 30% intensity increment for highest fiber concentration and $x/D \approx 4$. Apparently, the most remarkable enhancement takes place in the region from up to $x/D = 5$, i.e. approximately at the end of the jet core region. Radial profiles add to this perspective, showing how also in the radial direction, turbulence enhancement occurrs principally inside the core region. These results suggest

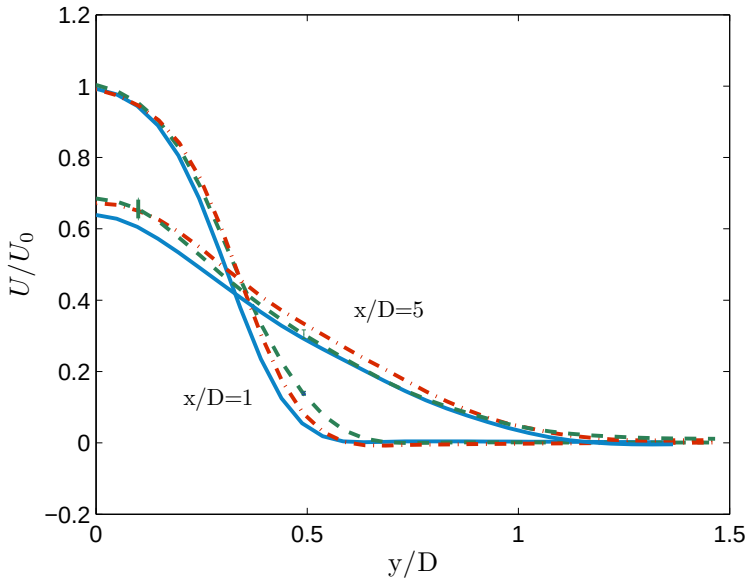

Figure 3.10: Radial profiles of the mean axial velocity of single-phase and fiber-laden case at two downstream positions $x/D = 1$ and $x/D = 5$

that the d/L ratio criteria cannot capture the complexity of the effects induced by non-spherical disperse particles. The observed behaviour in the core region of the jet may be intepreted by taking into account the dynamics of rod-like fibers in turbulent flows. The motion of a single rod-like rigid particle in a shear flow has been described by Jeffery [1922]: such particles spend most of the time almost parallel to streamlines revolving periodically around so-called Jeffery orbits.
Although the spatial resolution chosen for the measurements presented in this Chapter is not enough to observe fibers orientation, the results on turbulence modulation shown so far may be linked to the findings of Lin et al. [2012]. They investigated by means of numerical simulations a jet configuration laden with fibers finding that most fibers are aligned with the flow direction as they go downstream. At the same time, in the radial direction, fibers tend to align more with the flow direction in the region near the jet core (Lin et al. [2012]). This is partly in agreement with the results of the current work, where the turbulence enhancement in the axial direction decreases downstream of the pipe outlet, suggesting that fiber orientation plays a key role in turbulence modulation. When fibers are aligned with the main flow, the latter "sees" the fiber smaller dimension, whereas when the fiber is not aligned, wakes develop in the flow, increasing fluctuation intensity.
Turbulence intensity results may be discussed in the light of those obtained with the single-phase case in Chapter 2. Comparing data in Figure 3.11 to those depicted in Figure 2.7 it appears that the turbulence intensity of the streamwise component of velocity in the

axial direction in the fiber-laden case is comparable to single-phase jet for lower Reynolds numbers. As shown in Chapter 2, axial and radial turbulence intensities are strongly linked and this may suggest that the addition of fibers could lead to an enhancement of the entrainment rate, as shown in Figure 2.19 and 2.20.

3.5.2 Dispersed phase

Phase discrimination methodologies in multi-phase flows allow simultaneous calculation of fluid and dispersed phase velocities. In this Section, we present fiber and carrier-phase velocity results providing further insight on phase-interactions in this kind of experimental configuration.
To this aim, it is useful to evaluate the Stokes number associated to the given flow conditions. Its importance in the evaluation of particle dispersion in shear flows is discussed in Crowe et al. [1985] and has been explained in Chapter 1.
For rod-like particles, St is computed according to the formulation of Shapiro and Goldenberg [1993] based on the inverse of the resistance tensor S and the assumption of isotropic particle orientation, namely

$$\tau_p = \frac{2a^2 S}{9\nu} \frac{ln(r_p + \sqrt{{r_p}^2 - 1})}{\sqrt{{r_p}^2 - 1}} \tag{3.5.1}$$

where ν is the kinematic viscosity of the fluid and $r_p = b/a$ represents the fiber aspect ratio, being b and a respectively the fiber semi major and semi minor axes.

In this work the Stokes number, assuming the fluid characteristic time $\tau_f = \frac{D}{2U_0} \approx 8ms$, varied in the 0.6-0.7 range. Figure 3.12 reports the mean axial velocity, normalized with respect to fluid bulk velocity U_0, simultaneously measured for carrier and dispersed phase. The latter was obtained from sparsed, unstructured data generated in the PTV step by interpolating the vector data on a regular grid featuring 32 pixels vector spacing. Vector data interpolation was based on a second order polynomial fit calculated from the neighbors vectors.
Figure 3.12 reports simultaneous mean axial velocity of fluid and dispersed phase in a fiber-laden case with concentration C_{v2}, showing that fibers lag the fluid flow at the jet exit almost 12% reducing to nearly 5% at $x/D = 5$. Compared to results from Zoltani and Bicen [1990], where a jet laden with spherical particles with comparable Stokes number was investigated, the lag velocity observed in the fibers case is higher at the jet exit and the recovery velocity is also higher. In Figure 3.13 the lag velocity $(U_x - U_p)/U_0$, where U_p represents the streamwise mean particle velocity, is reported compared to Zoltani and Bicen [1990]. Starting from $x/D = 3$ the difference between the lag velocities increases dramatically with fibers recovering on average the fluid velocity faster than comparable spherical particles. This increased capability of fibers to follow the fluid motion as they move downstream may be explained again by fiber alignment to the flow which is found to increase in the axial direction (Lin et al. [2012]). As mentioned before, this behaviour causes the flow to "see" the fiber smallest dimension, leading to a lower resistance to slip between fiber and fluid which in turn tends to prolong the existing slip.

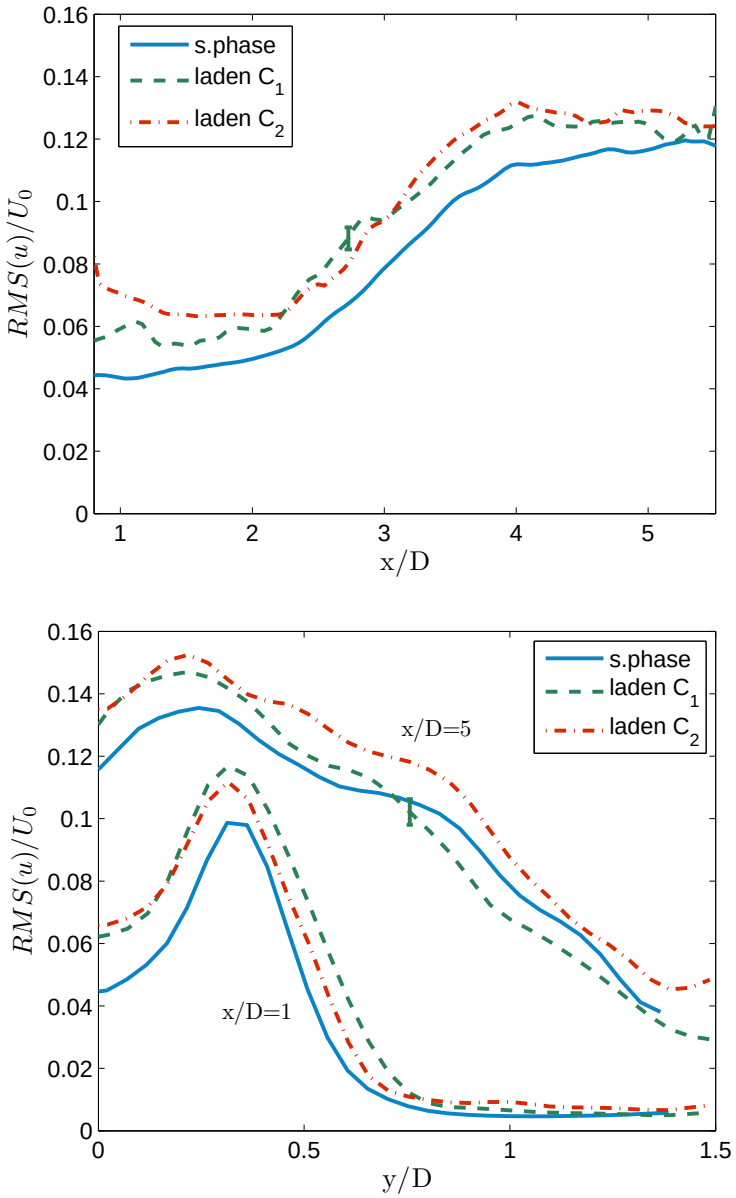

Figure 3.11: RMS of streamwise (at $y/D = 0$) and radial component of velocity in single-phase and fiber-laden case. Error bars represent the additional uncertainty induced by phase discrimination.

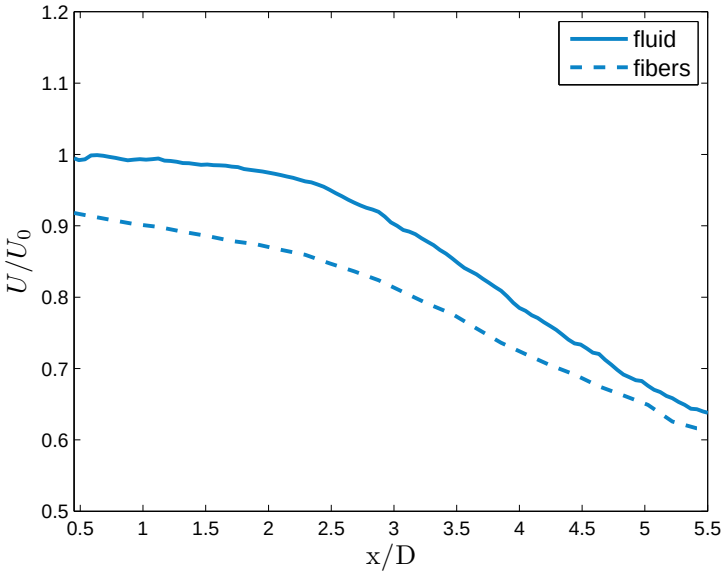

Figure 3.12: Mean axial velocity of fluid and fibers at $C = C_2$.

Figure 3.14 depicts respectively the streamwise and vertical components of velocity of the fluid and fiber phase in the radial direction. Data show that on average the dispersed phase follows quite faithfully the fluid velocity profiles when moving away from the jet axis and downstream of the pipe outlet. Remarkably, the vertical velocity profiles of the two phases almost match at every downstream position. This is in contrast with the results from Longmire and Eaton [1992] where particles radial velocity was negative (towards jet axis) near the jet outlet and positive for $x/D > 1$. This may be explained by the orientation state of the fibers which, most of the time almost parallel to the flow, limits their capability to move in the direction orthogonal to their length. Information on velocity fluctuations of both phases is provided in Figure 3.15 where RMS of streamwise velocity of both phases is presented. Intensity of dispersed phase fluctuations are 20% higher compared to fluid phase up to $x/D = 2.5$ where they collapse to fluid phase turbulence intensity levels. This results, matched to mean velocity findings shown in Figure 3.12, suggest an energy transfer occurring between fluid and dispersed phase along the jet axial direction. As the fluid exits the pipe, the energy content of the fiber phase stems mainly from fluctuating components whereas the fluid phase features higher mean levels. Downstream of the jet, the energy content of the fibers due to fluctuations in velocity approaches the same values of the fluid phase. This mechanism occurs supposedly via the orientation change of fibers and takes place in correspondence to the recovery of the mean velocity.

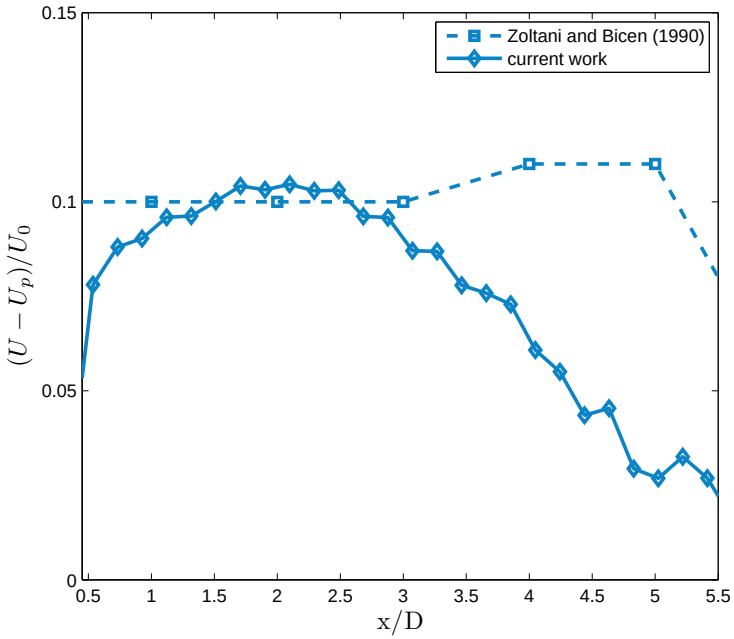

Figure 3.13: Fluid-particle mean axial velocity gap $(U_x - U_p)/U_0$ for $C = C_{v2}$ compared to Zoltani and Bicen [1990].

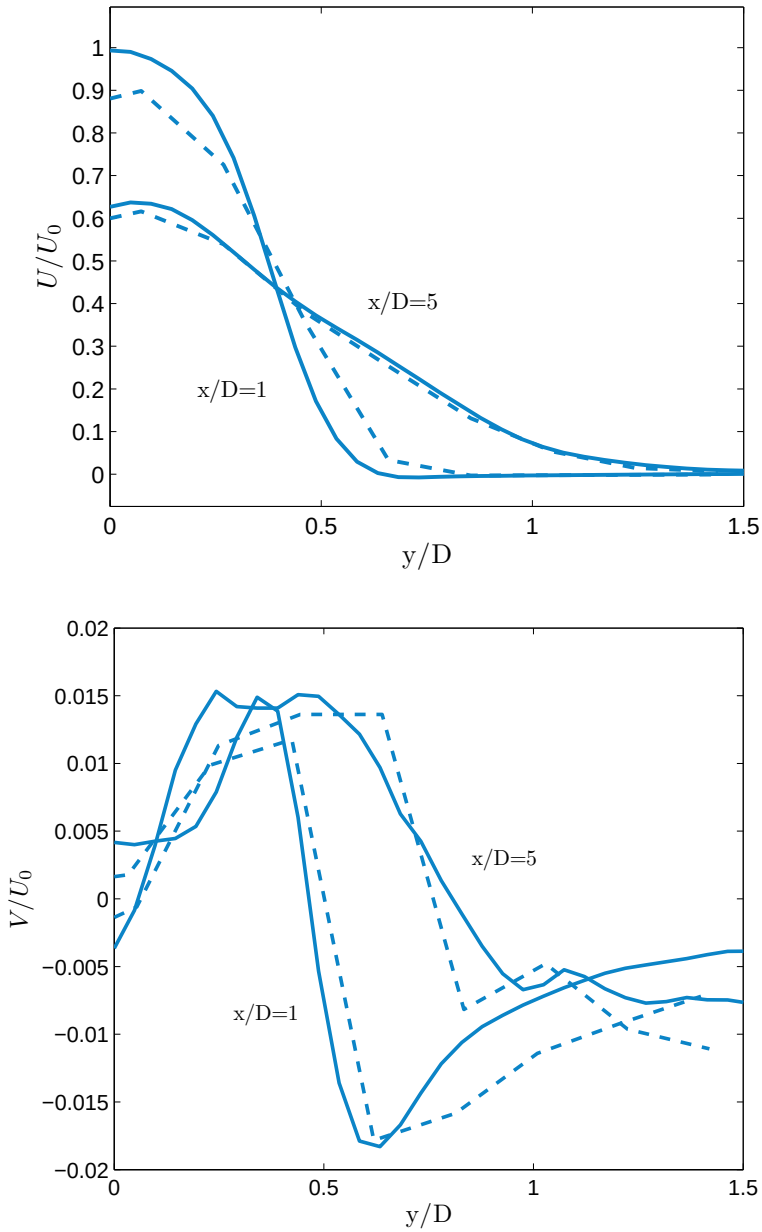

Figure 3.14: Fluid-particle velocity gap of streamwise (top) and vertical (bottom) components in the radial direction.

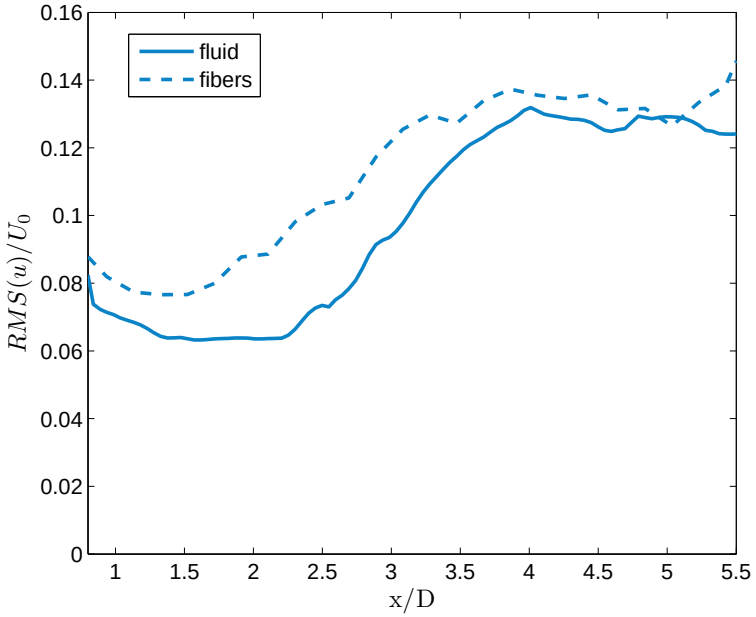

Figure 3.15: RMS of axial velocity of fluid and particles at $C = C_{v2}$.

3.6 Conclusions

In this Chapter an extension of phase discrimination algorithm by Kiger and Pan [2000] was presented based on intensity threshold in order to investigate a pipe turbulent jet laden with rod-like particles at two mass concentrations. Criteria for threshold determination and estimate of PIV calculations uncertainties were provided along with a discussion on method limitations. Results show that fiber injection does not affect jet mean profiles. However, even at low mass concentrations the addition of fibers lead to nearly 30% turbulence enhancement mainly in the jet core region opposite to the prediction by the single-parameter L/d criteria by Gore and Crowe [1989]. These findings confirm that such criterion cannot capture the complexity of interactions of such particles in turbulent flows. Turbulence modulation effects along the jet axis appeared to be linked to orientation state of fibers in the flow as reported in simulations (Lin et al. [2012]). Simultaneous calculations of PIV and PTV of respectively fluid and dispersed phase were presented showing that fibers tend to undergo higher lag velocity at the jet outlet than comparable spherical particles but with faster recovery speed. RMS data compared to results from Lin et al. [2012] suggest that an energy transfer between fluid and fiber phase occurs along the jet axis and that the driving mechanism is linked to fiber orientation in the flow.
Results for the fiber-laden case have been compared to single-phase case from Chapter 2, finding that the addition of fibers supposedly leads to an enhancing of the entrainment rate.
It is important to point out that due to the spatial resolution featured by the acquisitions, fibers particle appeared, in the collected images, as near-spherical particles. Nonetheless, the results shown hint at a relevant role played by the orientation state of fibers in the turbulence modulation effects, as set out in the previous sections.
These considerations pave the way for an ad-hoc acquisition campaign where the high spatial resolution allows simultaneous measurement of carrier flow velocity and fiber orientation data. This is the subject of the next Chapter.

4

Turbulent back-facing step channel flow laden with fibers

4.1 Introduction

As discussed earlier in Section 1.2, there exists a vast range of industrial applications where rod-like particles suspensions in turbulent flows are commonly encountered. Examples include pulp production, papermaking processes and several other industrial applications in which fibers are processed (es. fiber drying) or used as drag reducing agents (Paschkewitz et al. [2005]).
Controlling the rheological behavior and the concentration/orientation distribution of fibers is pivotal for process optimization. In papermaking processes (Lundell et al. [2011]), mechanical properties of manufactured paper are deeply influenced by anisotropic fiber orientation induced by the carrier flow. In fluid transport systems (see Paschkewitz et al. [2005] and Gillissen et al. [2008] among others), elongated fibers interacting with turbulent structures in the wall layer can be a valuable alternative to flexible polymers for reducing pressure drops.
Due to the practical importance of such suspensions, various experimental works have been developed testing various flow configurations (Carlsson et al. [2007] and Holm and Soederberg [2007] investigated shear flows along an inclined wall, Krochak et al. [2008] and Parsheh et al. [2005a] focused on flows through a linearly contracting channel and Parsheh et al. [2005b] on a planar contraction with different profiles). Similarly, many numerical works (see Zhang et al. [2001], Mortensen et al. [2008a], Mortensen et al. [2008b] and Marchioli et al. [2010]) have been carried out to study fiber dispersion in internal flows.
Experimental and numerical works have shown that fibers accumulate in the viscous sublayer and preferentially concentrate in regions of low-speed fluid velocity tending to align with the mean flow direction, in particular close to the wall. A step forward was taken by Krochak et al. [2009], who investigated by numerical simulations phase coupling in fiber suspensions flowing in a tapered channel and in Poiseuille flow (Krochak et al. [2010]).
Numerical works rely heavily on the broad assumptions required to model fiber motion

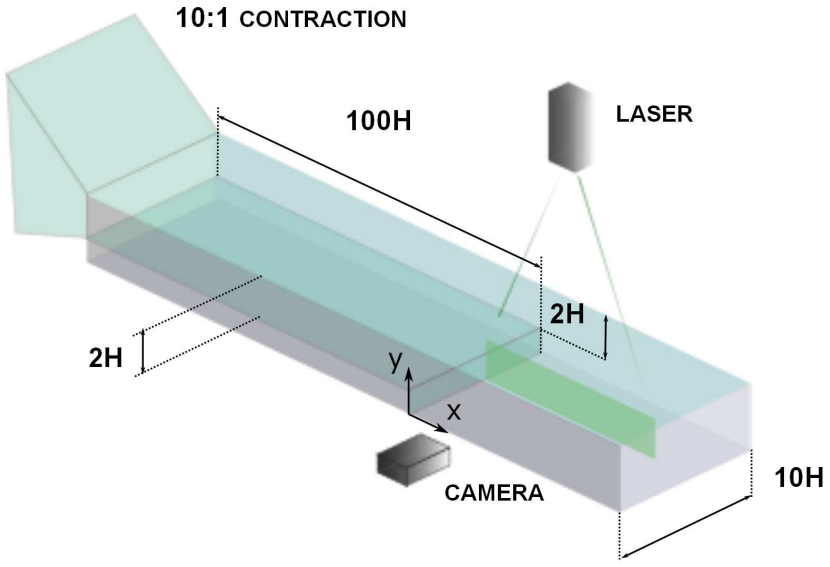

Figure 4.1: Experimental set-up for the channel and BFS flow.

in a computationally efficient and physically representative way. Validation of such assumptions demands a thorough characterization of the flow in terms of fiber orientation and distribution. More experimental data on such flows are needed to provide benchmark data for future modelling and approximate simulation methods (Marchioli et al. [2008]). Furthermore, despite some studies on sphere-laden flows in BFS channel configurations (Fessler and Eaton [1999] among others) more experimental data are needed to investigate the features of fiber-suspensions in such experimental conditions.
To this end, in this Chapter we show the results of a measurement campaign carried out on a fiber-laden flow through a channel with a BFS. The spatial resolution was specifically set in order to allow the detection of single fibers orientation. This feature not only is important for rehological properties of products in many industrial applications, but is linked supposedly to the turbulence modulation effects on the carrier phase, as suggested by the results provided in the previous Chapter.
Fibers identification and orientation detection requires a non-trivial image processing algorithm which shall be proposed in the next sections along with a validation on artificial images.

4.2 Experimental set-up

The channel and BFS apparatus is depicted in Figure 4.1. It consists of a channel $100H$ long, $10H$ wide and $2H$ high, where H represents the step height. The channel

is followed by a sudden expansion, with an expansion ratio $M/N = 1.5$, where M and N are respectively the channel height after and before the expansion. The channel is preceded by a smooth 10:1 contraction.
A standard PIV system is implemented via a Quantel $120mj$ Nd:Yag pulsed laser and PCO pixel-fly BW 14-bit 1392 $\times$1092 pixel resolution CCD cross-correlation camera. The repetition rate of the system is $15Hz$ and seeding and fiber particles are those described for the jet facility in Chapter 2.
The measurement campaign consisted of a preliminary acquisition in the channel section of the apparatus, precisely at $x = -10H$ and five acquisitions right after the expansion in order to cover an area up to $x = 8H$. Each acquisition covered an area of approximately 2H $\times$1.5H, leading to a resolution of roughly $0.01mm$ per pixel and consisted of 1000 images pairs. The Reynolds number based on streamwise maximum velocity U_0 and step height H was $Re_h = 18000$. The described acquisition scheme was employed for each one of the three cases tested; the baseline case, i.e. the unladen flow and the fiber-laden cases with two fiber concentrations, expressed as $nl^3 = 0.023$ and $nl^3 = 0.11$ corresponding respectively to $C_{v1} = 0.01\%$ and $C_{v2} = 0.049\%$. Thus, according to the classification set out in Section 3.2, the fiber suspension may be considered as dilute.

4.3 Image Processing and Phase Discrimination

Optical measurements have been extensively used to characterize fiber suspension flows. Parsheh et al. [2005a] used high speed imaging and LDV to study the orientation of fibers in a planar contraction. Metzger et al. [2007] developed a procedure to perform PIV calculations directly on fiber images for fibers sedimenting in a viscous fluid at low Reynolds number. Moses et al. [2001] used image processing to investigate fiber motion near solid boundaries in a simple shear flow. When the objective is the simultaneous measurement of the dispersed phase and the carrier fluid in dilute two-phase flow, more elaborated PIV approaches should be used. The simultaneous characterization of the continuous phase and the dispersed phase can be obtained following alternative approaches as described in Section 3.3. In this Chapter, we identify and validate a cheap, reliable image processing technique which is robust enough to discriminate between fibers and seeding in a fully developed turbulent flow in order to characterize the flow field and to calculate fiber concentration and orientation statistics. The methodology consists of image pre-treatment (intensity adjustment, threshold binarization and object identification by a recursive connection algorithm) and object-based phase-discrimination used to generate two independent snapshots from one single image, one for the dispersed-phase and one for the seeding. The performance of each image pre-treatment processing step is controlled by specific parameters, whose value is strongly sensitive to the test experimental set-up: the relative difference between tracer/fiber dimension determines the level of complexity of the phase discrimination step; the fiber aspect ratio determines the most reliable technique to identify fibers and to calculate their orientation. Furthermore, phase-discrimination requires non-trivial image-processing steps in order to discriminate the dispersed phase from the carrier flow seeded with particle tracers (see Kiger and Pan [1999] and Cheng et al. [2010]).

Different methods for fiber identification and subsequent orientation measurement have been implemented in various works. In Bernstein and Shapiro [1994] fibers detection and fiber orientation assessment was achieved through a visualization technique consisting of a short duration 3D video-photography system. Due to its relative semplicity, as discussed in Section 3.3, single camera set-up is the most employed: in the work by Parsheh et al. [2005a] the authors investigated the fiber orientation distribution function at the centerline of a planar contraction using an object fitting technique.
In Carlsson et al. [2007] authors investigated fiber orientation in a flow over an inclined plane using a 2nd order ridge detector with steerable filters (adapted from Jacob and Unser [2007]) for the calculation of fiber position and orientation in both streamwise and crosswise planes. Carlsson et al. [2011] build on these results, comparing the ridge detector to an elliptic filter using data from a fiber suspension in a laminar shear flow, finding that the two methods achieve approximately the same accuracy in spite of a lower computation time demanded by the ridge detector. With the same setup and methodology, Kvick et al. [2010] measured fiber position and orientation in relation to the low speed streaks present in a turbulent boundary layer.
The fiber identification and orientation calculation algorithm presented in this Chapter has been designed to suit our specific test environment in which (i) the (lower) size of the dispersed phase (fiber diameter) is similar to the size of the tracer and (ii) the fiber aspect ratio is not very large (order 10). When the fiber aspect ratio is small, edge detection as used by Rose et al. [2007] and Rose et al. [2009] becomes quite difficult to apply. The methodologies proposed by Metzger et al. [2007] and by Moses et al. [2001] to calculate fiber orientation become also difficult to apply. In Metzger et al. [2007] the typical fiber length was large (80 pixels); in Moses et al. [2001] the aspect ratio of fibers was also quite large ($40 \div 60$). In fact, fiber images size should be as big as possible in order to get good results when fiber orientation is measured based on the orientation of the line connecting the two ends of the fiber.
Since our object is to process a large number of images as required in a PIV-like context to derive joint statistics of flow field and dispersed phase (fiber) distribution and orientation, also the costs associated with image processing may become a major concern. Carlsson et al. [2007] used convolution of the fiber images with a steerable filter to detect fiber orientation. This algorithm is likely to be computationally more expensive than the algorithm (ellipse-fitting based) we propose in this work.
In the next sections a detailed description of each image processing step of the algorithm is given, with a focus on phase-discrimination and fiber orientation detection.

Figure 4.2 shows a sample snapshot of fiber and seeding particles taken from the channel apparatus. A close-up of the picture is shown on the right. The close up shows many of the features affecting image quality in the system under investigation. The simultaneous presence of seeding particles (appearing as white dots and indicated by the green arrows) and fibers (elongated white regions) is clearly noticeable. Sources of noise and image quality decay are introduced by the optical interactions (e.g. shadows) between fibers and particles. Fiber diameters have dimensions of the order of the seeding particles, hence fibers which are perpendicular to the laser sheet (as those indicated by yellow arrows) will not be distinguishable from seeding particles. Another issue is the presence of out of focus fibers and fibers lying in front of laser sheet which cause shadows

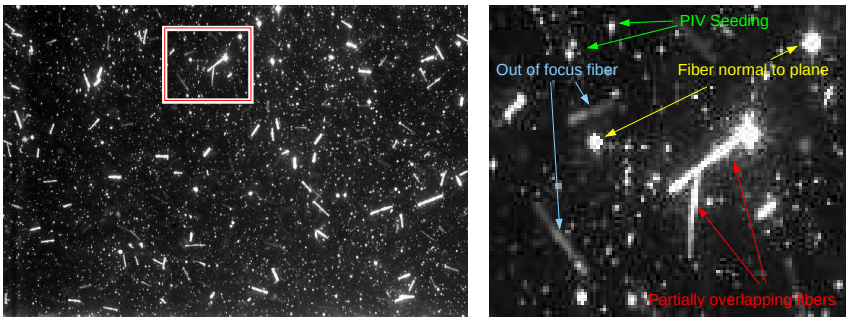

Figure 4.2: Sample raw image with tracer particles and fibers (left) and selected area (red square)

to appear (indicated by blue arrows). These regions are characterized by little or no seeding particles. The last issue is that of partially overlapping fibers, as those indicated by red arrows.
Image quality is undermined by all these different concurring effects and image processing is required to minimize these disturbances. The whole image processing algorithm is composed of four main steps, i.e. image pre-processing, phase discrimination, fiber analysis by object fitting and PIV analysis. A detailed description of the algorithm is described in the following sections.

4.3.1 Pre-processing

Raw images of laser illuminated fibers must be pre-processed to remove the background noise. In this thesis, this is made in two simple steps: first, the image intensity is adjusted such that 1% of the pixels is saturated at lowest and highest intensities of original image. Second, images are binarized: every pixel value above a prescribed intensity level is set to a maximum and every pixel below this value is set to zero. Once the image is binarized, phase discrimination can be carried out.

4.3.2 Phase-discrimination

The features of connected bright regions showing in each binarized image are evaluated using a recursive connectivity algorithm. Information about the size and the aspect ratio of each identified region, or object, is stored and can be employed to assess whether the object represents a tracer particle or a fiber.
In order to identify image objects representing fibers, we applied first an aspect ratio threshold discarding all the image objects featuring an aspect ratio lower than 1.5. Also, setting an aspect ratio threshold may be useful to eliminate both deformed, highly curved fibers and intersecting fibers from the identification process when this become a critical issue in the experiment.
Secondly, objects with a length exceeding a threshold value $l^* = 1/7l$ (see Table 4.1 for

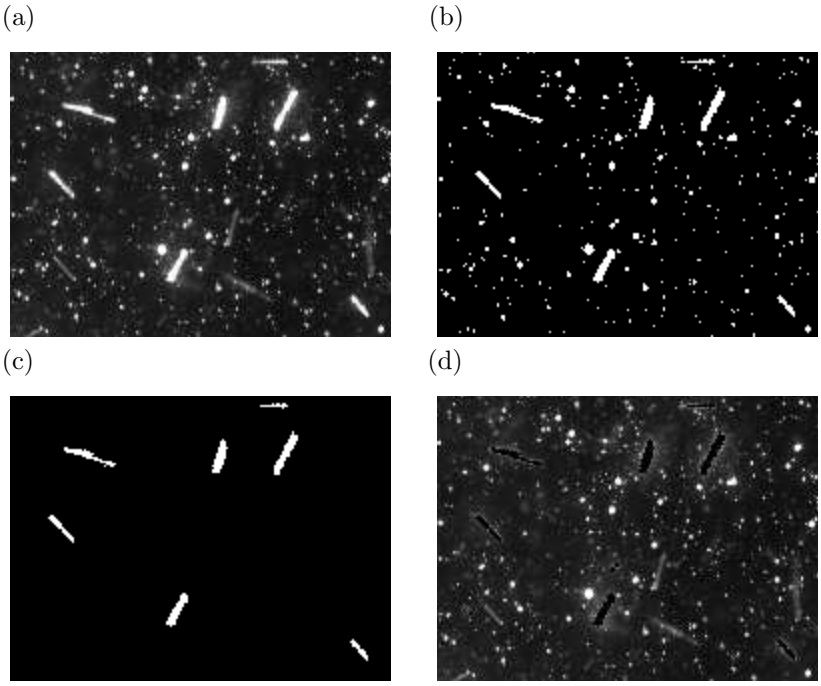

Figure 4.3: Steps of image processing algorithm: raw image (a), image after pre-processing (b), phase discriminated fibers (c) and seeding only images (d).

details) were considered as fibers. The criteria underlying the choice of the threshold value are discussed in detail in Section 4.4.3.

A set of pictures describing the pre-processing and phase discrimination steps are shown in Figure 4.3. Figure 4.3 (a) depicts a close-up of a where seeding particles and fibers are clearly visible. Figure 4.3 (b) is the output of the filtering and binarization step carried out on the raw image. As described, image is then fed to the recursive connectivity algorithm to identify the features of the image objects. Figure 4.3 (c) shows image objects which have been identified as fibers according to the mentioned criteria on aspect ratio and size. Finally Figure 4.3 (d) depicts the correspondent seeding-only image obtained subtracting from the original image the fiber-only image (c).

4.3.3 Fiber analysis by object fitting

Images in which fibers have been identified may then be further processed to obtain information about fiber orientation. To this end, image regions sorted as fibers are fitted to geometric ellipses following a non-linear least square approach as described in Fitzgibbon et al. [1999]. Ellipses were chosen because they reproduce quite reasonably the behavior of rigid elongated fibers in a number of applications of both scientific and engineering interest (Marchioli et al. [2010]).

Given a set of N points $(x_i, y_i),\ i = 1, 2, .., N$, with (x_i, y_i) representing the coordinates of the center of each pixel associated to the image object identified as a fiber, a fitting conic is described by a second order polynomial:

$$F(x, y) = a_{11}x^2 + a_{12}xy + a_{22}y^2 + 2a_{13}x + 2a_{23}y + a_{33} = 0 \tag{4.3.1}$$

The fitting conic is an ellipse if coefficients a_{ij} satisfy the specific constraint:

$$a_{12}^2 - a_{11}a_{22} < 0. \tag{4.3.2}$$

Values of $a_{ij}, i = 1, 3; j = 1, 3$ can be estimated using a general least-squares fitting approach which minimizes the sum of squared algebraic distances of the N points to the generic conic (see Fitzgibbon et al. [1999] for details).
Once the best fitting ellipse in terms of coefficients a_{ij} is computed, the orientation and all other relevant fiber statistics are calculated from the values of a_{ij}. For instance, rotation is calculated from coefficient a_{12}, which represents the tilt of an ellipse in the $x - y$ plane. Fiber orientation, θ_x, is defined as the angle formed by the best fitting ellipse major axis and the streamwise axis x. Using simple algebra, the coefficients a_{ij} can also be used to code the information about the fiber center of mass, aspect ratio and length as derived from the 2 D image.

4.4 Fibers Detection Algorithm Validation

Experimental two-phase simultaneous PIV investigations of fiber-laden turbulent flows are prone to various sources of error which should be adequately assessed and estimated. In particular, the fiber identification and orientation calculation process described in the previous section is subject to several limitations.
First of all distribution and orientation statistics are calculated only considering detected fibers. This means that fibers which are aligned or nearly aligned to the z axis and feature small orientation angles with respect to streamwise direction will be most likely not identified in the phase discrimination step and therefore will not be included in the calculations. In the limiting case, fibers perpendicular to the $x - y$ plane will look like a dot and thus invisible to the detection algorithm. Secondly, fibers that are only partially illuminated by the laser sheet could be misinterpreted as seeding or impurities. Finally special attention should be paid to the intrinsic approximation of using two-dimensional image information which are indeed the projection of three-dimensional orientation data. In this and similar works, where images are collected with a single camera, fiber orientation data is in fact worked out from projections of three-dimensional fibers onto the bi-dimensional image plane and the effect of such process should be carefully accounted for.
With reference to PIV velocity fields calculation, it is necessary to assess the error introduced by the "holes" left by fibers images removal, as shown in Figure 4.3. Monte Carlo simulations were adopted in this work to quantify the error magnitude affecting fibers number density and orientation distribution results. These simulations provide pseudo-experiment information on fiber distribution and orientation within the laser sheet. Arti-

ficial images which contain a certain number of seeding particles and randomly-oriented fibers are generated automatically and subsequently fed to the phase detection and fiber orientation modules. Statistical reliability is ensured by the large amount of data employed over the process whereas the way artificial images are generated is aimed at simulating the sources of uncertainty previously detailed. Two main test cases have been set up to validate the algorithm, each one characterized by specific image features as described below:

1. Artificial images displaying 50 or 150 fibers featuring no spanwise orientation (all fibers lying entirely within planes parallel to $x - y$ plane)

2. Artificial images displaying 150 fibers featuring spanwise orientation

In all test cases fiber aspect ratio in the artificial images has been set to 20. Each test case has been run several times gradually increasing the number of images, and consequently the number of fibers, to assess the effect of fiber sample size on the accuracy of the calculated statistics. Finally, the effect of the length threshold on the accuracy of the fiber identification step has been quantified.

4.4.1 Artificial images generation

Artificial images have been generated to account for the several sources of uncertainty which exist in actual experimental conditions. First of all, the light source is provided by a laser sheet having a finite thickness which implies that fibers could possibly be only partially lit thus leading to inaccuracy in the detection phase. The light intensity is also not uniform along the laser sheet thickness, resulting in non-homogeneously illuminated fibers. Images have been thus obtained generating first an artificial volume in which fully three-dimensional fibers and seeding particles have been randomly generated and subsequently taking into account just a thin slice of the volume. The objects, i.e. fibers and seeding particles, contained within the obtained sub-volume are then projected onto a plane. This method makes it possible to mimic the laser sheet thickness effect on algorithm accuracy along with the effect of estimating object orientation in a three-dimensional space from two-dimensional data. Fibers objects have been simulated by ellipsoids with same fixed dimensions and have been placed randomly in the artificial volume applying to them a random three-dimensional rotation matrix; seeding particles were considered as spherical objects distributed randomly inside the artificial volume. Light intensity distribution of tracer particles is calculated based on the relation described in Raffel et al. [2002] which has been extended to ellipsoid-like objects. For the generic fiber depicted in Figure 4.4, light intensity along fiber minor axis in the region included between the two focal points of coordinates (x_{f1}, y_{f1}) and (x_{f2}, y_{f2}) is assumed to be constant. In the same region the intensity along fiber major axis is instead assumed to follow a Gaussian profile, described as

$$I(x') = I_0 exp\left[\frac{-(x' - x_0)^2}{\frac{1}{8}d_\tau^2}\right] \tag{4.4.1}$$

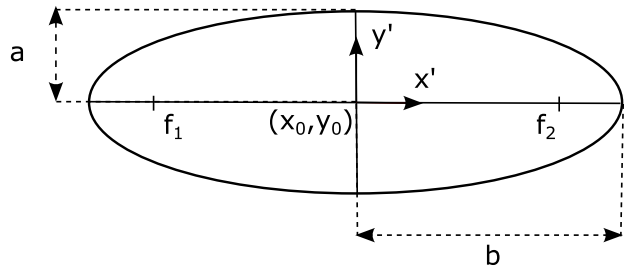

Figure 4.4: Single fiber model for light intensity calculation. Focal points are labelled f_1 and f_2.

where (x_0,y_0), d_τ and I_0 represent respectively the coordinates of ellipsoid center, the particle image diameter which accounts for diffraction limited and geometric spot size (Raffel et al. [2002]) and the laser sheet peak intensity. At the ellipsoid's ends, in the region where $x_{f1} \geq x \geq x_{f2}$ holds, light intensity is considered to be dependent on both coordinates leading to the following relation

$$I(x', y') = I_0 exp\left[\frac{-(x' - x_{fi})^2 - (y' - y_{fi})^2}{\frac{1}{8}d_\tau^2}\right] \tag{4.4.2}$$

where (x_{fi}, y_{fi}) is the generic focal point coordinate. The value d_τ is determined considering the following relations

$$d_\tau = \sqrt{M^2 d_p^2 + d_s^2} \tag{4.4.3}$$

$$d_s = 2.44(1 + M)f\lambda \tag{4.4.4}$$

where $d_p = 2b$ represents the physical particle size, M the lens magnification, approximately 0.4 in this work (Raffel et al. [2002]), d_s is the diffraction limited spot size and $f = 1.4$ and $\lambda = 524\ nm$ are optical system parameters. Peak intensity of the laser sheet I_0 is non-constant within the laser sheet, resulting in inhomogeneous lighting of fibers lying within the sheet. The peak intensity depends on the actual position of fiber within the sheet, leading to the following expression for I_0

$$I_0(z) = q \exp\left[\frac{z^2}{\frac{1}{8}\Delta z_0^2}\right] \tag{4.4.5}$$

where z-axis origin is considered to be at the center of the laser sheet where light intensity is maximum, Δz_0 is the laser sheet thickness and q is the efficiency with which the particle scatters light. In Figure 4.5 a sample artificial fiber image (right) is compared to an actual one (left).

Figure 4.5: Sample actual (left) and artificial (right) single fiber images.

4.4.2 Accuracy of ellipse fitting statistics

Test Case 1
This case represents the baseline test with fibers orientations defined in $x-y$ plane only. Fibers are located randomly inside the three dimensional volume and oriented randomly in the $x-y$ plane. Two runs of this test case have been performed: the first is characterized by each artificial image displaying 50 fibers; in the second run, fiber number per image has been increased to 150. In the first case, a very dilute suspension could be simulated, in which no fiber image intersection would occur. By increasing the concentration to 150 fibers a dilute suspension could still be simulated where fiber images intersection would occur, then resembling actual experimental conditions for fiber suspensions in turbulent flow.

Figure 4.6 shows a close-up of a sample image from the 50 fibers per image case, in which fibers detected with the presented methodology are depicted along with their center of mass. To validate extensively the proposed algorithm, statistics of fiber number density and fiber direction cosine have been computed and compared to expected values. The normalized number density is defined binning (i.e. counting) identified fibers inside regions of constant volume. When a dependence from one spatial coordinate is expected (e.g. the wall normal direction y in a boundary layer flow) volumes are arranged to span different value of the y coordinate. Dividing the number of fibers in each bin by the overall number of fibers in the image (about 60 fibers per square centimeter), the normalized number density obtained represents a probability density function and its integral equals to 1. Values of fiber number density calculated for artificial images were quite good, with approximately 99.9% of generated fibers correctly identified and located. The normalized average fiber number density, calculated binning the fibers into 17 discrete slabs arranged in the y direction was 0.0588 ± 0.0005.
Statistics on fiber orientation are obtained in terms of average value of direction cosine, $\mid \cos(\theta_x) \mid$. The average value can be calculated considering the whole volume. Nevertheless, when the objective is to define a spatial profile for fiber orientation, the average value can be calculated considering sub regions specifically defined to span different values of the relevant coordinate (e.g. y). Dividing the region of interest in I identical bands along the y direction, the orientation cosines of all the fibers whose centroid lies within the i_{th} band are summed over and then divided by the overall number of fibers.

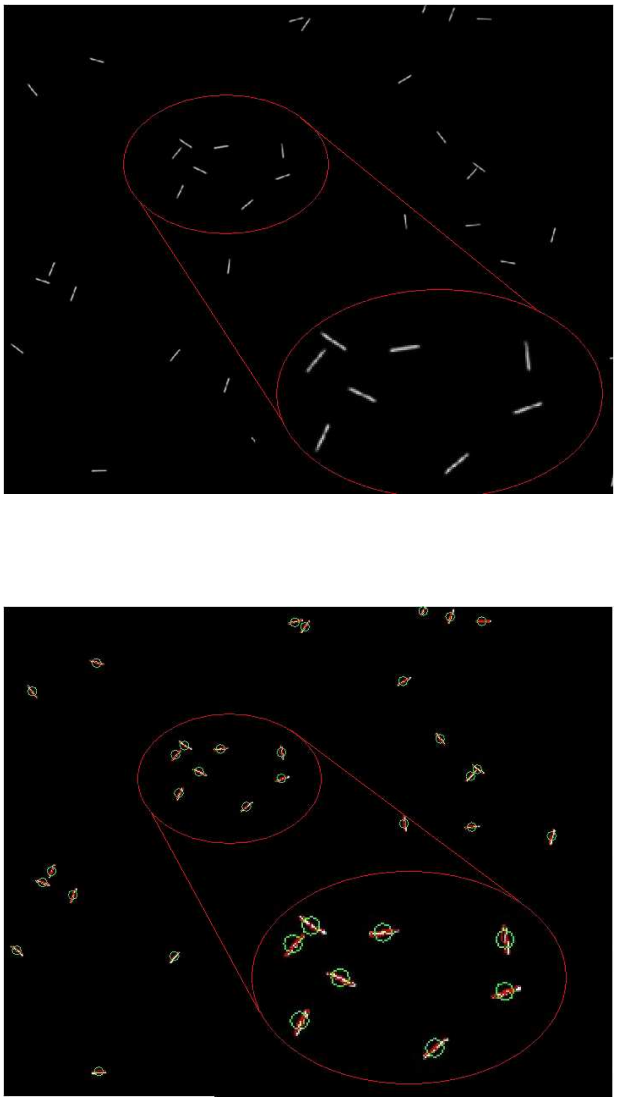

Figure 4.6: Close-up of artificial image with 50 fibers (top) and detected fibers (bottom). Red contours and green circles show respectively the best fitting ellipse and center of mass.

The mean direction cosine at every i_{th} band expressed in y position is thus calculated as

$$<\mid \cos(\theta_x) \mid>_i = \frac{1}{N_{p,i}} \sum_{k=1}^{N_{p,i}} \mid \cos(\theta_x) \mid_k \tag{4.4.6}$$

where $N_{p,i}$ represents the number of fibers identified within the i_{th} band. Values of $\mid \cos(\theta_x) \mid \simeq 1$ denotes a strong mean alignment of fibers to the streamwise direction.
The expected mean direction cosine calculated from artificial images was $2/\pi \approx 0.64$ which is the mean orientation angle projected on a unit sphere for randomly rotated fibers. The mean direction cosine calculated from ellipse fitting of 250 artificial images containing 50 fibers each was 0.64 ± 0.02 (mean $\pm$ standard deviation).
For the test case 1, in which 50 fibers per image were generated, the relative error in $\mid \cos(\theta_x) \mid$ is less than 1% if the number of processed fibers is $O(10^4)$, i.e. the number of processed images is large enough to be statistically representative of average fiber orientation.
The second run of the test case, in which 150 fibers were generated per image, made it possible to simulate a more practical flow condition, in which fiber intersection occurs within images, adding a further source of uncertainty in fiber discrimination and orientation calculation due to overlapping fibers. The relative error of calculated mean direction cosine with respect to expected value $2/\pi$ is reported in Figure 4.7 versus the number of fibers over which statistics are calculated (i.e. fiber sample size). Validation results confirmed the algorithm accuracy and robustness: a mean direction cosine relative error of 1% was achieved already after processing 12500 fibers, corresponding to nearly 85 images.

Test Case 2
In this test case fibers were generated with a random orientation in the three dimensional volume, i.e. without forcing them to lie parallel to the $x-y$ plane. This test case gives information on algorithm robustness towards orientation estimate errors due to fibers featuring weak orientation in the $x-y$ plane as opposed to strong orientation in $x-z$ plane. Artificial images were generated containing 150 fibers each; different runs with increasing number of images were tested to assess the dependency of algorithm accuracy on overall number of fibers sampled. Validation gave satisfactory results, with number density data in good agreement with the expected uniform value. For fibers randomly oriented in the three dimensional space, expected mean direction cosine should be equal to 0.5. Nevertheless, since statistics are calculated for (the portion of) fibers which are partially illuminated by the laser sheet, calculated mean direction cosine is typically larger than 0.5 because fibers which are strongly orientated out of the image $x-y$ plane are difficult to detect and, in the limiting case, appear as dots and are not even discriminated as fiber. Even in this case, convergence in accuracy is achieved quite fast: $|\cos(\theta_x)|$ relative error calculated for a fiber sample size equal to 1500 is as much as 5%; it drops to below 1% as the total number of fibers reaches 45000. Figure 4.7 shows results of Test Case 2 in comparison to Test Case 1.

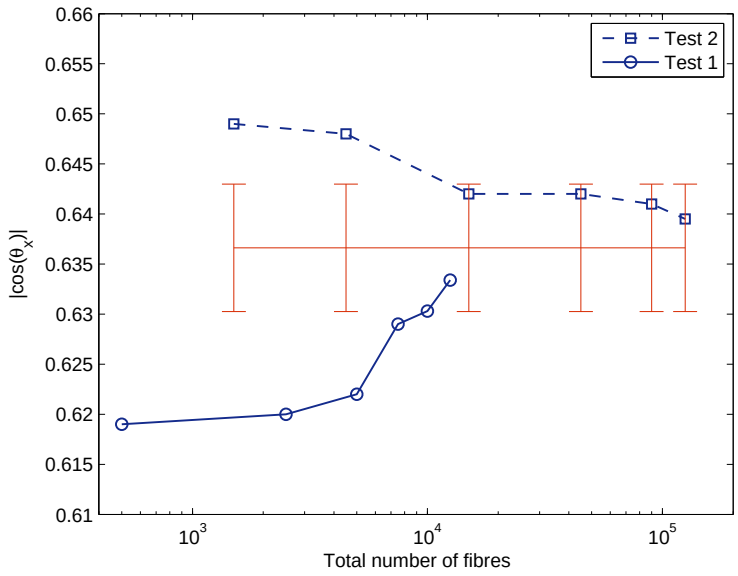

Figure 4.7: Mean direction cosine versus number of fibers sampled. Test Case 1 and Test Case 2 compared to expected $2/\pi$ value, red line with 1% error bar.

4.4.3 Effect of threshold setting

Two parameters are used to identify fibers within the phase discrimination step, i.e. image object's aspect ratio and length. Accurately setting the threshold for the latter can result in significant improvement of algorithm accuracy in terms of $|\cos(\theta_x)|$ relative error. Proper threshold setting involves a certain degree of compromise. More conservative choices, such as deeming as fibers only image objects having a length equal to actual fiber length l, could lead to too many overseen fibers; on the other hand, too loose a threshold would eventually lead to many false positives.
In Table 4.1 the comparison of results obtained considering four different length thresholds, l^*, is given. Artificial images used for validation purpose were those from Test case 2 (300 images with 150 fibers each). As may be noticed, a strict constraint on image object length compared to actual fiber length, l, ($l^* \simeq l$) leads to almost 10% error in $|\cos(\theta_x)|$ calculation. Error decreases steadily when threshold length is set to $l^* = 1/3\ l$ of actual fiber length as reported in Parsa et al. [2011] and reaches an optimum with $l^* = 1/7\ l$. Lowering the threshold below $l^* = 1/7\ l$ leads to an increment in error and an overall decay of algorithm accuracy.

Threshold length	$\lvert\cos(\theta_x)\rvert$	Relative error on $\lvert\cos(\theta_x)\rvert$
$l^* > 1/9\ l$	0.61	4.4%
$l^* > 1/7\ l$	0.64	0.5%
$l^* > 1/3\ l$	0.66	3.5%
$l^* > 2/3\ l$	0.677	5.96%
$l^* \approx l$	0.698	8.8%

Table 4.1: Effect of threshold length, l^*, on mean direction cosine relative error. Test Case 2, error calculated over 45000 fibers.

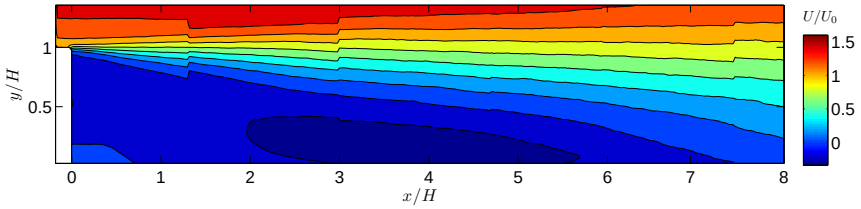

Figure 4.8: Contour plot of mean streamwise velocity data of unladen case.

4.4.4 Effect of phase discrimination on PIV results

Experimental data collected with the channel and BFS facility were used to assess the accuracy of PIV velocity field calculated from tracer images obtained from the processing of pipe images. As explained before, post-processing phase discrimination schemes introduces uncertainties in PIV calculations, due to the presence of "holes" left by the dispersed phase, in this case fiber particles, removal. Following the same procedure described in Section 3.4 algorithm validation was performed as described in Kiger and Pan [2000] comparing the PIV results from tracer only images to those stemming from the same images to which fibers were artificially added. For convenience we repeat below the steps comprising the validation procedure.
PIV velocity fields were first calculated from 70 pairs of tracer only images. Composite images displaying seeding and fibers were then generated combining seeding only images to fibers only images. The discrimination algorithm was applied to the latter images obtaining seeding only images. PIV calculations were performed on such images and results statistically compared to those collected in the first step. The total error of 1.10% of the average displacement over the whole field of observation was of the same order of magnitude of that reported in Kiger and Pan [2000].

4.5 Results

In this Section, results from single-phase and multi-phase flow data are presented and discussed. In the latter case simultaneous carrier flow PIV calculations and dispersed

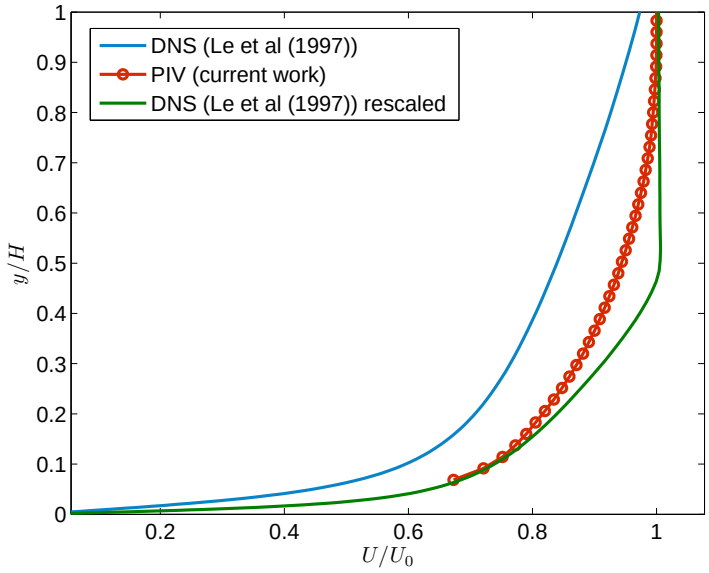

Figure 4.9: Mean streamwise velocity at $x = -10H$, compared to Le et al. [1997] data at $x = -3H$.

fibers data are obtained with the phase discrimination algorithm presented. PIV calculations are carried out from seeding-only images obtained from multi-phase data according to the process shown in Section 4.4 and the limitations described. PIV computations are performed by means of the commercial software detailed in sections 3.2 and 4.2. Minimum window size was set to 32 ×32 pixels with 50% overlap, leading to a vector grid spacing of $0.016H$.

4.5.1 Unladen flow

Results from the unladen case are here presented and compared to literature data from Le et al. [1997] at $Re_h = 5100$ and expansion ratio 1.2. Figure 4.8 shows the mean streamwise velocity of the whole field. In Figure 4.9 the mean streamwise velocity at $x = -10H$ is depicted and compared to Direct Numerical Simulation (DNS) data from Le et al. [1997] obtained at $x = -3H$. Although the profiles do not match, due to the different boundary conditions (in Le et al. [1997] the simulated flow is unconfined at the top of the channel) when they are normalized with respect to the channel halfwidth ($2.5H$ in Le et al. [1997]), the agreement is fair. The rescaling is shown in Figure 4.9 as the green profile. These results are similar to those obtained by Piirto et al. [2003] in similar experimental conditions. In Figure 4.10 RMS data of streamwise velocity are compared to DNS data. As suggested by Piirto et al. [2003], data are normalized with respect to maximum RMS value and show a satisfying qualitative agreement.

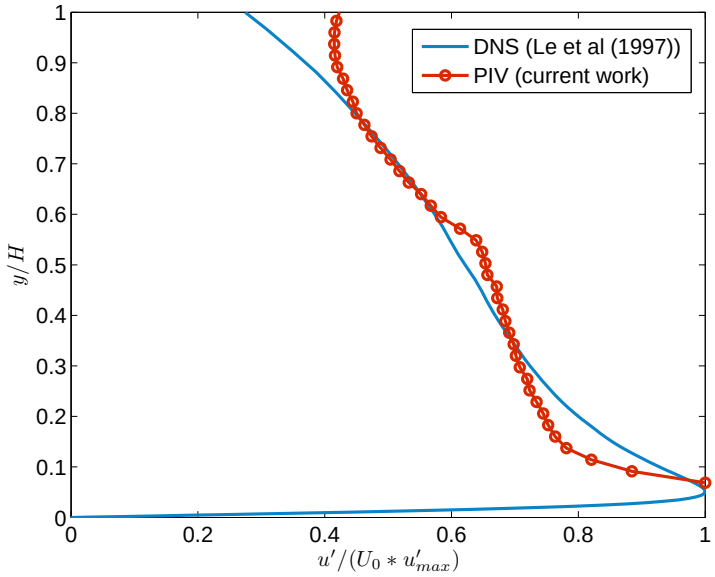

Figure 4.10: RMS of streamwise velocity at $x = -10H$, compared to Le et al. [1997] data at $x = -3H$.

PIV data close to the wall were discarded due to low reliability and thus the closest point to the wall where velocity data are available is located at nearly $0.7mm$ from the wall. Consequently the friction velocity

$$u_\tau = \sqrt{\frac{\tau_w}{\rho}} \tag{4.5.1}$$

where

$$\tau_w = \mu \left(\frac{\partial u}{\partial y} \right)_{y=0} \tag{4.5.2}$$

is the wall shear stress and μ the dynamic viscosity of the fluid, is calculated fitting the velocity profile to the Spalding universal profile for boundary layers (Spalding [1961]). The curves fitting is shown in Figure 4.11 resulting in a friction velocity estimate of $u_\tau \approx 0.082m/s$.
Mean and RMS profiles of the streamwise velocity at different positions downstream of the step, namely $x = 2H$ and $x = 4H$, are depicted in Figure 4.12 showing again a good agreement to numerical data, despite the difference in Re_h and expansion ratio.

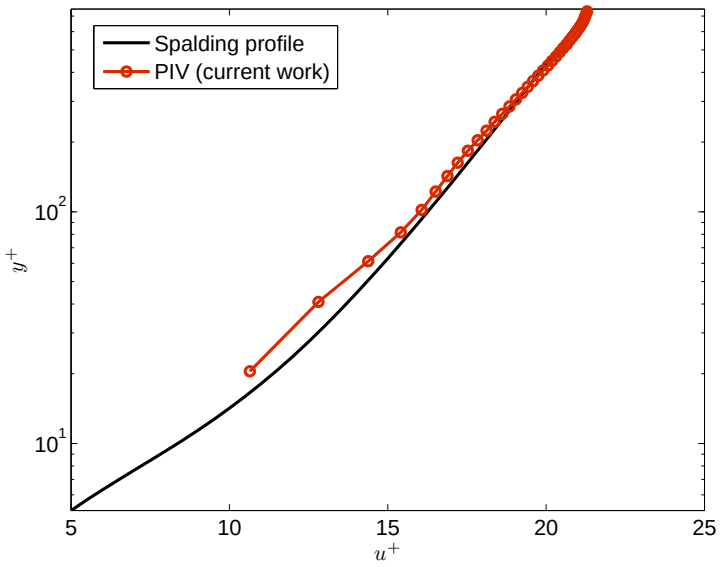

Figure 4.11: Wall profile compared to universal profile from Spalding [1961].

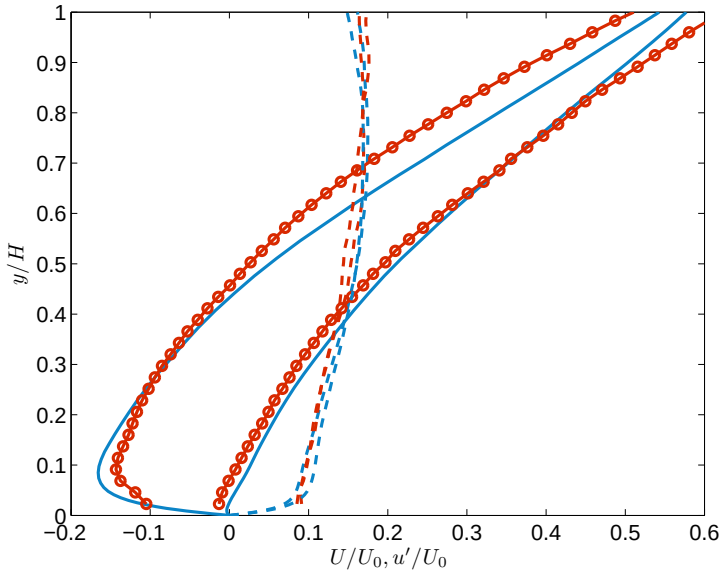

Figure 4.12: Mean (solid line) and RMS (dashed line) streamwise velocity at $x = 2H$ and $x = 4H$ compared to Le et al. [1997].

4.5.2 Fiber-laden flow

Mean streamwise velocity profiles at $x = -10H$ for the carrier flow in the fiber-laden case are shown in Figure 4.13 in comparison to single phase flow. The mean profile appears to be unaffected by fiber presence in the flow, regardless of the concentration. This occurs also downstream of the step, as shown in Figure 4.14 where mean and RMS data are shown at two different downstream positions. These findings are similar to the results shown in Chapter 3 for the fiber-laden jet and have been also reported in literature for spherical particles (Fessler and Eaton [1999]). These results suggest that rod-like particles do not alter the mean flow features of the carrier phase and with this regard behave in a similar way to spherical particles. This is in disagreement with results from Krochak et al. [2009] simulations. They found that in a tapered channel at low Reynolds number the presence of fibers induces relevant changes in the mean flow and in the streamlines. RMS data depicted in Figures 4.13 and 4.14 show that some turbulence modulation, namely enhancement, is noticeable in the region where $y/H > 0.8$. This occurs to a lesser extent in the channel region, and most relevantly in the step region, where the increase at $y/H \approx 1$ and $x = H$ reaches its maximum and is as high as 20% for the $C = C_{v2}$ case. It appears that the amount of turbulence enhancement features some dependence on the concentration of the suspension and it decreases as the distance from the step increases. As shown in Figure 4.14, at $x = 6H$ turbulence modulation effect is very low. Similar results where reported by Fessler and Eaton [1999] where little turbulence modulation was observed after the reattachment point.

4.5.3 Fibers concentration and orientation

In the previous Section, turbulence intensity results showed that the carrier flow in fiber suspensions undergoes a moderate local increase in turbulence, in the region of the flow where $y/H > 0.8$ and for small ($x \approx H$) distances from the step. In this Section we present fibers concentration and orientation data to investigate on this effect.

The orientation angle φ of each fiber with respect to the streamwise axis x is calculated according to Figure 1.2, i.e. φ represents the angle between the horizontal x axis and the projection of the fiber on the $x - y$ plane. This approach is similar to adopting a two-dimensional fiber orientation model. According to the two-dimensional approximation, it is assumed that fibers lye entirely within the $x - y$ plane. Although this is not true, as the phenomena under investigation are three-dimensional, Krochak et al. [2010] showed how this assumption does not undermine the quality of orientation data. In Figure 4.15 a series of probability density functions (PDF) displaying the orientation distribution of fibers at different distances from the wall at $x = -10H$ is shown in the case $C = C_{v2}$. Strong geometrical constraints affect the orientation of fibers in the flow. In general, when the distance of the center of mass of the fiber from the wall is minor than the fiber's half length, namely $y < l/2$, the range of orientation states that the fiber can feature are limited, tending to a limit of $\varphi = 0$ when $y = 0$.

This is confirmed by Figure 4.15, where for $y < l/2$ the PDFs are somewhat narrow and the orientation angle values are clustered around low values (when $y < l/4$ for 90% of fibers $|\varphi| < 10°$). As the distance from the wall increases, the orientation states that can

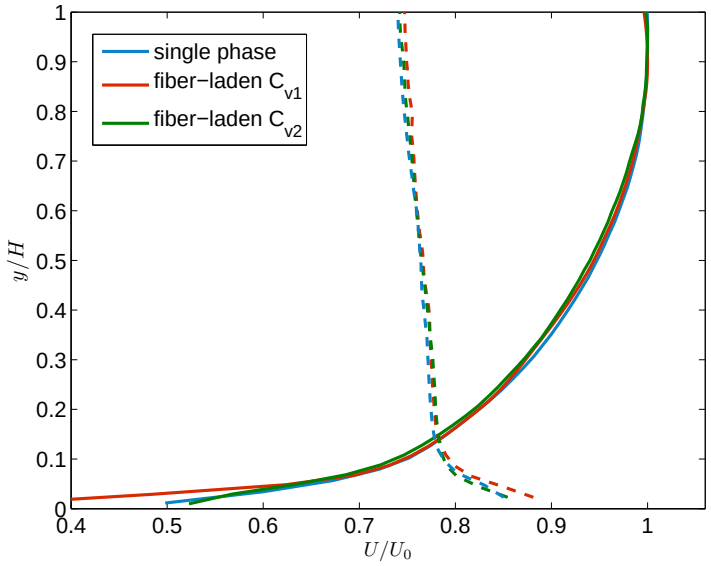

Figure 4.13: Mean and RMS profile of unladen and fiber-laden cases at $x = -10H$.

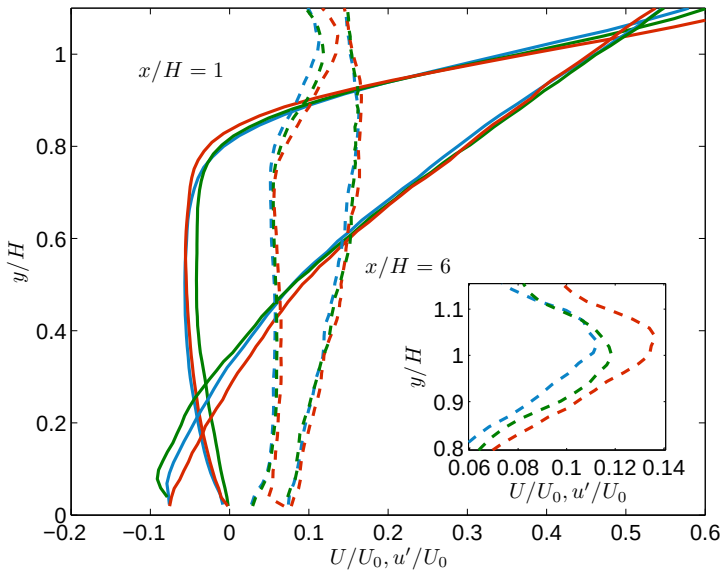

Figure 4.14: Mean (solid lines) and RMS (dashed lines) profile of unladen and fiber-laden cases at $x = 1H$ and $x = 6H$.

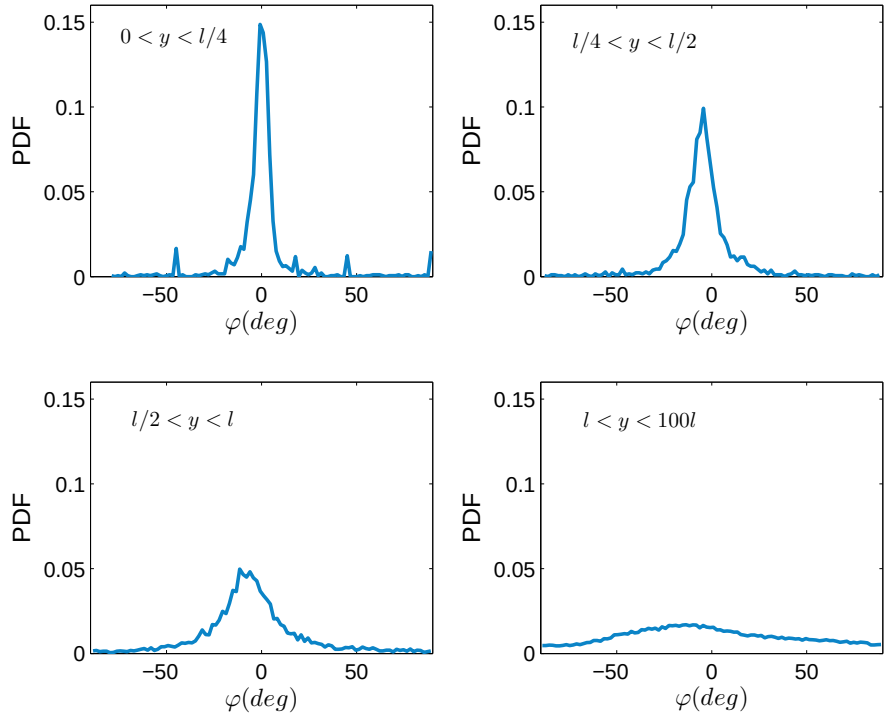

Figure 4.15: Fiber suspension at $x = -10H$ with $C = C_{v2}$: PDF of the orientation angle at different distances form the wall.

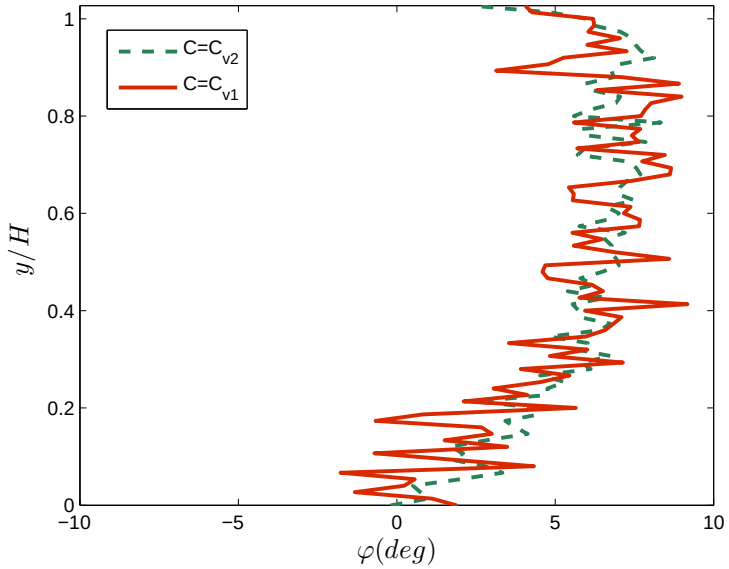

Figure 4.16: Mean orientation angle near the wall at $x = -10H$.

be reached by the fibers grow in number up to $y > l/2$ where no constraints are imposed by the wall and fibers are free to rotate in the flow. This is clearly noticeable in the bottom right picture in Figure 4.15 where, for $l < y < 100l$, the PDF of φ spreads. Another interesting behaviour of fibers may be observed investigating the PDFs at $0 < y < l/4$ and $l/4 < y < l/2$. In the first case, the PDF is centered around $\varphi = 0$: as the distance from the wall increases, already at $l/4 < y < l/2$, the orientation peak shifts towards negative values and this trend is confirmed when $l/2 < y < l$. A negative orientation angle corresponds to fibers pointing away from the wall, i.e. in the direction of shear gradient present near the wall. This behaviour has been reported by other authors (Krochak et al. [2010] among others) and is confirmed by the PDF obtained when y apporoaches the channel centerline. As the distance from the wall increases, the shear gradient gets weaker and the orientation peak is less noticeable (bottom right of Figure 4.15). Similar results have been found for the lower concentration case, in spite of the lower amount of fibers detected. The mean orientation angle at $x = -10H$ is depicted in Figure 4.16 for the fiber suspensions tested. As suggested by the results reported in Figure 4.15, close to the wall fibers tend to align to the shear gradient direction, thus pointing away from the wall. This behaviour has also been observed by Krochak et al. [2010] at low Reynolds number.
Fibers concentration data at $x = -10H$ are shown in Figure 4.17 where fiber normalized number density is reported versus the distance from the wall normalized to the fiber length l.

The normalized number density is calculated dividing the region under analysis into

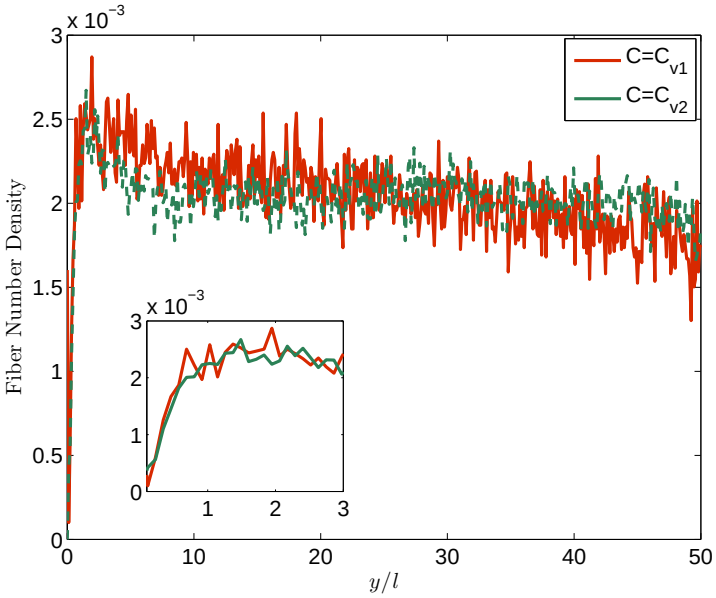

Figure 4.17: Fibers concentration at $x = -10H$.

N bins along the y direction. After counting the number of fibers located in each bin the number is normalized to the overall number of bins. In this case, N was set to 500, achieving good resolution with nearly 500 fibers per each bin. From Figure 4.17 and the relative inset, it appears that for $y < l/2$ the concentration decreases steadily, whereas for $y > l/2$, after a peak in concentration, also reported by other authors (Dearing et al. [2012]), it levels at the uniform concentration value ($1/N = 0.002$). These results may be explained introducing another peculiar phenomenon occurring in fiber suspensions, called "pole-vaulting". Stover et al. [1992] reported that in the near-wall region, fibers tend to move their center of mass away from the wall, in a "vaulting" motion, although it could not be ascertained whether the fibers touched the wall during this movement. This phenomenon may account for the reported concentration trend; fibers close to the wall ($y < l/2$) are sent away from the wall by the pole vaulting mechanism in regions of the flow where $y > l/2$. In the latter region they settle, establishing a fiber concentration gradient.

The region of strong shear present after the step is expected to have relevant effects on fibers concentration and orientation. In Figure 4.18 the mean orientation angle at $x = H$ and $x = 4H$ is shown in the case $C = C_{v2}$, which, thanks to the number of fibers detected, led to reliable results. It may be noticed that in the shear region, fibers tend to orientate with an angle $\varphi \approx 10°$, higher than that observed in the channel, in particular when $x = H$. For $y < 0.5H$ and close to the wall, the effect of the recirculation region behind the step is evident in the shape of the profiles. At $x = 4H$, this effect ends, and

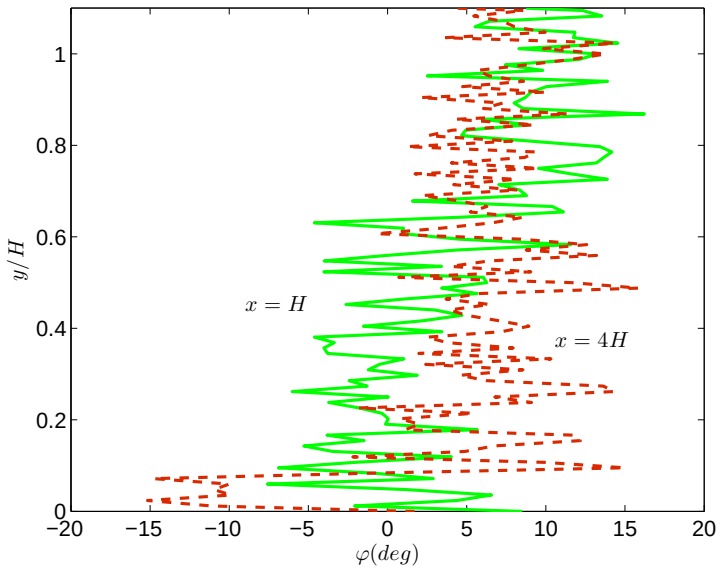

Figure 4.18: Fibers mean orientation angle at $x = H$ and $x = 4H$. $C = C_{v2}$.

the curve becomes flatter.
In order to have a clearer picture of the orientation state of the dispersed phase in the whole field, we show in Figures 4.19 and 4.20 the map of the mean and RMS of the orientation angle. The RMS of φ may be conveniently considered as a measure of the orientation isotropy of the fiber suspension, in that low levels of RMS indicate that fibers within the suspension tend to be packed together. With this in mind, it is possible to compare the results in Figure 4.20 to turbulence modulation results discussed in this Chapter. The region of lowest RMS, i.e. highest isotropy, corresponds to the flow region where turbulence is mostly enhanced.

4.6 Conclusions

In this Chapter, simultaneous PIV calculations of carrier phase and fibers concentration and orientation data have been presented and discussed. Data show that mean profiles are only slightly affected by fibers injection in the flow, whereas turbulence intensity is enhanced locally in the shear layer region downstream of the step and for $x < 6H$. Dispersed phase concentration data showed the peculiar behaviour of fibers close to the wall in the channel section of the flow and their tendency to escape the region close to the wall ($y < l/2$) towards the center of the channel. Orientation data confirm that fibers tend to align to the shear gradient, reversing their average sign at approximately $y \approx 0.2$. Downstream of the step, the presence of a region of strong shear has an impact on fibers

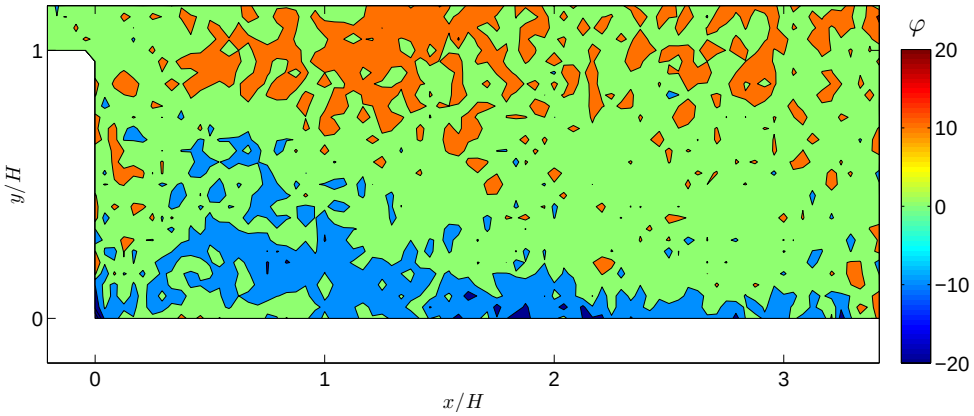

Figure 4.19: Mean orientation angle map. $C = C_{v2}$.

orientation state. Just behind the step, fibers tend to be aligned with the main flow, whereas the recirculation region behind the step has the effect of increasing the absolute value of the orientation angle. Downstream of the step, where $x > 7H$, fibers orientation recovers the profile reported in the channel section of the apparatus. Contour maps of mean and RMS of the orientation angle φ compared to turbulence modulation results, hint at a role played by fibers orientation anisotropy in enhancing turbulence. Where fibers feature higher orientation coherency, i.e. low RMS, turbulence is enhanced.

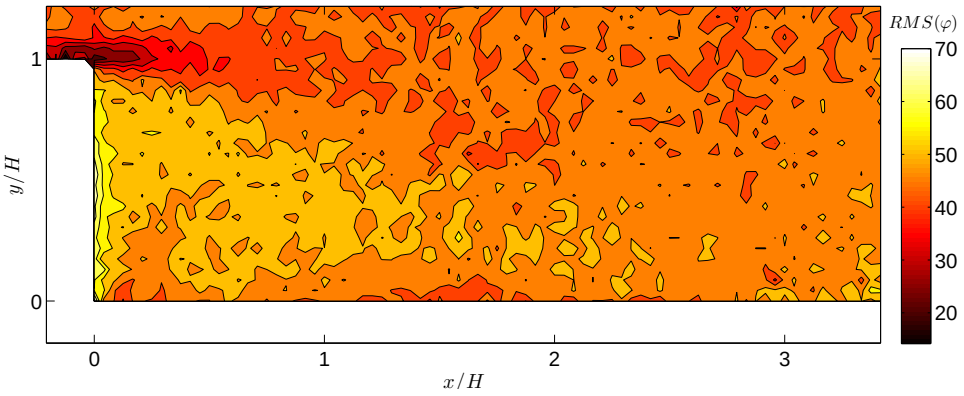

Figure 4.20: RMS of orientation angle map. $C = C_{v2}$.

Conclusions

In this thesis, fiber suspensions have been investigated experimentally by means of High-speed and standard PIV in the framework of two main classes of flow: turbulent pipe jets and channel flows with backward-facing step. A thorough preliminary analysis has been performed on the single phase turbulent jet to shed light on the interaction existing between longitudinal and transversal turbulent structures and their dependence on Reynolds number. To this end, a model has been derived to predict quantities such as entrainment rate comparing the predictions to experimental findings, with good qualitative results. Important relations have been identified between the size of transversal vortical structures and entrainment rate and, statistically, between longitudinal and transversal turbulent intensities.
The next step of this thesis was to analyse the turbulent pipe jet laden with fibers at two different concentrations, leading to very dilute suspensions. A discrimination technique has been presented and validated in order to obtain simultaneous carrier phase velocity data and fiber velocity. The results indicated a relevant turbulence modulation effect even at low concentrations of fibers, which hinted at an important role played by the orientation state of fibers in the turbulent energy transfer processes occuring within the flow-fibers system.
High spatial resolution measurements were performed in a channel flow with BFS apparatus with no dispersed phase, and laden with fibers at two very dilute concentrations. The application of an ad-hoc phase discrimination and fiber identification procedure on the images collected made it possible to acquire fiber orientation data. The results show that the mean velocity fields are not affected by the fiber presence, as in the jet case, and turbulence is enhanced locally. Comparing these results to fiber orientation maps, it appears that turbulence enhancement is linked, rather than to a specific orientation state of fibers, to the level of isotropy of the orientation.

The results of this thesis have been published in the following articles:

A Capone, A Soldati, GP Romano
Mixing and entrainment in the near field of turbulent round jets
Exp Fluids 2013 54:1434

SS Dearing, M Campolo, A Capone, A Soldati
Phase discrimination and object fitting to measure fibers distribution and orientation in turbulent pipe flows
Exp Fluids 2013 54:1419

Bibliography

M Amielh, T Djeridane, F Anselmet L, and Fulachier. Velocity near-field of variable density turbulent jets. *Int J Heat Mass Tran*, 39:2149–2164, 1996.

S Andersson and A Rasmuson. Flow measurements on a turbulent fiber suspension by laser doppler anemometry. *AIChE J*, 46:1106–1119, 2000.

DF Arola and RL Powell. NMR imaging of pulp suspension flowing through an abrupt pipe expansion. *AIChE J*, 44:2597–2606, 1998.

S Balachandar and JK Eaton. Turbulent Dispersed Multiphase Flow. *Annu Rev Fluid Mech*, 42:111–133, 2010.

A Benavides and B van Wachem. Eulerian-Eulerian prediction of dilute turbulent gas-particle flow in a backward-facing step. *Int J Heat Fluid Flow*, 30:452–461, 2009.

O Bernstein and M Shapiro. Direct determination of the orientation distribution function of cylindrical particles immersed in laminar and turbulent shear flows. *Journal of Aerosol Science*, 25:113–136, 1994.

T Boedec and S Simoens. Instantaneous and simultaneous planar velocity fields measurements of two phases for turbulent mixing of high ppressure sprays. *Exp Fluids*, 31: 506–518, 2001.

C Bogey and C Bailly. Turbulence and energy budget in a self-preserving round jet: direct evaluation using large eddy simulation. *J Fluid Mech*, 627:129–160, 2009.

FP Bretherton. The motion of rigid particles in a shear flow at low Reynolds number. *J Fluid Mech*, 14:284–304, 1962.

P Burattini, P Lavoie, and RA Antonia. On the normalized turbulent energy dissipation rate. *Phys Fluids*, 17:098103, 2005.

M Campolo, MV Salvetti, and A Soldati. Mechanisms for microparticle dispersion in a jet in crossflow. *AIChE J*, 51:28–43, 2005.

A Capone, A Soldati, and GP Romano. Mixing and entrainment in the near field of turbulent round jets. *Exp Fluids*, In Press, 2012.

A Carlsson, F Lundell, and LD Soederberg. Fibre orientation control related to papermakings. *J. Fluids Eng.*, 129:457–465, 2007.

A Carlsson, K Hakansson, M Kvick, F Lundell, and LD Soderberg. Evaluation of steerable filter for detection of fibers in flowing suspensions. *Exp Fluids*, 51:987–996, 2011.

JE Cater and J Soria. The evolution of round zero-net-mass-flux jets. *J Fluid Mech*, 472:167–200, 2002.

Y Cheng, S Pothos, and FJ Diez. Phase discrimination method for simultaneous two-phase separation in time-resolved stereo PIV measurements. *Exp Fluids*, 49:1375–1391, 2010.

J Cohen and I Wygnansky. The evolution of instabilities in the axisymmetric jet. Part1. The linear growth of disturbances near the nozzle. *J Fluid Mech*, 176:191–219., 1987.

S Crow and F Champagne. Orderly Structure in Jet Turbulence. *J Fluid Mech*, 48: 547–591, 1971.

CT Crowe. *Multiphase Flow Handbook:Turbulence modulation by particles.* CRC Press, 2006.

CT Crowe, RA Gore, and TR Troutt. Particle dispersion by coherent structures in a free shear flow. *Part Sci Tech J*, 3:149–158, 1985.

S Dearing, M Campolo, A Capone, and A Soldati. Phase discrimination and object fitting to measure fibers distribution and orientation in turbulent pipe flows. *Exp Fluids (In Press)*, 2012.

E Delnoij, J Westerweel, NG Deen, JAM Kuipers, and WPM van Swaaij. Ensemble correlation PIV applied to bubble plumes rising in a bubble column. *Chem Eng Sci*, 54:5159–5171, 1999.

RC Deo, J Mi, and GJ Nathan. The influence of nozzle-exit geometric profile on statistical properties of a turbulent plane jet. *Exp Therm Fluid Sci*, 32:545–559, 2007a.

RC Deo, GJ Nathan, and J Mi. Comparison of turbulent jets issuing from rectangular nozzles with and without sidewalls. *Exp Therm Fluid Sci*, 32:596–606, 2007b.

FJ Diez, MM Torregrosa, and S Pothos. A comparison between round turbulent jets and particle-laden jets in crossflow by using time-resolved stereoscopic particle image velocimetry. *J Fluids Eng-T ASME*, 133:9, 2011.

PE Dimotakis. The mixing transition in turbulent flows. *J Fluid Mech*, 409:69–98, 2000.

KD Driscoll, V Sick, and C Gray. Simultaneous air/fuel-phase PIV measurements in a dense fuel spray. *Exp Fluids*, 35:112–115, 2003.

JK Eaton. Two-way coupled turbulence simulations of gas-particle flows using point particle tracking. *Int J Multiphase Flow*, 35:792–800, 2006.

JK Eaton and JR Fessler. Preferential concentration of particles by turbulence. *Int J Multiphase Flow*, 277:109–134, 1994.

S Elgobashi. On predicting particle-laden turbulent flows. *Appl Sci Res*, 52:30929, 1994.

M Falchi and GP Romano. Evaluation of the performance of high-speed PIV compared to standard PIV in a turbulent jet. *Exp Fluids*, 47:509–526, 2009.

H Fellouah and A Pollard. The near and intermediate field of a Round Free Jet: The effect of Reynolds Number and mixing transition. *Sixth International Symposium on Turbulence and Shear Flow Phenomena (TSFP-6). Seoul, South Korea*, 2009.

JR Fessler and JK Eaton. Turbulence modification by particles in a backward-facing step flow. *J Fluid Mech*, 394:97–117, 1999.

AW Fitzgibbon, M Pilu, and RB Fischer. Direct least squares fitting of ellipse. *IEEE Transactions on pattern analysis and machine intelligence*, 21:476–480, 1999.

D Fleckhaus, K Hishida, and M Maeda. Effect of laden solid particles on the turbulence flow structure of a round free jet. *Exp Fluids*, 5:323–333, 1987.

JJJ Gillissen, J Boersma, PH Mortensen, and HI Andersson. Fibre-induced drag reduction. *J Fluid Mech*, 602:209–218, 2008.

HL Goldsmith and SG Mason. The microrehology of Non-Newtonian suspensions. *Rheol Acta*, 1974.

RA Gore and CT Crowe. Effect of particle size on modulating turbulent intensity. *Int J Multiphase Flow*, 15:279–285, 1989.

E Gutmark and CM Ho. Preferred modes and the spreading rates of jets. *Phys Fluids*, 26:2932–2938, 1983.

ME Hassan and A Meslem. Time-resolved stereoscopic particle image velocimetry investigation of the entrainment in the near field of circular and daisy-shaped orifice jets. *Phys Fluids*, 22:21–32, 2010.

B Hill. Measurement of Local Entrainment Rate in the Initial Region of Axisymmetric Turbulent Air Jets. *J Fluid Mech*, 51:773–779, 1972.

R Holm and D Soederberg. Shear influence on fibre orientation: dilute suspension in the near wall region. *Rheol Acta*, 46:721–729, 2007.

HJ Hussein, SP Capp, and WK George. Velocity measurements in a high-reynolds-number, momentum-conserving, axisymmetric, turbulent jet. *J Fluid Mech*, 258:31–75, 1994.

M Jacob and M Unser. Design of steerable filters for feature detection using canny-like criteria. *IEEE Transactions on pattern analysis and machine intelligence*, 26:1007–1019, 2007.

GB Jeffery. The Motion of Ellipsoidal Particles Immersed in a Viscous Fluid. *Proc R Soc London, Ser A*, 102:161–179, 1922.

R Kerekes and C Schell. Characterization of fibre flocculatioin regimes by a crowding factor. *J Pulp Pap Sci*, 18:32–38., 1992.

DA Khalitov and EK Longmire. Simultaneous two phase PIV by two parameter discrimination. Exp Fluids. *Exp Fluids,*, 32:252–268, 2002.

KT Kiger and C Pan. Two-phase piv for dilute solid/liquid flow. In *Third international workshop on PIV. Santa Barbara*, pages 157–162, 1999.

KT Kiger and C Pan. PIV Technique for the simultaneous Measurement of Dilute Two-Phase Flows. *J Fluid Eng*, 122:811–817, 2000.

J Kim and H Choi. Large eddy simulation of a circular jet: effect of inflow conditions on the near field. *J Fluid Mech*, 620:383–411, 2009.

GP Klaasen and WR Peltier. The role of transverse secondary instabilities in the evolution of free shear layers. *J Fluid Mech*, 202:367–402, 1988.

W Kosiwczuk, A Cessou, M Trinit, and B Lecordier. Simultaneous velocity field measurements in two-phase flows for turbulent mixing of sprays by means of two-phase PIV. *Exp Fluids*, 39:895–908, 2005.

P Krochak, J Olson, and D Martinez. The orientation of semidilute rigid fiber suspensions in a linearly contracting channel flow. *Phys Fluids*, 20:073303, 2008.

PJ Krochak, JA Olson, and DM Martinez. Fiber suspension flow in a tapered channel: the effect of flow/fiber coupling. *Int. J. of Multiphase Flow*, 35:676–688, 2009.

PJ Krochak, JA Olson, and DM Martinez. Near-wall estimates of the concentration and orientation distribution of semi-dilute rigid fibre suspension in poiseuille flow. *J. Fluid Mech.*, 653:431–462, 2010.

J Kuang, CT Hsu, and H Qiu. Experiments on Vertical Turbulent Plane Jets in Water of Finite Depth. *J Eng Mech*, 2001.

J Kussin and M Sommerfeld. Experimental studies on particle behaviour and turbulence modification in horizontal channel flow with different wall roughness. *Exp Fluids*, 33: 143–59, 2002.

M Kvick, K Hakansson, F Lundell, LD Soderberg, and L Prahl Wittberg. Fibre streaks in wall bounded turbulent flow. In *7th International conference on multiphase flows Tampa, Florida*, 2010.

H Le, P Moin, and J Kim. Direct Numerical Simulation of Turbulent Flow Over a Backward-Facing Step. *J Fluid Mech*, 330:349–374, 1997.

F Li, H Qi, and C You. Phase Doppler anemometry measurements and analysis of turbulence modulation in dilute gassolid two-phase shear flows. *J Fluid Mech*, 663: 434–455, 2010.

TQ Li, JD Seymour, RL Powell, KL McCarthy, L Odberg, and MJ McCarthy. Turbulent pipe flow studied by time-averaged NMR imaging: Measurements of velocity profile and turbulent intensity. *Magn Reson Imaging*, 12:923–934, 1994.

D Liepmann and M Gharib. The role of streamwise vorticity in the near-field entrainment of round jets. *J Fluid Mech*, 245:643–648, 1992.

JZ Lin, XY Liang, and SL Zhang. Numerical simulation of fiber orientation distribution in round turbulent jet of fiber suspension. *Chem Eng Res Des*, 6:766–775, 2012.

EK Longmire and JK Eaton. Structure of a particle-laden round jet. *J Fluid Mech*, 36: 217–257, 1992.

F Lundell, LD Sderberg, and PH Alfredsson. Fluid Mechanics of Papermaking. *Annu Rev Fluid Mech*, 43:195–217, 2011.

TG Malmstrom, A Kirkpatrick, B Christensen, and K Knappmiller. Centreline velocity decay measurements in low-velocity axisymmetric jets. *J Fluid Mech*, 246:363–377, 1997.

C Marchioli, MV Salvetti, and A Soldati. Some issues concerning large-eddy simulation of inertial particle dispersion in turbulent bounded flows. *Phys. Fluids*, 20:040603, 2008.

C Marchioli, M Fantoni, and A Soldati. Orientation, distribution and deposition of elongated, inertial fibres in turbulent channel flow. *Phys Fluids*, 22:033301, 2010.

MA Mergheni, JC Sautet, G Godard, HB Ticha, and SB Nasrallah. Experimental investigation of turbulence modulation in particle-laden coaxial jets by Phase Doppler Anemometry. *Exp The Fluid Sci*, 33:517–526, 2009.

B Metzger, JE Butler, and E Guazzelli. Experimental investigation of the instability of a sedimenting suspension of fibres. *J. Fluid Mech.*, 575:307–332, 2007.

J Mi, DS Nobes, and GJ Nathan. Influence of jet exit conditions on the passive scalar field of an axisymmetric free jet. *J Fluid Mech*, 432:91–125, 2001.

J Mi, P Kalt, G Nathan, and C Wong. Piv measurements of a turbulent jet issuing from round sharpedged plate. *Exp Fluids*, 42:625–637, 2007.

P Moin and SV Apte. Large-eddy simulation of realistic gas turbine combustors. *AIAA J*, 44:698–708, 2006.

D Molin, C Marchioli, and A Soldati. Turbulence modulation and microbubble dynamics in vertical channel flow. *Int J Multiphase Flow*, 42:80–95, 2008.

PH Mortensen, HI Andersson, JJJ Gillissen, and BJ Boersma. Dynamics of prolate ellipsoidal particles in a turbulent channel flow. *Phys Fluids*, 20:093302, 2008a.

PH Mortensen, HI Andersson, JJJ Gillissen, and BJ Boersma. On the orientation of ellipsoidal particles in a turbulent shear flow. *Int J Multiphase Flow*, 7:678–683, 2008b.

KB Moses, SG Advani, and A Reinhardt. Investigation of fibre motion near solid boundaries in simple shear flow. *Rheol Acta*, 40:296–396, 2001.

P O'Neill, J Soria, and D Honnery. The stability of low Reynolds number round jets. *Exp Fluids*, 36:473–483, 2004.

AD Paris. Turbulence attenuation in a particle-laden channel flow. *Thesis (PhD)*, 2002.

S Parsa, J Guasto, K Kishore, N Ouellette, J Gollub, and G Voth. Rotation and alignment of rods in twodimensional chaotic flow. *Phys Fluids*, 23:043302, 2011.

M Parsheh, ML Brown, and CK Aidun. On the orientation of stiff fibres suspended in turbulent flow in a planar contraction. *J Fluid Mech*, 545:245–269, 2005a.

M Parsheh, ML Brown, and CK Aidun. Variation of fiber orientation in turbulent flow inside a planar contraction with different shapes. *Int J Multiphase Flow*, 32:1354–1369, 2005b.

RN Parthasarathy and YH Chan. Turbulence modification in dilute small-particle-laden liquid jets. *AIAA J*, 39:535–537, 2001.

RN Parthasarathy and GM Faeth. Turbulence modulation in homogeneous dilute particle-laden flows. *J Fluid Mech*, 220:485–514, 1990.

S Paschkewitz, C Dmitropoulos, Y Hou, V Somandepalli, M Mungalm, E Shaqfeh, and P Moin. An experimental and numerical investigation of drag reduction in a turbulent boundary layer using a rigid rodlike polymer. *Phys Fluids*, 17:085101, 2005.

M Piirto, P Saarenrinne, H Eloranta, and R Karvinen. Measuring turbulence energy with PIV in a backward-facing step flow. *Exp Fluids*, 35:219–236, 2003.

C Poelma, J Westerweel, and G Ooms. Turbulence statistics from optical whole-field measurements in particle-laden turbulence. *Exp Fluids*, 40:347–363, 2006.

C Poelma, J Westerweel, and G Ooms. Particle-fluid interactions in grid-generated turbulence. *J Fluid Mech*, 589:315–351, 2007.

SB Pope. *Turbulent Flows*. Cambridge University Press, 2000.

F Prevost, J Boree, HJ Nuglisch, and G Charnay. Measurement of Fluid/Particle correlated motion in the far-field of an axisymmetric jet. *Int J Multiphase Flow*, 22: 685–701, 1996.

WR Quinn. Upstream shaping effects on near field flow in round turbulent free jets. *Eur J Mech B-Fluid*, 25:279–301, 2006.

WR Quinn. Experimental study of the near field and transition region of a free jet issuing from a sharp-edged elliptic orifice plate. *Eur J Mech B-Fluid*, 26:583–614, 2007.

M Raffel, C Willert, and J Kompenhans. *Particle Imaging Velocimetry: a practical guide. 2nd edition*. Springer, 2002.

GP Romano. The effect of boundary conditions by the side of the nozzle of a low Reynolds number jet. *Exp Fluids*, 33:323–333, 2002.

KA Rose, JA Meier, GM Dougherty, and JG Santiago. Rotational electrophoresis of striped metallic microrods. *Phys Rev E*, 75:011503, 2007.

KA Rose, B Hoffman, D Saintillan, ESG Shaqfeh, and JG Santiago. Hydrodynamic interactions in metal rodlike-particle suspensions due to induced charge electroosmosis. *Phys Rev E*, 79:011402, 2009.

DWI Rouson and JK Eaton. On the preferential concentration of solid particles in turbulent channel flow. *J Fluid Mech*, 428:149–169, 2001.

R Sadr and JC Klewicki. Flow field characteristics in the near field region of particle-laden coaxial jets. *Exp Fluids*, 39:885–894, 2005.

Y Sato, M Mori, Y Takeda, K Hishida, and M Maeda. Signal processing for advanced correlation ultrasonic velocity profiler. *Third International Symposium on Ultrasonic Doppler Methods for Fluid Mechanics and Fluid Engineering. EPFL, Lausanne, Switzerland.*, 2002.

F Sbrizzai, R Verzicco, MF Pidria, and A Soldati. Mechanisms for selective radial dispersion of microparticles in the transitional region of a confined turbulent round jet. *Int J of Multiphase Flow*, 30:1389–1417, 2004.

F Sbrizzai, R Verzicco, and A Soldati. Turbulent Flow and Dispersion of Inertial Particles in a Confined Jet Issued by a Long Cylindrical Pipe. *Flow Turbul Combust*, 82: 1–23, 2009.

M Shapiro and M Goldenberg. Deposition of glass fiber particles from turbulent air flow in a pipe. *J Aerosol Sci*, 24:65, 1993.

DB Spalding. A single formula for the Law of the Wall. *Mech Trans ASME Ser E*, 83: 455–457, 1961.

KD Squires and JK Eaton. Preferential concentration of particles by turbulence. *Phys Fluids*, 3:1169–1178, 1991.

M Stanislas, K Okamoto, CJ Kahler, J Westerweel, and F Scarano. Main results of the third International PIV Challenge. *Exp Fluids*, 45:27–71, 2008.

M Steen. On turbulence structure in vertical pipe flow of fiber suspensions. *Nord Pulp Pap Res*, 1989.

CA Stover, DL Koch, and C Cohen. Observation of fibre orientation in simple shear flow of semi-dilute suspensions. *J Fluid Mech*, 238:277–296, 1992.

B Toth, J Anthoine, and ML Riethmuller. Two-phase PIV method using two excitation and two emission spectra. *Exp Fluids*, 47:475–487, 2009.

DP Towers, CE Towers, CH Buckberry, and M Reeves. A colour PIV system employing fluorescent particles for two-phase flow measurements. *Meas Sci Technol*, 10:824–830, 1999.

BJ Trevelyan and SG Mason. Particle motions in sheared suspensions. I. Rotations. *J Coll Sci*, 6:354–367, 1951.

LP Wang and M Maxey. Settling Velocity and Concentration Distribution of Heavy Particles in Homogeneous Isotropic Turbulence. *J Fluid Mech*, 256:27–68, 1993.

JA Wiklund, M Stading, AJ Pettersson, and A Rasmuson. A comparative study of UVP and LDA techniques for pulp suspensions in pipe flow. *AIChE J*, 2006.

I Wygnanski and HE Fiedler. Some measurements in the self-preserving jet. *J Fluid Mech*, 38:577–612, 1969.

G Xu and RU Antonia. Effect of different initial conditions on a turbulent round free jet. *Exp Fluids*, 33:677–683, 2002.

TS Yang and SS Shy. Two-way interaction between solid particles and homogeneous air turbulence: particle settling rate and turbulence modification measurements. *J Fluid Mech*, 526:171–216, 2005.

KF Yu and EWM Lee. Evaluation and modification of gas-particle covariance models by Large Eddy Simulation of a particle-laden turbulent flows over a backward-facing step. *Int J Multiphase Flow*, 52:5652–5656, 2009.

KBMQ Zaman and AKMF Hussain. Turbulence suppression in free shear flows by controlled excitation. *J Fluid Mech*, 103:133–159, 1981.

H Zhang, G Ahmadi, FG Fan, and JB McLaughlin. Ellipsoidal particles transport and deposition in turbulent channel flows. *Int J Multiphase Flow*, 27:971–1009, 2001.

CK Zoltani and AF Bicen. Velocity measurements in a turbulent, dilute, two-phase jet. *Exp Fluids*, 9:295–300, 1990.